PE&RS

July 2023 Volume 89, Number 7

Photogrammetric Engineering & Remote Sensing *The official journal for imaging and geospatial information science and technology*

JOIN ASPRS TODAY!

asprs THE IMAGING & GEOSPATIAL INFORMATION SOCIETY

ACCELERATE YOUR CAREER!

PHOTOGRAMMETRY · REMOTE SENSING · GIS · LIDAR · UAS …and more!

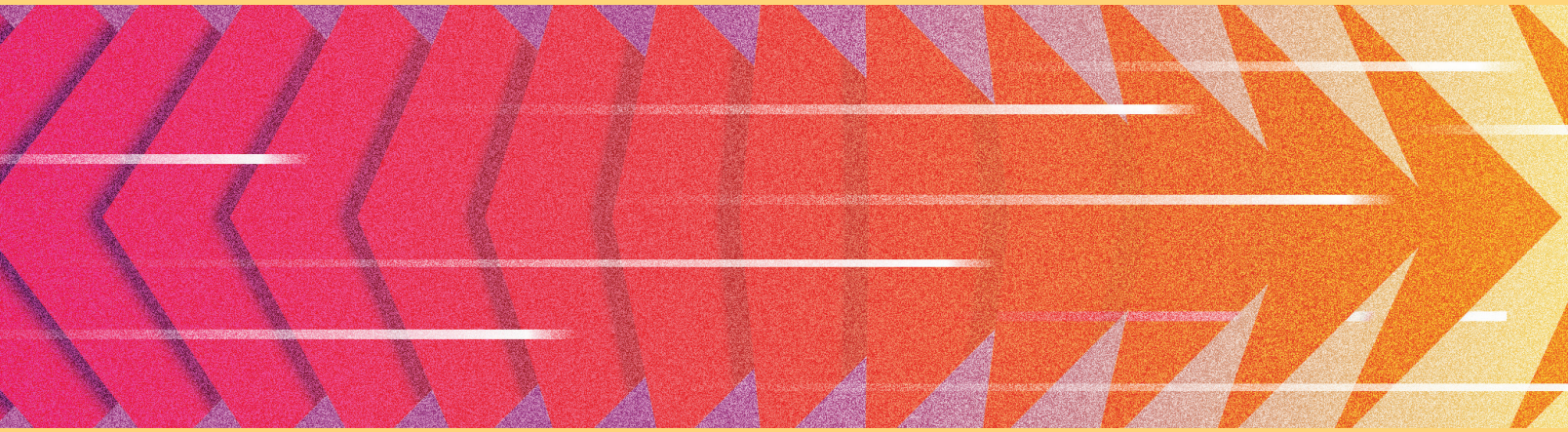

LEARN

- Read our journal, *PE&RS*
- Attend professional development workshops, GeoBytes, and online courses through the ASPRS ProLearn platform
- Earn professional development hours (PDH)
- Attend our national & regional meetings and conferences

DO

- Write for *PE&RS*
- Innovate to create new geospatial technologies
- Present at our national & regional meetings and conferences
- Engage & network

GIVE

- Participate in the development of standards & best practices
- Influence state licensure through our NCEES affiliation
- Mentor colleagues & support students
- Educate others about geospatial science & technology

BELONG

- Establish yourself as a geospatial expert
- Grow business relationships
- Brand yourself and your company as geospatial leaders
- Connect to the world via our affiliation with ISPRS

Don’t delay, join today at **asprs.org**

ANNOUNCEMENTS

The National Oceanic and Atmospheric Administration has signed **Woolpert** to a $7 million contract to perform hydrographic surveying and collect bathymetric data in and around Nome, Alaska. These data will support commercial fishing, shipping channels, coastal resilience, scientific research, and Seabed 2030, a collaborative project that aims to map the world's ocean floor by 2030.

Woolpert will collect data over 1,874 square nautical miles in Northern Norton Sound, which stretches from Golovin Bay through Nome to Cape Woolley on the eastern edge of Alaska. Nome is adjacent to the Bering Strait and central to America's marine presence in the Arctic. The region serves as a major transit route for shipping traffic to the Port of Nome, which has supplied food, construction materials, equipment, and other goods for over 60 Alaskan communities for more than a century.

Regional hydrographic data was most recently collected in the 1930s. This project will update National Ocean Service nautical charting products and services and will support the Seabed 2030 Project. This collaborative effort between the Nippon Foundation and the General Bathymetric Chart of the Oceans aims to integrate and share all available bathymetric data to produce a definitive map of the world's ocean floor by 2030.

Woolpert has collected topographic, bathymetric, and hydrographic data in and around Alaska for decades and has an office in Wasilla. Multiple hydrographic survey vessels will be used to collect these data, including two large live-aboard ships and two Wave Adaptive Modular Vessels (WAM-Vs). The WAM-Vs will be used primarily in a force multiplication strategy in coordination with the larger vessels performing this work. A combination of the right tools and experience are critical for this contract.

"Hydrographic surveying in Alaska can be logistically challenging, and moving equipment requires a range of vehicles and aircraft," Woolpert Certified Hydrographer Dave Neff said. "Local knowledge and relationships are highly beneficial for any project in Alaska. Our work over the years both as Woolpert and eTrac, a Woolpert Company, has given us the scope and confidence to cost-effectively execute, while managing inherent regional risk. We're at home in Alaska, and we are excited to provide these needed data for Nome and all who rely on the region for goods and services."

This project will get underway in June and is expected to conclude in September.

NV5 Geospatial announced it has completed lidar data collection across 5,125 square miles of Eastern Massachusetts. The detailed data – collected as part of the U.S. Geological Survey (USGS) 3D Elevation Program (3DEP) and now publicly available from Massachusetts Bureau of Geographic Information (MassGIS) – uncovered 1,000 primary addresses and over 10,000 structures previously unidentified by imagery alone, offering insights the Commonwealth can use to support emergency services, property tax assessment and boundary infringement inquiries, and saving time and money required for additional boots-on-the-ground examinations.

The collection also provides useful elevation data to support infrastructure, transportation and utility projects; improve the accuracy and precision of hydrologic network mapping; and classify and manage structures and vegetation.

"This new lidar survey replaces data from about 10 existing ad hoc elevation mapping projects completed over the last 25 years by various public agencies, each with differences in coverage, accuracy and point density," said Peter Grace, GIS Analyst and 911 Team Lead for the Massachusetts Executive Office of Technology Services and Security (EOTSS).

In Spring 2021, the USGS, on behalf of MassGIS, contracted with NV5 Geospatial to acquire the eastern portion of Massachusetts at a QL 1 lidar specification, which is four times more detailed than previous specifications. As part of 3DEP, federal grant funds for the project were provided to a partnership coordinated by MassGIS, between the Massachusetts Department of Transportation, the Executive Office of Energy and Environmental Affairs (EEA), the Executive Office of Technology Services and Security (EOTSS), and the Cape Cod Commission.

"Our collaboration with the USGS and NV5 enabled us to deliver valuable data that can be applied in numerous ways," said Neil MacGaffey, retired director of MassGIS, who initially led the project. "This freely available data can help municipalities and state agencies improve infrastructure designs and gain a better understanding of structures in their jurisdiction, make communities more resilient, model stormwater volume and areas at risk from flooding more accurately, and ultimately minimize the spend for all interested parties valuable through economies of scale in data acquisition."

For more information about the MassGIS project and NV5 3DEP work, contact Drew Meren, Drew.Meren@nv5.com.

ACCOMPLISHMENTS

This March at its inaugural Tech Summit, Liberty Latin America recognized Esri with an Innovative Small Suppliers Award at the summit's 2023 Vendor Awards. The telecommunications company serving Latin America and the Caribbean honored Esri, the global leader in geographic information system (GIS) technology at the event which showcased the contributions made by key vendor partners.

The Summit focused on the critical importance of innovation in driving business opportunities and economic development across the region, as well as how Liberty Latin America is improving customer experience through automated tools, developing new products, growing fixed-mobile convergence, and providing next generation B2B solutions.

Esri's GIS software is used by Liberty Latin America to improve the operations of its various regional departments which are spread out across the region as well as in the Caribbean. The company was able to expand service at scale, while increasing collaboration. Deploying the Esri apps, ArcGIS Survey123 and ArcGIS Collector, they were able to solve complex business challenges related to mobile data gathering in new and innovative ways. All these new implementations saved Liberty Latin America time and money for customers, while also establishing them as a leader in the industry, providing service where it is needed most.

"This first Tech Summit aligns perfectly with our company's purpose of connecting communities and changing lives," said Aamir Hussain, Liberty Latin America's Chief Technology and Product Officer. "Our focus on driving growth through innovation is essential to stay ahead in today's fast-paced world. We are thrilled to showcase our cutting-edge products and solutions and learn from industry-leading speakers. With the collective wisdom and insights gained from this event, we look forward to driving innovation that will create a positive impact across our region."

Liberty Latin America showcased its products and services at the summit, including Hybrid Cloud, Private Networks, Always On connectivity, Next-Gen Unified Communications, Video Analytics, its portfolio of 5G Handsets, and how e-SIM will be deployed across the region. In addition, the company shared how it is preparing its fixed networks to deliver higher speeds, enhancing mobile performance through a new wireless core, and enabling IT transformation.

Esri was one of five suppliers to be recognized for their contributions to Liberty Latin America's telecom service innovations.

ASPRS & GEO WEEK — STRONGER TOGETHER IN 2024

ONE CONFERENCE PASS. A WORLD OF GEOSPATIAL EDUCATION.

FEBRUARY 11-13, 2024 | DENVER, COLORADO

Exciting News! For the first time in 2024, Geo Week will offer attendees a single comprehensive conference pass that provides access to Geo Week conference sessions and ASPRS conference sessions.

By uniting these two premier conferences, Geo Week offers an unprecedented opportunity for professionals engaged in photogrammetry, remote sensing, GIS, and related technologies to extract maximum value from attending. You'll gain insights through technical deep-dives, stay informed with the latest project updates, delve into real-world case studies, explore cutting-edge hardware and software applications, acquire essential workflow best practices, and more.

The conference pass includes entry to the Exhibit Floor, select networking events, the Geo Week Awards Ceremony, and the new Student Hub featuring student presentations and posters. In addition to the main conference programming, ASPRS will host pre-show workshops for an additional fee.

As always, ASPRS members will receive a member discount that will be available on the ASPRS website when registration opens in October. The Conference Program will be posted in late October. Find all event updates at www.geo-week.com.

SAVE THE DATE!

PE&RS
PHOTOGRAMMETRIC ENGINEERING & REMOTE SENSING
The official journal for imaging and geospatial information science and technology
July 2023 Volume 89 Number 7

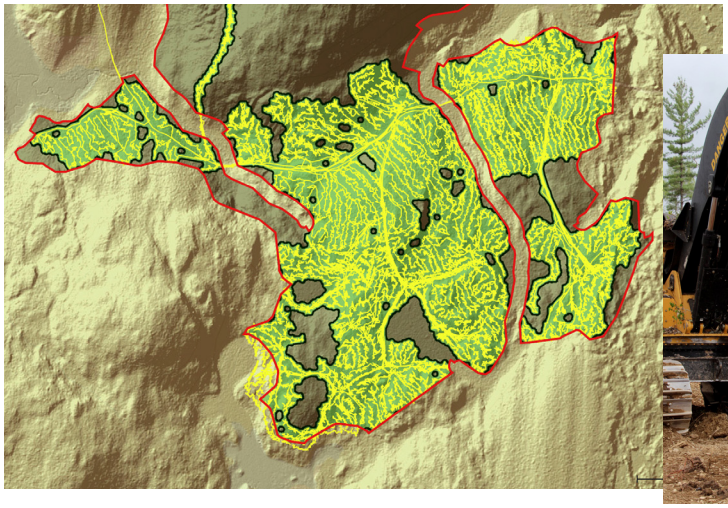

COLUMNS

ANNOUNCEMENTS

Call for *PE&RS* Special Issue Submissions

DEPARTMENTS

See the Cover Description on Page 400

COVER DESCRIPTION

Perched on the Qinghai-Tibetan Plateau in western China, Qinghai Lake is a biodiverse outpost within the arid steppe—and a sensitive indicator of the region's climatic shifts. The lake's fluctuating water level serves as a de facto gauge of climate change in this high-altitude watershed.

Recent changes in the lake level are apparent in this pair of satellite images, captured by the Thematic Mapper (TM) on Landsat 5 on July 29, 2010 (above), and by the Operational Land Imager-2 (OLI-2) on Landsat 9 on July 22, 2022 (cover). Sand spits stretching nearly 25 kilometers (15 miles) once cleared the water's surface and cordoned off lakes within the lake. However, they were mostly submerged by 2022.

Researchers measuring water levels in Qinghai Lake reported that the level declined steadily at an average rate of 8 centimeters (3 inches) per year from 1961 to 2004. At that point, the trend reversed, and the lake started rising at 18 centimeters (7 inches) per year through the end of the study period in 2019.

The striking turnaround coincided with trends of warming and wetting, according to the authors. Lake levels declined prior to 2004 primarily due to decreased river runoff. The subsequent rise in lake levels was driven by increasing precipitation and river runoff, as well as decreasing evaporation. (There is no outflow from the lake.) Though less evaporation doesn't intuitively track with warming temperatures, the researchers note that temperature increases were more significant in winter months, when the lake was covered with ice, than in summer months. Summers saw more precipitation, which meant more cloudy days, higher humidity, and therefore less evaporation.

The evolution of the sand spit is one of the more dynamic effects of the lake's fluctuations. When water levels were lower, more lakebed sediments were exposed to the prevailing westerly winds, which swept the sediments to the eastern shore of the lake. As dunes built up there, they divided Qinghai Lake into several sub-lakes, including Shadao Lake (centered in the top-left image) and Haiyan Bay (toward the bottom-right of the wider view). These lakes appear isolated from Qinghai Lake in the 2010 image but were mostly reincorporated in 2022.

The importance of Qinghai Lake and its wetlands goes beyond its climate signals. Many species are endemic to the plateau, and the endangered Przewalski's gazelle lives only around Qinghai Lake. The ecosystem also plays a critical role as a breeding and stopover site for many migratory waterbirds along the Central Asian and East Asian Flyways.

The full version of both images can be downloaded from https://landsat.visibleearth.nasa.gov/view.php?id=151316.

NASA Earth Observatory images by Allison Nussbaum, using Landsat data from the U.S. Geological Survey. Story by Lindsey Doermann.

PHOTOGRAMMETRIC ENGINEERING & REMOTE SENSING

JOURNAL STAFF

Publisher ASPRS
Editor-In-Chief Alper Yilmaz
Director of Publications Rae Kelley
Electronic Publications Manager/Graphic Artist
Matthew Austin

Photogrammetric Engineering & Remote Sensing is the official journal of the American Society for Photogrammetry and Remote Sensing. It is devoted to the exchange of ideas and information about the applications of photogrammetry, remote sensing, and geographic information systems. The technical activities of the Society are conducted through the following Technical Divisions: Geographic Information Systems, Photogrammetric Applications, Lidar, Primary Data Acquisition, Professional Practice, Remote Sensing Applications, and Unmanned Autonomous Systems. Additional information on the functioning of the Technical Divisions and the Society can be found in the Yearbook issue of *PE&RS*.

All written correspondence should be directed to the American Society for Photogrammetry and Remote Sensing, PO Box 14713, Baton Rouge, LA 70898, including general inquiries, memberships, subscriptions, business and editorial matters, changes in address, manuscripts for publication, advertising, back issues, and publications. The telephone number of the Society Headquarters is 301-493-0290; the fax number is 225-408-4422; web address is www.asprs.org.

PE&RS. *PE&RS* (ISSN0099-1112) is published monthly by the American Society for Photogrammetry and Remote Sensing, 8550 United Plaza Blvd, Suite 1001, Baton Rouge, Louisiana 70809 . Periodicals postage paid at Bethesda, Maryland and at additional mailing offices.

SUBSCRIPTION. *PE&RS* is available as an e-Subscription (single-site and multi-site licenses) and an e-Subscription with print add-on (single-site license only). PE&RS subscriptions are on a calendar-year, beginning in January and ending in December.

The rate for a single-site e-Subscription for the USA/Non-USA is $1040 USD, for Canadian* is $1092 USD.

The rate for a multi-site e-Subscription for the USA/Non-USA is $1040 USD plus $250 USD for each additional license, for Canadian* is $1092 USD plus $263 for each additional license.

The rate for e-Subscription with print add-on for the USA is $1525 USD, for Canadian* is $1612 USD, and for Non-USA is $1565 USD.

*Note: Subscription prices for Canada includes 5% of the total amount for Canada's Goods and Services Tax (GST #135123065). **PLEASE NOTE: All Subscription Agencies receive a 20.00 USD discount.**

POSTMASTER. Send address changes to PE&RS, ASPRS, PO Box 14713, Baton Rouge, LA 70898. CDN CPM #(40020812).

MEMBERSHIP. Membership is open to any person actively engaged in the practice of photogrammetry, photointerpretation, remote sensing and geographic information systems; or who by means of education or profession is interested in the application or development of these arts and sciences. Membership is for one year, with renewal based on the anniversary date of the month joined. Membership Dues include a 12-month electronic subscription to *PE&RS*. Annual Individual Membership dues are $175.00 USD and Student Membership dues are $50.00 USD. A tax of 5% for Canada's Goods and Service Tax (GST #135123065) is applied to all members residing in Canada.

Kevin Lim, *Ph.D.*

The Journey from a Ph.D. to a Successful Company

At the start of my doctoral studies, I wasn't sure whether I would remain in academia or transition to a career in the forestry industry. I had a foot in each door, with an applied research project on the use of airborne lidar to map forests funded by both academic and industry sources. Ultimately, my entrepreneurial side prevailed. I spent the final two years of my PhD working in industry and, upon graduation in 2006, decided to take my work to market. A common view among my peers was that there was a great deal of innovation "locked in academia": student research that unfortunately never left campus, despite its potential industry benefits. I had always been curious to find out why this might be so, and I reasoned that by using my own work as a test case, I would get a crash course in facing the challenges of transforming promising research into a profitable business. While I can now safely call it a success story–Lim Geomatics has pioneered numerous forestry technology solutions and is one of Canada's fastest growing companies—the climb has, at times, been steep.

In the start-up phase, I discovered an ironic disconnect between business training and real life. The former centres on creating ideal situations and analyzing them to the last detail: skills ill-suited to navigating the quick, unpredictable flow of life as an entrepreneur. Spending a month painstakingly creating a business plan doesn't keep things from veering off in an unpredictable direction the minute you make your first sale. As a self-taught CEO, I believe entrepreneurship is more a matter of character than education. Mental agility is key to maintaining momentum in the face of uncertainties, and keeping a level head allows you to gain wisdom from failure rather than dwelling on it. You have to blow yourself up, you have to trip a million times; otherwise, you're not going to learn.

Looking back, like many other new grads, I entered the business world wearing rose-coloured glasses, hopeful that prospective clients would be as enthusiastic about my work as I was and would see its value as clearly as I did. Often, fresh science graduates are so focused on their product or solution, the technical magic they've brought to life, that they lose sight of what it really takes to go to market. Unfortunately, hope is not a viable business strategy. Value is determined by the customer, not by how technologically impressive the product is or how strongly its creator believes in it–and being a business means actually selling something. As an example, I once attended a conference and met a scientist who had developed some new technology. Although I wasn't interested in acquiring the entire product, I saw that one small element of it would be beneficial in a range of contexts at my company. I was eager to discuss buying just that piece, but the scientist was unwilling to consider it, instead attempting unsuccessfully to convince me that the true value was in the product as a whole. That all-or-nothing approach, the insistence on keeping one's work intact and "perfect," may serve a researcher well in academia, but it proves self-defeating in business. A piece of the work, if it comes at the right time and solves the right problems, may be of greater value than the whole from the customer's standpoint.

Working in forestry also brings some industry-specific challenges. At Lim Geomatics, we're still trying to commercialize, to some extent, what we've had for 16 years. Even after demonstrating to a prospective client exactly how adopting our technology would streamline their processes or reduce their costs, there's no guarantee of buy-in. No matter how many success stories we have from forestry companies that have chosen to work with us, others still aren't ready to go out on a "lim(b.)" I'm confident that the quality of the technology isn't the problem, and I don't think money is the deciding factor either: many

Photogrammetric Engineering & Remote Sensing
Vol. 89, No. 7, July 2023, pp. 401-403.
0099-1112/22/401-403

doi: 10.14358/PERS.89.7.401

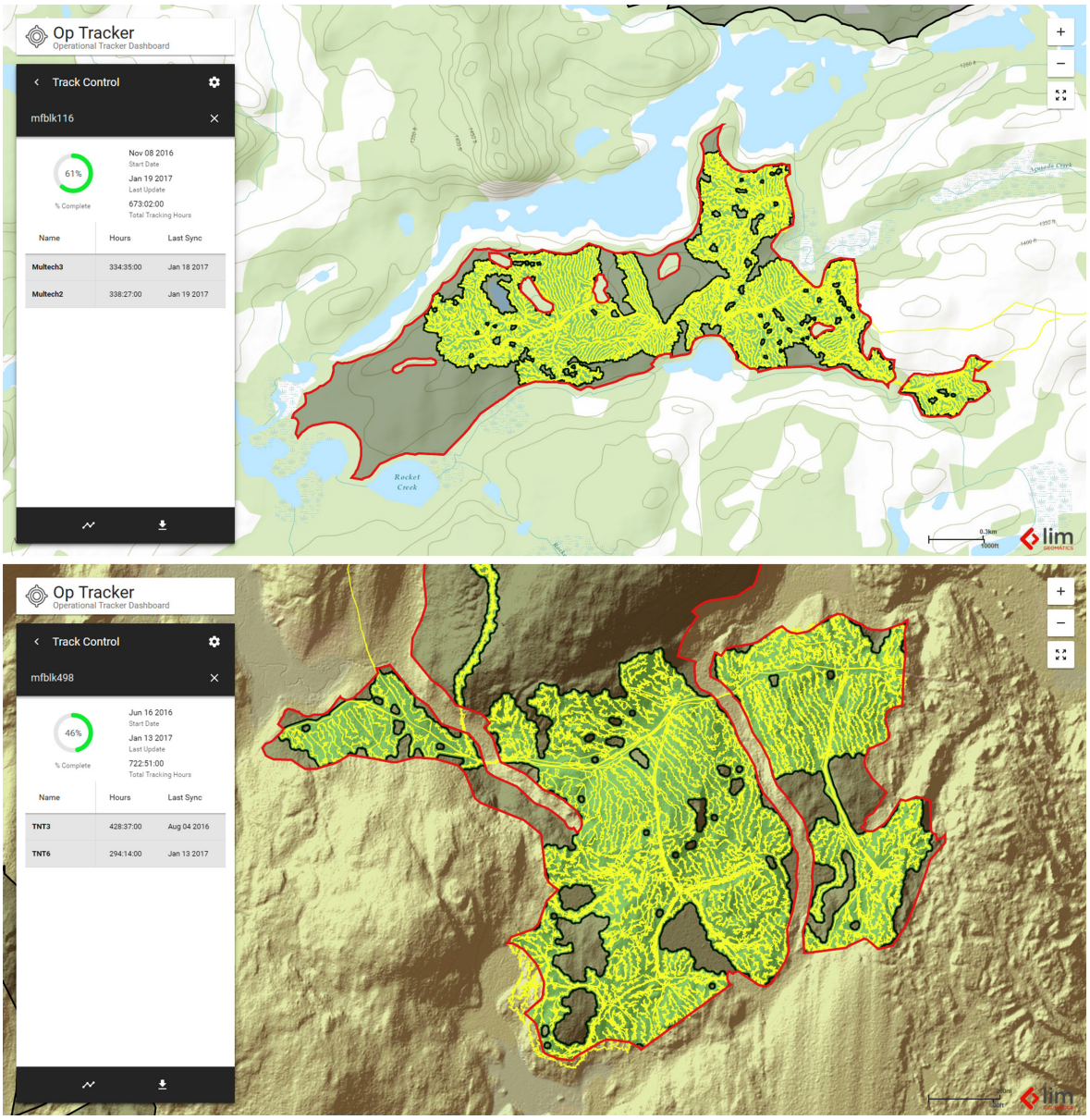

These are screenshots of feller buncher machine tracks (yellow) and the areas harvested (green buffer). The harvested areas are referred to as depletion areas or as-builts. Our mobile technology is installed in the cabs of forestry machines so we can track and report on productivity, specifically productive machine hours (PMH). The lower image shows a hillshade derived from airborne lidar. Both images are delivered through the Op Tracker web application. In this example, lidar remote sensing data, telematics, and GIS are merged together to provide insights into timber harvesting operations.

of the companies that are hesitant to permanently adopt new technology are happy to fund any number of pilots. The main obstacle, as I see it, is resistance to change. For the client, adoption of new technology requires a solid change-management strategy. Although the transition will ultimately result in smoother workflow and decreased costs, it does come with a degree of uncertainty in its early stages, and adaptation to new tools and procedures may temporarily increase the workload of employees who are already stretched thin. Another major factor of change-resistance is that the forestry industry often takes a "traditional" approach to business relationships, preferring to work with familiar companies and revisit past connections over trying something—or someone—new.

How, then, does a new player compete? For one thing, I recommend that novice entrepreneurs consider partnering with more established companies, a strategy I myself unwisely resisted in my company's early days. One person competing against a small business, let alone a large and well-established company, is a David vs. Goliath situation that rarely has the same positive outcome as the story. While collaboration must be undertaken carefully due to the risk of intellectual property being appropriated, it also comes with advantages, such as network connections and greater industry visibility. A second and more important strategy is establishing trust. "People aren't buying you, they're buying the brand" is a saying I have come to understand in the process of building my company—and for me, trust is the foundation of every partnership. Companies that sign with Lim Geomatics trust us to deliver, to do the right thing, based on our brand.

When it comes to building a business, I don't think there is a "right path." Mine has entailed tremendous personal and professional growth, from bootstrapping as a new entrepreneur to

These are screenshots from AFRIDS (Advanced Forest Inventory Decision Support), a solution that allows foresters to interact with forest inventory information products derived from airborne lidar. The upper image shows RGB imagery blended with a canopy height model derived from lidar. A user can draw a block and, within seconds, receive analytics on it: for example, area, volume, height and basal area data. The graph in the lower image is an expanded view of the top pop-up. It presents forest inventory data derived from airborne lidar in addition to diameter distribution data by volume and density.

scaling the operations of a nearly 20-year-old company. Along the way, mentors have been instrumental, providing both opportunities and inspiration. I would highlight the influence of my father, who also built a successful career in computer science; my doctoral supervisor Dr. Paul Treitz, who was always great in enabling my curiosity; Dr. Bob Ryerson, who (after a briefly tense exchange over pizza about similar-sounding company names) entrusted me with door-opening technical work in the Maldives; and now the other CEOs who comprise TEC Canada, notably Pascal St-Jean. I am optimistic that the forestry technology industry is on an upswing. One can cite a current wave of long-standing, more traditional companies that have built up more technical capacity or bought some intellectual property. Innovation remains a key interest of mine: I'm always on the lookout for ideas with commercial potential, and in the future I hope to start a "uni bootcamp" for scientists seeking to market their work. Commercializing academic research is hard—but it shouldn't be!

References

Lim, K. 2006. LiDAR Remote Sensing of Forest Canopy and Stand Structure Ph.D. dissertation Queen's University, Kingston, Ontario, Canada.

Lim K., Treitz P., Baldwin K., Morrison I., Green J. 2003. Lidar remote sensing of biophysical properties of tolerant northern hardwood forests, *Canadian Journal of Remote Sensing*, 29:5, 658-678, DOI: 10.5589/m03-025.

Author

Kevin Lim, Ph.D., President & CEO
Lim Geomatics Inc.
2685 Queensview Drive, Suite 102
Ottawa, Ontario, K2B 8K2 Canada
kevin@limgeomatics.com | 613-686-5735

Geospatial Solutions

Pickett provides aerial LiDAR, aerial mapping and imaging, land surveying, hydrographic surveying and engineering services to clients throughout the US and Caribbean. Pickett specializes in offering the simultaneous collection of high resolution Aerial Imagery combined with engineering-grade airborne LiDAR, allowing us to turn around baseline imagery and LiDAR-derived data quickly and efficiently. We deliver CADD and GIS-ready products to meet unique client specifications. Our clients come to us for the most complex projects because of our proven track record of producing deliverables efficiently, safely, cost-effectively and on schedule. With over 60 years of experience, we have established ourselves as leaders and innovators in the surveying and geospatial industry. Contact us today to see how our geospatial services can benefit next your project.

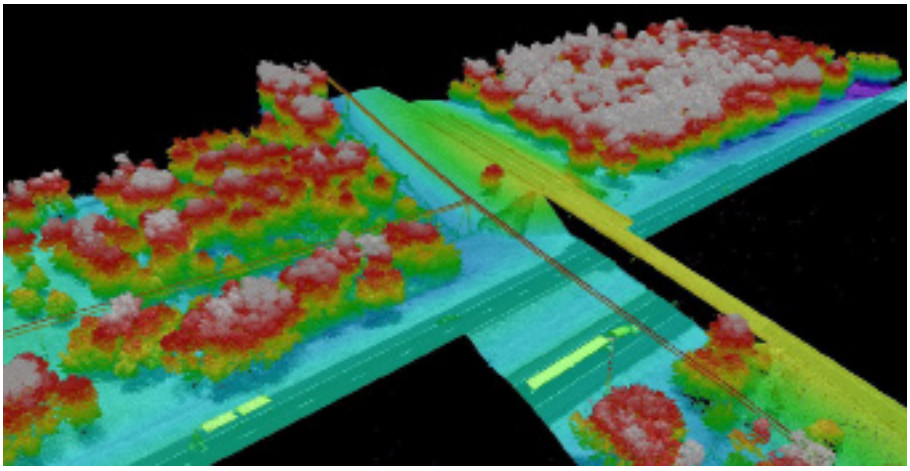

The Teledyne Optech G2 LiDAR System and Optech Galaxy T2000 LiDAR sensor are some of the many tools we use for a myriad of LiDAR applications. When used in conjunction with our Phase One iXU-RS 1000 and iXM-RS150F medium-format cameras, these systems produce a complete picture of site conditions.

The Optech G2 LiDAR System and Optech Galaxy PRIME LiDAR sensor are some of the many tools we use for a myriad of LiDAR applications with point densities up to 150 points per square meter. When used in conjunction with our iXU-RS 1000 medium-format camera, this system produces a complete picture of site conditions.

In the energy sector, we perform aerial surveys of corridors with lengths of 1 mile to 100 miles, with a point density of 50 points per square meter, or more. For the mining sector, we provide aerial surveys ranging in size from 1-acre stockpiles to several thousand acres, using the data to create digital surfaces and compute high-accuracy volumes for accounting purposes. Land development projects range in size from 20 acres to 100 square miles, and occasionally more, finalizing into a detailed topographic survey.

We utilize a RIEGL terrestrial scanner for smaller projects where high-resolution, high-accuracy LiDAR data is required. In combination with the top-mounted DSLR camera, we can create photo-realistic point clouds to survey and document as-built conditions of almost any feature.

Our aerial platform consists of a 2015 Cessna T-206H Turbo Station Air and a 1981 Cessna T-210N Turbo Centurion, both modified with FAA approved camera ports for aerial surveys. Pickett has multiple Unmanned Aerial Systems, and complies with FAA Part 107 regulations, to provide UAS services commercially

Pickett and Associates, LLC
5010 West Nassau Street
Tampa, FL 33607
(813) 877-7770 | Info@PickettUSA.com
www.pickettusa.com

PICKETT®

Fundamentals of Capturing and Processing Drone Imagery and Data

Amy E. Frazier and Kunwar K. Singh, Eds.

CRC Press: Boca Raton, FL. 2021. Xxiii and 361 pp., diagrams, maps, photos, images, index. Electronic copy. $130.00(hbk), $91.00(ebk) ISBN: 978-0-367-24572-6 (hbk), 978-1-032-02249-9 (pbk), 978-0-429-28323-9 (ebk).

Reviewed by M.Kathryn Rocheford, PhD, Research Archaeologist, Minnesota Historical Society, Saint Paul, Minnesota.

The editors have compiled a tremendous tome that includes contributions from a multitude of authors have met their reported goal for this book to be accessible to someone with little or no training in collecting and processing drone imagery and data. The editors, Frazier and Singh, have organized the contents of the book in two parts. The Introduction in Part I lays out the contents of the book in tantalizing detail to support picking and choosing the topic(s) of interest. Part I goes on to outline drone terminology and a variety of their real-world applications, as well as an introduction to the concepts of remote sensing and photogrammetry as they pertain specifically to drones. It then presents the specifics for sensor selection, flight planning, drone regulations, and imagery processing using structure from motion (SfM).

The second part of the book provides users with twelve real-world applications written with learning objectives, detailed instructions, and discussion and synthesis questions, making this book a valuable source for students and educators. Data for the hands-on exercises are provided through a web link in the book's introduction. However, the first file to "load" for Chapter 8 is not included in the data set but using the next data set works. The software utilized for the exercises is either free or trial downloads are available, and the links to access them are in the instructions. As the authors noted, every publication that provides links to external websites is prone to broken links and this book is no exception. For example, the Chapter 8 link to the Mission Planner software is not correct, it directs you to the main ArudPilot page and there is no menu panel on the left. However, a quick Google search for Mission Planner ArduPilot will take you to the menu panel. In addition, the ArduPilot site has changed the menu item for First Time Setup. It has been removed and will take some technical savvy to get to the right place. Most instructors know that published computer exercises need to be tested so that minor changes like these can be debugged before giving them to students.

The editors and contributing authors do an excellent job of synthesizing a variety of topics within the context of drone captured imagery and data that are supported with plenty of references for those who want to dig in deeper. Synthesizing the art and science for drone applications was not an easy task, as each topic has a variety of applications other than drones, (e.g., electromagnetic energy, sensor technology, and structure from motion). Instructors and students alike will recognize the basic concepts from other course work and be able to expand their knowledge into the use of drones.

The twelve Hands-On Applications provide enough content for a typical college semester of 15 weeks. Each chapter provides a real-world application from the foundational chapters: Planning Unoccupied Aircraft Systems (UAS) Missions and Aligning and Stitching Drone-Capture Images, to utilization of data from specific sensors, including RGB and multispectral, point cloud from SfM, as well as sensors to measure atmospheric parameters. Recognizing the expense of lidar equipment and the issue with payload mentioned by the authors, this reviewer wanted to see an example that utilized lidar data obtained using a UAS. Finally, there is a variety of discipline specific applications including wildlife management (Chapter 10), vegetation assessment (Chapters 11 & 13), geomorphology (Chapters 14 & 15), cultural resource management (Chapters 16 & 17), and atmospheric monitoring (Chapters 18 & 19), providing something for

continued on page 409

Photogrammetric Engineering & Remote Sensing
Vol. 89, No. 7, July 2023, pp. 405,409.
0099-1112/22/405, 409

doi: 10.14358/PERS.89.7.405

The layman's perspective on technical theory and practical applications of mapping and GIS

MAPPING MATTERS

YOUR QUESTIONS ANSWERED

by Qassim Abdullah, Ph.D., PLS, CP
Woolpert Vice President and Chief Scientist

- **Have you ever wondered about what can and can't be achieved with geospatial technologies and processes?**
- **Would you like to understand the geospatial industry in layman's terms?**
- **Have you been intimidated by formulas or equations in scientific journal articles and published reports?**
- **Do you have a challenging technical question that no one you know can answer?**

If you answered "YES" to any of these questions, then you need to read Dr. Qassim Abdullah's column, Mapping Matters.

In it, he answers all geospatial questions—no matter how challenging—and offers accessible solutions.

Send your questions to Mapping_Matters@asprs.org

To browse previous articles of Mapping Matters, visit http://www.asprs.org/Mapping-Matters.html

"Your mapping matters publications have helped us a lot in refining our knowledge on the world of Photogrammetry. I always admire what you are doing to the science of Photogrammetry. Thank You Very much! the world wants more of enthusiast scientists like you."

"I read through your comments and calculations twice. It is very clear understandable. I am Honored there are experienced professionals like you, willing to help fellow members and promote knowledge in the Geo-Spatial Sciences."

YOUR COMPANION TO SUCCESS

GIS Tips & Tricks

By Al Karlin, Ph.D. CMS-L, GISP

File Navigation is Easier than You Think

For novices entering into the Esri GIS world from an Apple-iOS™ environment, which is a common occurrence for my beginning GIS students, they have to overcome not only the intricacy's and complexities of the GIS software, but also navigating through a MicroSoft™ Windows filing system, maybe for the first time. For many beginners these are both daunting tasks but even more so for those trying to access GIS data either on their local disks or on a network. Fortunately, the ArcGIS Pro interface provides several tools to construct shortcuts to often-used data paths. The Add Folder Connections tools are available in ArcGIS Pro, and similar tools in ArcGIS Desktop, make short work to finding data in a challenging file system.

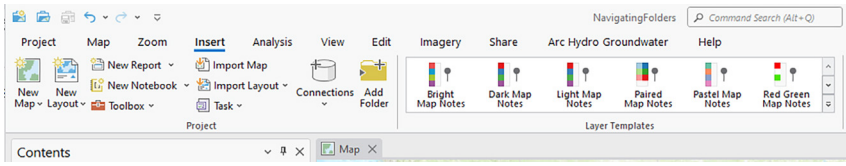

Figure 1. The ArcGIS Pro starting ribbon showing the Insert Tab and the Add Folder tool.

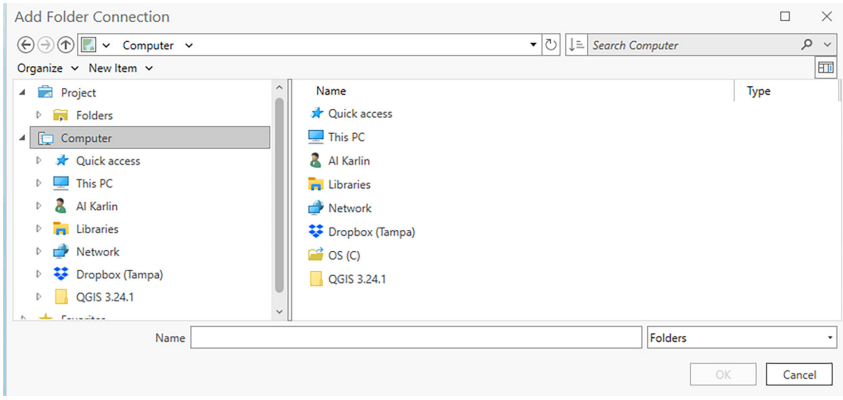

Figure 2. The Add Folder Connection file navigation dialog box activated from the Add Folder tool.

Adding a Folder from the Insert Tab in ArcGIS Pro

When starting an ArcGIS Pro project (.aprx) the Map tab opens with a basemap and the ribbon starts on the "Insert" tab as in Figure 1.

In the Project group, clicking on the "Add Folder" icon will start a standard Windows™ file navigator (Figure 2) that you can use to navigate to a folder for quick repeat navigation. The target folder may contain images, GIS data, or other useful files to your project. Simply navigate through the file system to your desired target folder.

When you find the folder that you want to connect to your project, as in this example, I navigated through my Professional\GISData folders to find the \Alaska folder, then I select it (left-click) and clicked OK (Figure 3).

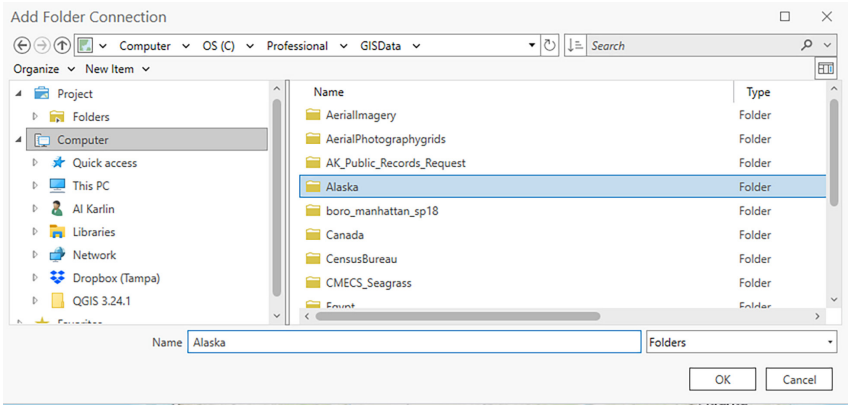

Figure 3. Navigating to and selecting a windows file folder to add to the project Folder.

This will place the \Alaska folder in my project's "Folder" file so that when I use the "Add Data" tool on the Map | Layer group, the desired folder will appear (Figure 4, right pane) ready for use; no additional file navigation necessary.

Photogrammetric Engineering & Remote Sensing
Vol. 89, No. 7, July 2023, pp. 407-409.
0099-1112/22/407-409

doi: 10.14358/PERS.89.7.407

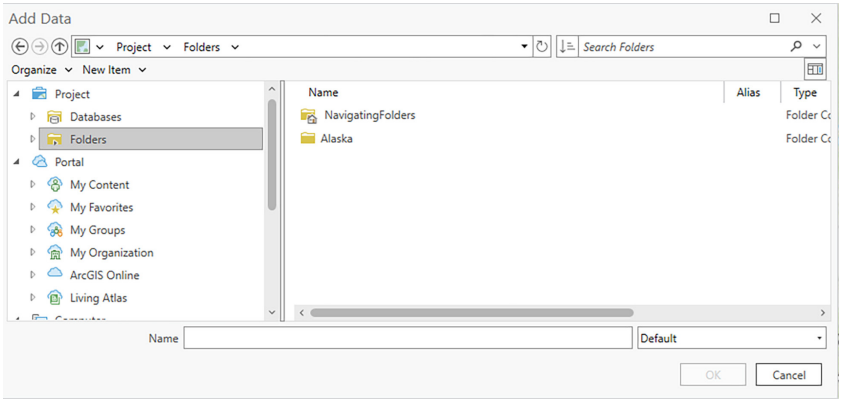

Figure 4. The ArcGIS Pro project Folder, as accessed from the Add Data tool, showing the folder previously attached to the project from Figure 3.

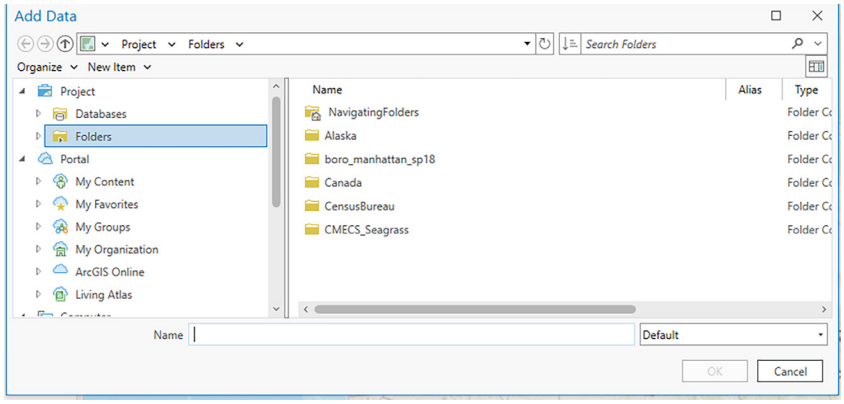

Figure 5. The ArcGIS Pro project Folder, as accessed from the Add Data tool, showing the multiple folders attached to the project by using the Shift + Select tip.

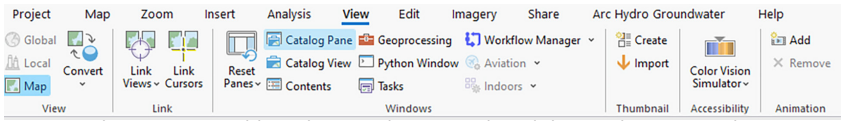

Figure 6. The ArcGIS Pro ribbon showing the View Tab and the Catalog Pane in the Windows group.

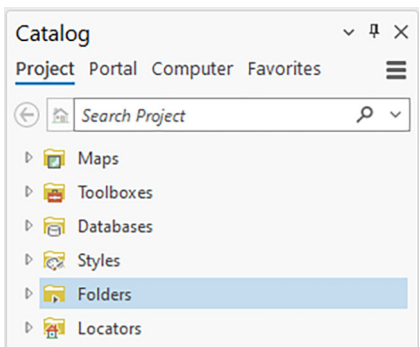

Figure 7. Opening the Catalog pane shows the project's Folders icon with an expand arrow to the left of the folder.

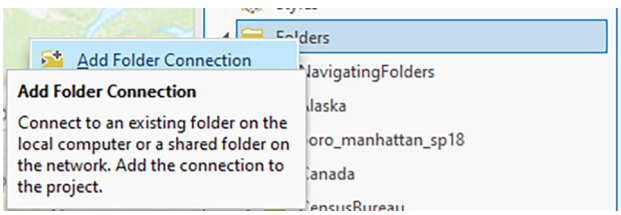

Figure 8. Adding a Folder Connection using the Catalog pane.

TIP #1 — You can add multiple paths (Figure 5) to your project's "Folder" by holding the SHIFT key while you Select (left-click) on folders to add. In this case, I added the \boro_manhattan_sp18, \Canada, \CensusBureau and \CMECS_Seagrass folders using the Shift+Select combination.

Adding Folders from the Catalog Pane to ArcGIS Pro

If you are like me, you are accustomed to having a Catalog pane (what used to be ArcCatalog) handy to manage your files. I strongly encourage my students to follow this practice.

TIP #2 — From the View tab (Figure 6) on the ribbon, in the Windows group, open a Catalog Pane and dock the Catalog pane (or float it) as you like. (I generally dock it on the right-hand side of the canvas.)

When you open the Catalog pane, you see the "Folders" (Figure 7). Right-clicking on the "Folders" starts the "Add Folder Connection" (Figure 8) which will open a Windows File navigator as in Figure 2. Of course, you can use the Shift + Select combination to choose multiple folders.

TIP #3 — Right-clicking on any individual folder icon, gives you additional options for managing that connected folder (Figure 9).

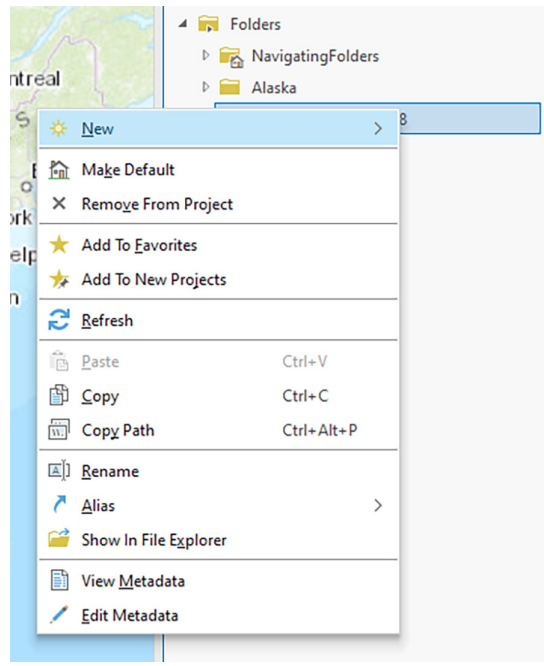

Figure 9. Right-clicking on a folder from the Catalog pane reveals additional file management options.

Adding a Folder in ArcGIS Desktop

For those using ArcGIS Desktop, Connect to Folder from the ArcMap interface is a bit different. The Connect to Folder tool is available only from the "Add Data" button. After the "Add Data" button is pressed, the Windows file navigator displays several optional icons along the top of the file browser, including the "Connect to Folder" icon. When this icon is selected (Figure 10), the Connect to Folder (Figure 11) will allow you to navigate and connect to a folder.

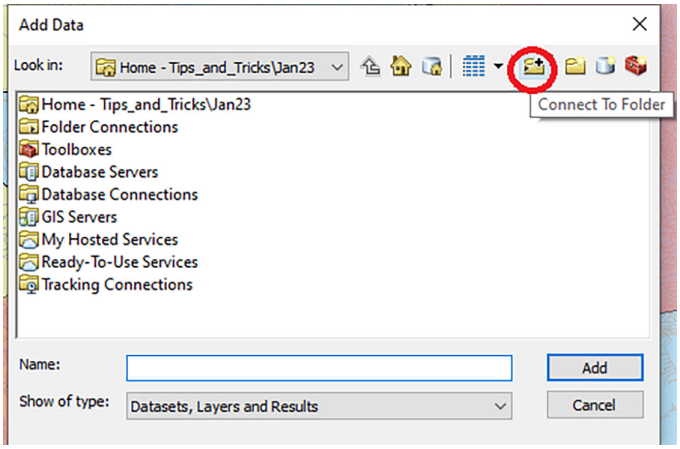

Figure 10. In ArcMap Desktop, the Connect to Folder icon is located on the Add Data dialog box.

Unfortunately, if you need to connect to multiple folders, you will need to navigate to each separately; the Shift + Select combination does not work.

Finally, from ArcCatalog or a Catalog Window in ArcMap, you can also right-click on the "Folder Connections" to Connect to Folder (Figure 12) in much the same way as in ArcGIS Pro (Figure 8).

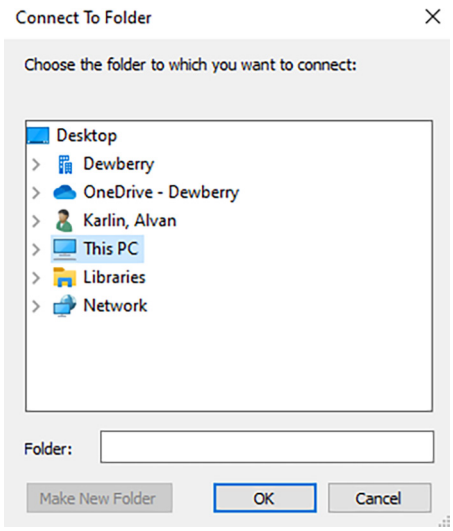

Figure 11. The Connect to Folder dialog box and navigator in ArcMap Desktop

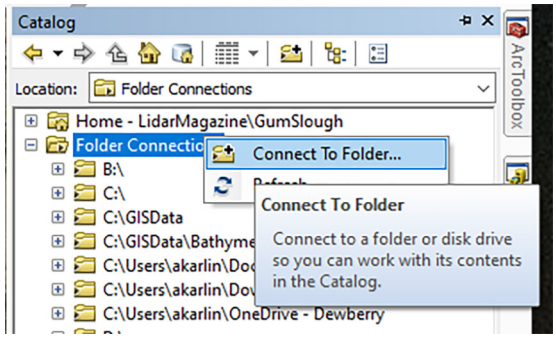

Figure 12. The Connect to Folder tool in ArcCatalog or a Catalog Window in ArcMap Desktop.

While learning to navigate through a Windows™ file system may initially be a challenge to iOS™ (and other) users, connection to folders in the ArcGIS environment certainly helps overcome some of those difficulties.

Send your questions, comments, and tips to GISTT@ASPRS.org.

Al Karlin, Ph.D., CMS-L, GISP *is a senior geospatial scientist with Dewberry's Geospatial and Technology Services group in Tampa, FL. Al works with all aspects of lidar, remote sensing, photogrammetry, and GIS-related projects. Al also teaches Mapmaking for the Social Sciences at the University of Tampa.*

BOOK**REVIEW** *continued from page 405*

cultural and natural science disciplines. While there are additional sensors (e.g., lidar, thermal infrared) and discipline specific applications that are not included in this tome (e.g., fire and emergency response, civil engineering, and forensic investigations), the array of sensor technologies across disciplines is impressive. In addition, the foundations provided in this book would support incorporation of additional sensors and would be portable to other disciplines. This book is one of the best foundational books providing enough theoretical background that is accessible to a novice and exemplary hands-on applications for users to gain experience with real-world data. I highly recommend this book for independent learners, as well as educators for incorporation as a text/lab book.

STAND OUT FROM THE REST

EARN ASPRS CERTIFICATION

ASPRS congratulates these recently Certified and Re-certified individuals:

RECERTIFIED MAPPING SCIENTIST LIDAR

Azadeh Koohzare, Certification #R019L
Effective February 14, 2023, expires February 14, 2028

Susan Hessefort, Certification #R022L
Effective January 31, 2023, expires January 31, 2028

Bartley Wade Estes, Certification #R027L
Effective June 20, 2023, expires June 20, 2028

Terry J. Keeton, Certification #R028L
Effective August 4, 2023, expires August 4, 2028

RECERTIFIED PHOTOGRAMMETRIST

Thomas R. Freeman, Certification #R1360CP
Effective June 23, 2023, expires June 23, 2028

Paul Kokes, Certification #R1194CP
Effective December 5, 2020, expires December 5, 2025

Luiz H. Cortes, Certification #R1546CP
Effective March 21, 2023, expires March 21, 2028

Daniel Rorrer, Certification #R1047CP
Effective February 19, 2023, expires February 19, 2028

Mark Safran, Certification #R1350CP
Effective March 7, 2023, expires March 7, 2028

CERTIFIED MAPPING SCIENTIST LIDAR

Gregory Stamnes, Certification #L078
Effective March 10, 2023, expires March 10, 2028

RECERTIFIED MAPPING SCIENTIST RS

Raymond A. Miller, Certification #R208RS
Effective October 26, 2022, expires October 26, 2027

CERTIFIED UAS TECHNOLOGIST

Alex Olsen-Mikitowicz, Certification #UAS-T041
Effective April 3, 2023, expires April 3, 2026

RECERTIFIED LIDAR TECHNOLOGIST

Andrew Verville, Certification #R049LT
Effective April 1, 2023, expires April 1, 2026

CERTIFIED LIDAR TECHNOLOGIST

Brett Allen Cox, Certification #LT079
Effective April 17, 2023, expires April 17, 2026

Brock Riebe, Certification #LT080
Effective May 10, 2023, expires May 10, 2026

Hans Knoepfel, Certification #LT081
Effective May 13, 2023, expires May 13, 2026

RECERTIFIED GIS/LIS TECHNOLOGIST

Taylor Moore, Certification #R302GST
Effective May 19, 2023, expires May 19, 2026

ASPRS Certification validates your professional practice and experience. It differentiates you from others in the profession. For more information on the ASPRS Certification program: contact **certification@asprs.org,** visit **https://www.asprs.org/general/asprs-certification-program.html.**

asprs THE IMAGING & GEOSPATIAL INFORMATION SOCIETY

ASPRS PARTICIPATING IN GEO WEEK — FEBRUARY 2024!

Geo Week is the premier event for increased integration between the built environment, advanced airborne/terrestrial technologies, and commercial 3D technologies, bringing together former stand-alone events AEC Next Technology Expo & Conference, International Lidar Mapping Forum, and SPAR 3D Expo & Conference, and powerful partnership events including ASPRS Annual Conference.

Geo Week was created as a response to the changing needs of built world and geospatial professionals, and to acknowledge the convergence of technology taking place currently. New technological innovations, the need for remote workflows, and hardware breakthroughs are redefining expectations across teams, organizations, and entire industries. Geo Week is at the center of it all.

The ASPRS program at Geo Week 2024 will include technical sessions, continuing education workshops, committee meetings, and a student-focused Academic Hub.

NEW ASPRS MEMBERS

ASPRS would like to welcome the following new members!

Mercy Onaopemipo Akintola
Andrew A. Andrews
Mohsen Arjmand
Adamu Bala
Mounika Bondada
Rin Dakai
Deniz Bilge Demir
Leena Dhruwa
Dayna Dominguez
Anirudh Edpuganti
Bhoomika Ghale
Jacob Hart
Syed Zohaib Hassan
Shashank Karki
Rupak Karn
Shanti Kumari
Mona Latil-Quinn
Shailja Mamgain
Margot Mattson
Baleseng Tlholohelo Mokoena
Dasti Sardar Muhammad Yousaf, Sr.
Chidinma Godsgood Ndu
Judith Oppong
Jeremy Powell
Dolonchapa Prabhakar
Muhamad Hanif Resgi Putranto
Barira Rashid
Onteddu Chaitanya Reddy
Elçin Sari
Matthew Serenita
Jamen Dean Underwood
Balla Vivek, Ph.D.
Sajith Variyar VV
Tang Xueying

FOR MORE INFORMATION ON ASPRS MEMBERSHIP, VISIT
HTTP://WWW.ASPRS.ORG/JOIN-NOW

PUBLISHING OPEN-ACCESS IN *PE&RS* IS NOW EASIER!

ASPRS is changing the subscription model of our monthly journal, *PE&RS*. ASPRS is waiving open-access fees for primary authors from subscribing institutions. Additionally, primary authors who are Individual Members of ASPRS will be able to publish one open-access article per year at no cost and will receive a 50% discount on open-access fees for additional articles.

- **Open Access matters!** By providing unrestricted access to research we can advance the geospatial industry and provide research that is available to everyone.
- **Institutions and authors receive more recognition!** Giving permission to everyone to read, share, reuse the research without asking for permission, as long as the author is credited.
- **Reputation matters!** Known for its high standards, *PE&RS* is the industry leading peer-review journal. Adding open access increases authors' visibility and reputation for quality research.
- **Fostering the geospatial industry!** Open access allows for sharing without restriction. Research is freely available to everyone without an embargo period.

Under the previous subscription model, authors and institutions paid $1500 or more in open-access fees per article. This will represent a significant cost savings. Open-access publications benefit authors through greater visibility of their work and conformance with open science mandates of funding agencies.

Subscriptions asprs.org/subscribe
Membership asprs.org/membership

asprs THE IMAGING & GEOSPATIAL INFORMATION SOCIETY

A Lightweight Conditional Convolutional Neural Network for Hyperspectral Image Classification

Linfeng Wu, Huajun Wang, and Huiqing Wang

Abstract

Deep learning (DL), especially convolutional neural networks (CNNS), has been proven to be an excellent feature extractor and widely applied to hyperspectral image (HSI) classification. However, DL is a computationally demanding algorithm with many parameters and a high computational burden, which seriously restricts the deployment of DL-based HSI classification algorithms on mobile and embedded systems. In this paper, we propose an extremely lightweight conditional three-dimensional (3D) HSI with a double-branch structure to solve these problems. Specifically, we introduce a lightweight conditional 3D convolution to replace the conventional 3D convolution to reduce the computational and memory cost of the network and achieve flexible HSI feature extraction. Then, based on lightweight conditional 3D convolution, we build two parallel paths to independently exploit and optimize the diverse spatial and spectral features. Furthermore, to precisely locate the key information, which is conducive to classification, a lightweight attention mechanism is carefully designed to refine extracted spatial and spectral features, and improve the classification accuracy with less computation and memory costs. Experiments on three public HSI data sets show that the proposed model can effectively reduce the cost of computation and memory, achieve high execution speed, and better classification performance compared with several recent DL-based models.

Introduction

With the development of hyperspectral sensors, the spatial resolution and the number of spectral bands in the hyperspectral image (HSI) have greatly increased. Compared with multispectral and natural Red-Green-Blue images, the abundant spatial and spectral information provided by HSI can be used to more accurately identify ground objects containing different materials. Therefore, hyperspectral image classification, which classifies each image pixel into specific labels, has attracted great attention in many real applications around the world, such as vegetation ecology (Liang *et al.* 2015), atmospheric science (Liu *et al.* 2022), geology and mineral resources (Jain and Sharma 2019; Peyghambari and Zhang 2021), marine research (Serranti *et al.* 2018) and precision agriculture (He *et al.* 2018). However, high-dimensional HSIs have few training samples and large spatial variability of spectral features, which brings great difficulties to hyperspectral classification.

In the past decades, many traditional machine learning algorithms have been proposed to classify HSI, such as support vector machine (SVM) (Tarabalka *et al.* 2010), random forest (Abdel-Rahman *et al.* 2013) and k-nearest neighbor (Ma *et al.* 2010). These methods usually only consider spectral information, and feature extraction is not sufficient. Therefore, other traditional machine learning algorithms also consider spatial information, such as extended morphological profiles (Quesada-Barriuso *et al.* 2014), composite kernels (Zhou *et al.* 2015), and sparse representation (Wang *et al.* 2015), and the results are more satisfactory. However, traditional machine learning algorithms use hand-crafted features, which are relied heavily on expert knowledge. In addition, the hand-crafted features are not enough to discriminate subtle variation, which restricts the classification performance.

In recent years, inspired by the successful application of deep learning in image classification (Krizhevsky *et al.* 2012), object detection (Girshick *et al.* 2014), and natural language processing (NLP) (Bordes *et al.* 2012), deep learning (DL) has also been applied to HSI classification and achieved good performance. Compared with machine learning algorithms, deep learning can effectively extract hierarchical and nonlinear features via a series of hierarchical layers. For example, lower layers can extract shallow and simple features, and the deeper layers can represent more abstract features. In addition, different networks focus on extracting different feature types, which makes deep learning more suitable for dealing with various situations. In the remote sense community, DL-based methods demonstrate extremely promising results. For example, a stackable auto-encoder network introduced the concept of deep learning into hyperspectral data classification for the first time (Chen *et al.* 2014). To avoid loss of detailed information caused by dimension reduction methods such as principal component analysis and negative matrix factorization, the restricted Boltzmann machine and deep belief networks (Li *et al.* 2014) are introduced in to realize the feature extraction and classification. With the development of DL, many advanced networks have been effectively used to solve HSI classification tasks (Ahmad *et al.* 2022) with different degrees of success. For example, a spectral-spatial residual network (SSRN) (Zhong *et al.* 2018) is proposed to jointly extract spectral and spatial features. An integration of multiple convolutional neural networks (CNN) (Sikakollu and Dash 2021) is proposed to generate more reliable and robust prediction results. To highlight the most critical spectral and spatial information, a double-branch dual-attention mechanism three-dimensional (3D)-CNN (Li *et al.* 2020) is proposed, and satisfactory results are obtained in a small number of training samples. However, in terms of the visual invariance of CNN's fixed-size convolution kernel, the visual transformation of the input image will lead to the instability of the network performance. To overcome this problem, some methods introduced the concept of NLP to explain the process of image classification from a new perspective. Motivated by the self-attention mechanism (Vaswani *et al.* 2017) and recurrent neural network (Paoletti *et al.* 2020), vision transformers (VIT) (Hong *et al.* 2021) reconsideration of the input image as a sequence of tokens to capture long-range dependence, have also become popular. In addition, generative adversarial network (Zhan *et al.* 2018; Zhong *et al.* 2020) create artificial instances from data sets, while retaining features similar to the original set, which alleviates the problems of class imbalance and the limited number of labeled samples.

However, most existing work tends to improve classification accuracy at the cost of complex models and many training samples. For computationally intensive deep learning algorithms, the complexity

Linfeng Wu and Huajun Wang are with Chengdu University of Technology, College of Geophysics, Chengdu, China, 610059 (wulinfeng@stu.cdut.edu.cn).

Huiqing Wang is with Southwest Medical University, Information Technology Education Center, Luzhou, China, 646000.

Corresponding author: Linfeng Wu (wulinfeng@stu.cdut.edu.cn)

Contributed by Qunming Wang, December 7, 2022 (sent for review February 9, 2023; reviewed by Jiayi Li, Huapeng Li).

Photogrammetric Engineering & Remote Sensing
Vol. 89, No. 7, July 2023, pp. 413–423.
0099-1112/22/413–423

doi: 10.14358/PERS.22-00130R2

of the models increases, making them difficult to deploy on embedded systems for mobile and airborne devices, with low power, memory, and computational resources. The characteristics of these embedded systems pose new challenges to the design of DL algorithms and promote the development of more efficient algorithms with fewer sample requirements. In general, lightweight neural network design methods can be divided into three directions: neural architecture search (Wu *et al.* 2019; Liu *et al.* 2021), neural network compression (Choudhary *et al.* 2020; Deng *et al.* 2020), tight architecture design (Huang *et al.* 2018; Wang *et al.* 2020). Among them, tight architecture design is a structured improvement scheme, which focuses on reducing the connection between feature mapping channels by changing the standard convolution and fully connected layer, to reduce the parameters and computation. The neural network designed by this method can conveniently and effectively cooperate with other strategies to improve the overall expression ability of the model, so it has great development potential. In ShuffleNet (Zhang *et al.* 2018), group convolution divides the output feature maps of the previous layer into several groups, and each group performs convolution operations respectively, to reduce the computation of convolution. To overcome the problem of information flow between different groups, ShuffleNet-V2 (Ma *et al.* 2018) scrambles the feature map of each channel after group convolution, so that each group can obtain the feature information extracted by other groups. The strategy of grouping and shuffling the standard convolution is equivalent to decomposing the global channel feature extraction into two stages: local channel feature extraction and channel shuffling. This strategy promotes the study of more efficient convolution methods. The depth-wise separable (DWS) convolution (Sandler *et al.* 2018) separates the standard convolution operation into depth-wise (DW) convolution and point-wise (PW) convolution, thus reducing many parameters and computation brought by the standard convolution. Furthermore, to improve the efficiency of feature extraction, the ghost network (Han *et al.* 2020) uses a series of linear transformations with low cost to generate more feature maps.

Based on the above-mentioned knowledge, several HSI classification methods have been proposed to overcome these difficulties to increase computational efficiency and reduce the number of parameters. In lightweight convolutional neural network (LWCNN) (Jia *et al.* 2021), a spatial-spectral Schroedinger eigenmaps is introduced to compress the spectral dimension to significantly reduce the number of parameters. However, the dimensionality reduction method leads to the loss of some details of the raw HSI data. To address the issue, some works use DWS convolution (Zhang *et al.* 2019; Wang *et al.* 2022) to extract features directly from raw HSI data. In Ghostnet (Paoletti *et al.* 2021), the ghost module composed of a significantly lighter convolution and a cheap linear layer replaces standard convolution to extract spectral-spatial features to reduce the computing cost. However, the simple decomposition of standard convolutions (such as ghost module and DWS convolution) has two drawbacks.

First, the standard one-step convolution is decomposed into smaller multistep convolutions, which leads to a significant increase in network depth. With the increase of network depth, the extracted features gradually disappear in the transmission process, resulting in gradient disappearance and model degradation.

Second, blindly reducing the number of parameters and model size will easily lead to the performance degradation of the model, which is contrary to the purpose of lightweight design.

To provide appropriate answers to the above problems, this work proposes a new hyper-light model for HSI classification. First, to reduce the complexity of the model, a two branch shallow network is constructed, where the two-branch structure extracts rich spatial and spectral features independently to ensure the diversity of features and reduce the loss of information. Second, dense connection (Huang *et al.* 2017), which connects each convolution layer to every other layer in a feedforward manner, is used to enhance the transmission of features and alleviate gradient vanishing. Third, we developed a lightweight DWS conditional convolution unit to replace the standard convolution, which improves the representation capability of the model with fewer parameters and higher computational efficiency. Furthermore, to extract more valuable spatial and spectral information and reduce the interference of useless information, a lightweight attention mechanism, which we called merge attention, is proposed to refine features and improve classification accuracy.

The rest of this paper is organized as follows: In the section "Methods", we will introduce the proposed method, including DWS conditional convolution, merging attention mechanism, and the implementation details of the dual branch network. To verify the effectiveness of our work, the experimental results and necessary analysis are presented in the section "Experimental Results", and the section "Discussion". Finally, we summarize our work in the "Conclusion" section.

Methods

DWS Conditional 3D Convolution

HSI raw data is usually represented as a cube containing one-dimensional spectral information and two-dimensional (2D) spatial information, so it is natural to use 3D convolution to express the relationship between objects in 3D space. Recently, many HSI classification frameworks have applied 3D convolution to jointly extract rich spectral and spatial information (Jia *et al.* 2021; Paoletti *et al.* 2021). Given n_1 input data x, the i^{th} output of the $l+i^{\text{th}}$ 3D convolution layer can be formulated as:

$$x_i^{l+1} = \sum_{j=1}^{n_l} W_i^{l+1} x_j^l + b_i^{l+1} \tag{1}$$

where x_j^l represents the j^{th} output feature map of the l^{th} 3D convolution layer. W_i^{l+1} and b_i^{l+1} stand for the weights and biases of the $l+1^{\text{th}}$ 3D convolution layer, respectively. In addition, Data Normalization (DN) (Ioffe and Szegedy 2015) layer and Gaussian error linear units (DN) (Hendrycks and Gimpel 2016) layer are added after each 3D convolution layer. DN makes the distribution of features at each layer of the network as stable as possible. DN learns the nonlinear relationship of data. DN and GELU are represented as follows:

$$\hat{x} = \frac{x - E(x)}{\mathrm{Var}(x)} \tag{2}$$

$$\mathrm{GELU}(\hat{x}) = \frac{\hat{x}}{2} \cdot \left[1 + \mathrm{erf}\left(\frac{\hat{x}}{\sqrt{2}} \right) \right] \tag{3}$$

where x is the input data of the DN layer, and $\hat{x}$ is the output data of the DN layer.

Based on the above knowledge, we can observe that simply stacking standard convolution units and expanding the size of the convolution kernel will generate many learnable parameters and bring a lot of computational burdens. In addition, in the standard convolution, the same convolution kernel parameters are used for all input samples, which limits the representation capability of the model. Recently, a conditional convolution (CondConv) (Yang *et al.* 2019) is proposed to improve the expression ability of the model, in which multiple parallel convolution kernels are aggregated into a dynamic kernel, and weights are adaptively combined according to the input features. Figure 1a and 1b show the structure of conditional convolution and standard convolution, respectively. In standard convolution, the convolution kernel parameters are determined by training and treating all input samples equally, while in conditional convolution, the convolution kernel parameters are obtained by calculating the weighted convolution kernel of the input image by multiple experts. Therefore, conditional convolution can adaptively adjust the convolution parameters according to the input image. In addition, the improvement of standard convolution capacity depends on the expansion of convolution kernel size and channel number, which will further increase the computational burden of the model. However, conditional convolution only needs to increase

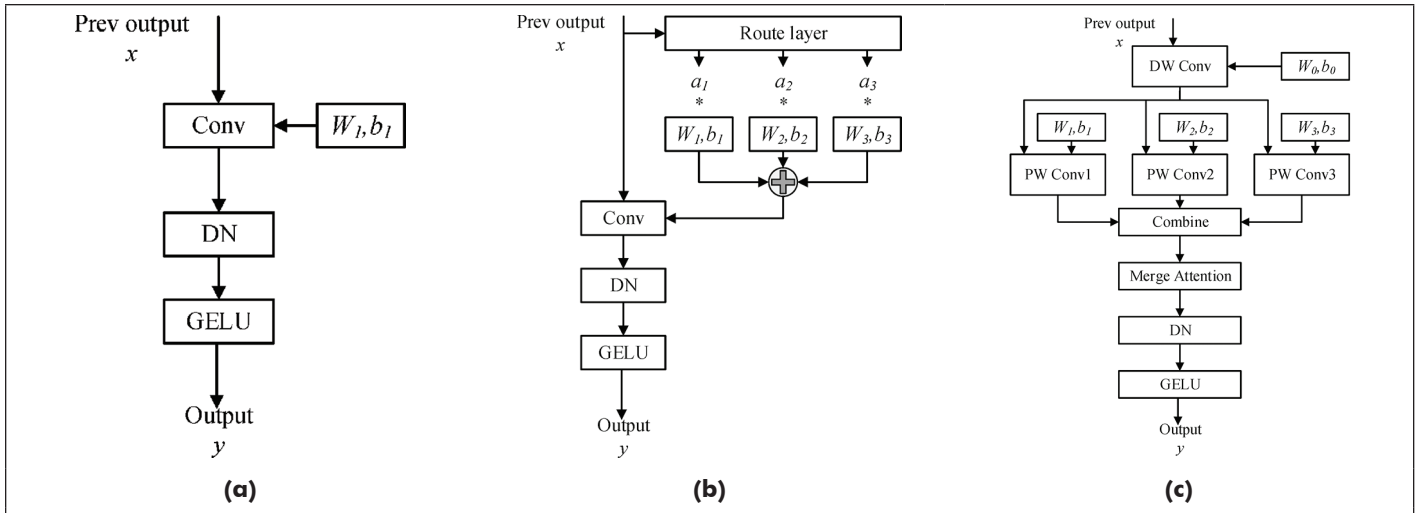

Figure 1. Structures of: (a) standard convolution, (b) conditional convolution with three kernels, and (c) proposed depth-wise separable (DWS) conditional convolution with three kernels. DN = Data Normalization; GELU = Gaussian error linear units.

the number of experts before performing the convolution operation. Motivated by it, we developed a lightweight- and attention-assisted DWS conditional convolution unit to replace the standard convolution, which improves the representation capability of the model with fewer parameters and higher computational efficiency.

The structure of the DWS conditional convolution is shown in Figure 1c. To achieve a lightweight structure for easy deployment on embedded systems, we separate the standard conditional convolution into two steps: DW convolution and PW convolution. First, DW convolution applies a convolution kernel in each channel of the input data, and then splices the outputs of all convolution kernels to obtain its final output. In DW convolution, each channel of the input cube is assigned one convolution kernel. Therefore, numerous parameters are reduced. Second, multiple cheap PW convolutions with the size of 1×1×1 to realize single-channel-level fusion for the output data from the DW convolution to further decompose and refine the standard conditional convolution. In addition, compared to the standard conditional convolution, multiple parallel convolutions select different parameters to extract features, which can effectively improve the representation capability of the model and achieve flexible HSI feature extraction. The output y of DWS conditional convolution can be expressed mathematically as:

$$y = \sum_{i=1}^{n} \left(W_i * (W_0 * x + b_0) + b_i \right) \tag{4}$$

where x is the input of DWS conditional convolution, n is the number of convolution kernels, and * is the convolution operation. W_0 and b_0 are the bias and weights for DW convolution operation, respectively. W_i and b_i are the bias and weights for PW convolution operation, respectively.

We can estimate the floating-point operations per second (FLOPS) theoretically reduced by the DWS conditional convolution unit. Assume standard 3D convolution $W_s \in R^{C_{in} \times K \times K \times K \times C_{out}}$, the DWS conditional convolution composed by DW convolution $W_d \in R^{C_{in} \times K \times K \times K}$, and the n PW convolution $W_p \in R^{C_{in} \times 1 \times 1 \times 1 \times C_{out}}$, the reduced FLOPS can be written as follows:

$$\frac{\text{FLOPs}_{\text{dwscc}}}{\text{FLOPs}_{\text{sc}}} = \frac{K^3 \cdot C_{\text{in}} \cdot P^3 + C_{\text{in}} \cdot P^3 \cdot C_{\text{out}} \cdot n}{K^3 \cdot C_{\text{in}} \cdot P^3 \cdot C_{\text{out}}} = \frac{1}{C_{\text{out}}} + \frac{n}{K^3} \tag{5}$$

where P is the size of input cube, K represents the size of the convolution kernel. C_{in} and C_{out} represent the number of channels of the input and output data, respectively.

Let us consider a practical example, a standard 3×3×3 convolution applied to 12, 9×9×9 input cubes to generate 24, 9×9×9 output cubes, required 12×3×3×3×24 = 7776 parameters (assume that the padding size is 1). For CondConv with three kernels, required 12×3×3×3×24×3 = 23 328 parameters. For DWS conditional convolution composed by the 3×3×3 DW convolution with group size 12 and the 1×1×1 PW convolution with three kernels, only required 12×3×3×3+12×3 = 1188 parameters. Figure 2 provides a graphical representation of the entire process. In addition, according to Equation 5, theoretically, DWS conditional convolution can reduce the FLOPS consumed by standard convolution by about nine times.

Merge Attention Mechanism

The attention mechanism (AM) enables the model to focus on important information and ignore irrelevant information, which has been widely proven to effectively improve the performance of CNN (Fu *et al.* 2019; Huang *et al.* 2019). However, most existing methods focus on developing more complex AMs to achieve better performance, which will inevitably increase the complexity of the model. To balance the performance and complexity, we designed a lightweight merge AM, which is embedded in the DWS conditional convolution unit to improve the performance with fewer parameters. The structure is shown in Figure 3.

The merge AM mainly includes five steps: first, sum the output x_i of n PW convolutions to generate the fused data x_f. Second, compressed x_f by the global average pool operation to generate channel descriptor z_c, which can be expressed by Equation 6. Third, a special one-dimensional (1D) convolution is used to efficiently realize local cross-channel interaction and extract the dependencies between channels. In addition, a nonlinear activation (Sigmoid) function σ is included to learn the nonlinear relationship between channels, which can be expressed by Equation 7. Fourth, calculate the adaptive importance $a_i(s)$ for each input feature using the Softmax function, which can be expressed by Equation 8. Finally, refine the features of each PW convolution output according to the $a_i(s)$, and then the refined features x_o are fused by element-wise sum operation, which can be expressed by Equation 9.

$$z_c = \frac{1}{P \times P \times B} \sum_{i=1}^{P} \sum_{j=1}^{P} \sum_{k=1}^{B} x_f(i, j, k) \tag{6}$$

$$s = \sigma(W * z_c + b) \tag{7}$$

$$a_i(s) = \frac{\exp(s_i)}{\sum_{j=1}^{n} \exp(s_j)}, \; i = 1, \ldots, n \tag{8}$$

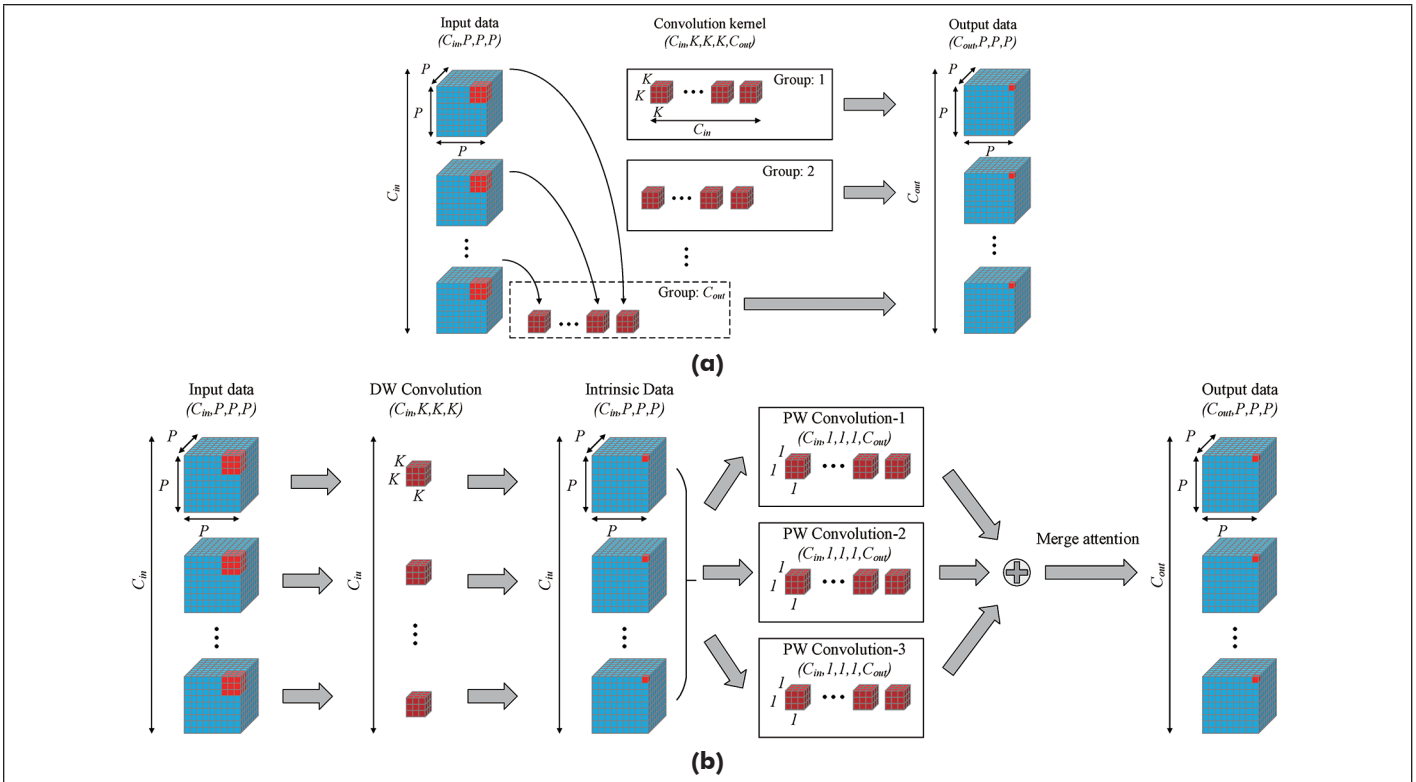

Figure 2. Graphical visualization of: (a) standard three-dimensional (3D) convolution and (b) depth-wise separable (DWS) conditional 3D convolution (assume that the padding size is $K/2$).

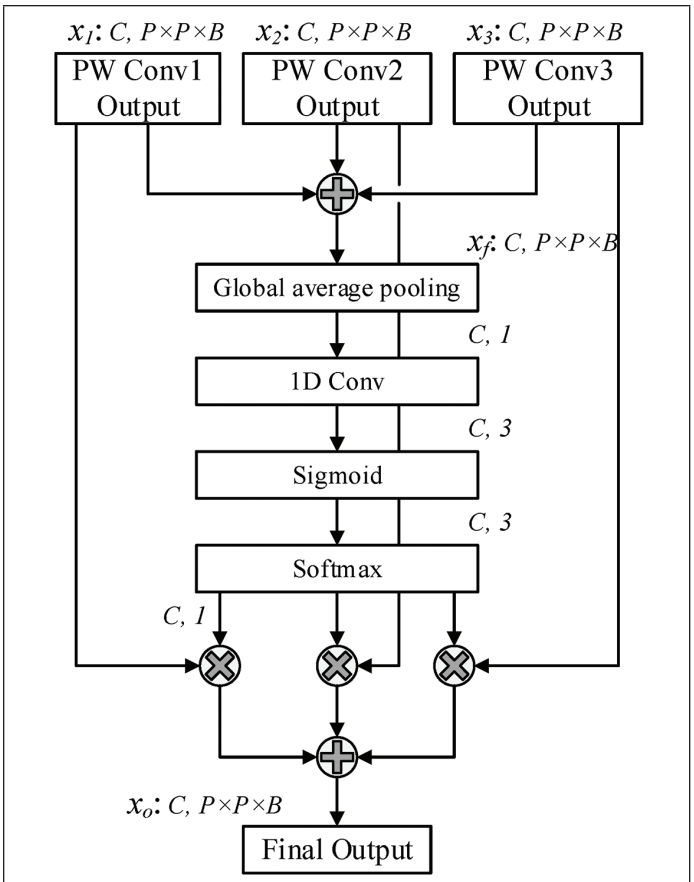

Figure 3. Structure of the proposed merge attention mechanism. 1D = one-dimensional; PW = point-wise.

$$x_o = \sum_{i=1}^{n} a_i(s) \times x_i \tag{9}$$

where B and P represent the spectral and spatial dimensions of the input data, and $x_f(i, j, k)$ represents the data value of the x_f at position (i, j, k). * is the convolution operation, and W and b are the bias and weights of convolution kernel, respectively.

The Framework of the Proposed Model for hsi Classification

Take the Indian Pines (IP) data set as an example, the framework of the proposed network is shown in Figure 4. First, a small cube is randomly selected from the HSI raw data as the input. Then, each small cube is fed into the dual branch network to extract the spatial and spectral features, respectively. Finally, the fused spectral and spatial features are input into a fully connected layer to generate the classification results.

The size of input data in spatial branch is (9×9×200). Before feed into the DWS conditional convolution unit, a standard convolution with the kernel size of (24, 1×1×200) and the stride size of (1×1×1) to reduce the spectral dimension, to generate the feature maps X_{11} of size (24, 9×9×1). Then, the feature maps X_{11} are feed into three DWS conditional convolution units to fully capture spatial features. To enhance the transmission of features and alleviate gradient vanishing problem, we apply dense connection, which connect each convolution layer to every other layer in a feedforward manner, and the out feature maps X_{12} with size of (60, 9×9×1) can be obtained. The size of the convolution kernel in each DWS conditional convolution is (12, 3×3×1), the stride size is (1×1×1), and the padding is (1×1×0). The implementation details of the spatial branch are reported in Table 1.

The size of input data in spectral branch is (9×9×200). Before feed into the DWS conditional convolution, a standard convolution with the kernel size of (24, 1×1×7) and the stride size of (1×1×2) to reduce the spectral dimension, to generate the feature maps X_{21} of size (24, 9×9×97). Then, the feature maps X_{21} are sent to three DWS conditional convolution units to fully capture spectral features, and the out feature maps X_{22} with size of (60, 9×9×97) can be obtained. The size of the convolution kernel in each DWS conditional convolution is (12, 1×1×7),

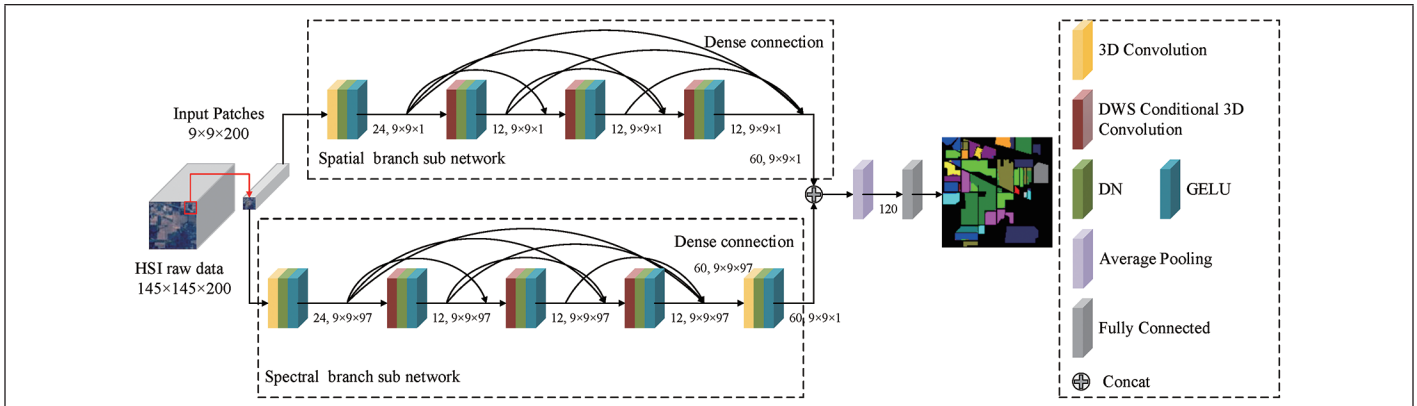

Figure 4. Flowchart of the proposed lightweight conditional convolutional network for hyperspectral image (HSI) classification. 3D = three-dimensional; DWS = depth-wise separable; DN = Data Normalization; GELU = Gaussian error linear units.

Table 1. The implementation details of the spatial branch.

Layer Name	Kernel Size	Stride Size	Output Size	DN	GELU
3D Conv	(24, 3×3×200)	(1×1×1)	(24, 9×9×1)	Yes	Yes
DWS Cond 3D Conv	(12, 3×3×1)	(1×1×1)	(24, 9×9×1)	Yes	Yes
DWS Cond 3D Conv	(12, 3×3×1)	(1×1×1)	(24, 9×9×1)	Yes	Yes
DWS Cond 3D Conv	(12, 3×3×1)	(1×1×1)	(24, 9×9×1)	Yes	Yes
Concatenation	—	—	(60, 9×9×1)	No	No

3D = three-dimensional; DWS = depth-wise separable; DN = Data Normalization; GELU = Gaussian error linear units.

Table 2. The implementation details of the spectral branch.

Layer Name	Kernel Size	Stride Size	Output Size	DN	GELU
3D Conv	(24, 1×1×7)	(1×1×2)	(24, 9×9×97)	Yes	Yes
DWS Cond 3D Conv	(12, 1×1×7)	(1×1×1)	(24, 9×9×97)	Yes	Yes
DWS Cond 3D Conv	(12, 1×1×7)	(1×1×1)	(24, 9×9×97)	Yes	Yes
DWS Cond 3D Conv	(12, 1×1×7)	(1×1×1)	(24, 9×9×97)	Yes	Yes
Concatenation	—	—	(60, 9×9×97)	No	No
3D Conv	(60, 1×1×97)	(1×1×1)	(60, 9×9×1)	Yes	Yes

3D = three-dimensional; DWS = depth-wise separable; DN = Data Normalization; GELU = Gaussian error linear units.

Table 3. The implementation details of the final prediction.

Layer Name	Kernel Size	Stride Size	Output Size	DN	GELU
Concatenation	—	—	(120, 9×9×1)	No	No
Global Average Pooling	(9×9×1)	(1×1×1)	(120, 1×1×1)	No	No
Flatten	—	—	(120)	No	No
Fully Connected	(120)	—	(16)	No	No

DN = Data Normalization; GELU = Gaussian error linear units.

the stride size is (1×1×1), the padding is (0×0×3). Finally, after the input feature maps X_{22} passes through the last layer, the out feature maps X_{23} with size of (60, 9×9×1) can be obtained. The last layer consists of a standard 3D convolution with size of (60, 1×1×97) and the stride size is (1×1×1). The implementation details of the spectral branch are reported in Table 2.

To obtain fused spatial and spectral features, we concatenate the feature maps X_{12} and X_{23} to generate the feature maps X_4 with size of (120, 9×9×1). Then, after the feature maps X_4 through the average pooling layer, the 1D vector X_5 with the dimension of 120 can be obtained. Finally, a fully connected layer to generate the probabilities of the 16 categories. The total loss for training our model is defined as follows:

$$L = -\frac{1}{S}\sum_{i=1}^{S}\left[y_i \log \hat{y}_i + (1-y_i)\log(1-\hat{y}_i)\right] \tag{10}$$

where S represents the number of samples in the mini-batch, y_i is the real labels, and $\hat{y}_i$ is the predicted labels of the model. The implementation details of the final prediction are reported in Table 3.

Experimental Results

Hyperspectral Data Sets

The experiment was conducted on three real HSI data sets used to evaluate HSI classification algorithms, including IP, Salinas Valley (SV), and Xu Zhou (XZ). The IP data set was collected by AM sensor over North Western India, containing 145 × 145 pixels and 200 bands, with a spatial resolution of 20 m per pixel. This scene has 10 249 labeled pixels and 16 different ground-truth classes, including one-third forest and two-thirds agriculture. Figure 5 shows the false color image and the corresponding ground truth image of the IP data set.

The SV data set was collected by AM sensor over Salinas Valley, California, containing 512 × 217 pixels and 204 bands, with a spatial resolution of 3.7 m per pixel. This scene has 54 129 labeled pixels and 16 different ground-truth classes, including vegetables, bare soils, and vineyard fields. Figure 6 shows the false color image and the corresponding ground truth image of the SV data set.

The XZ data set was collected by Hyperion sensor (HySpex SWIR-384, HySpex VNIR-1600) over Xu Zhou, China, containing 500 × 260 pixels and 436 bands. This scene has 68 877 labeled pixels and nine different ground-truth classes. Figure 7 shows the false color image and the corresponding ground truth image of the XZ data set.

Experimental Settings

In the experimental data sets, each class randomly selects five labeled samples as the training set, five labeled samples as the validation set, and the rest as the test set. For a fair comparison, all experiments are in the same experimental environment and hyperparameters. The number of training iterations is set to 300 and the batch size is set to 64. In addition, to prevent the model from falling into a local minimum, we the use cosine annealing (Konar *et al.* 2020) method to dynamically adjust the learning rate, and the initial value of the learning rate is set to 0.0005.

The hardware environment used in the experiment is an Intel Core i7-8750h CPU, NVIDIA Geforce GTX 1070 MAX-Q GPU, and 16 GB of memory. The software environment was CUDA 10.2, Python 3.6.8, and PyTorch 1.6.

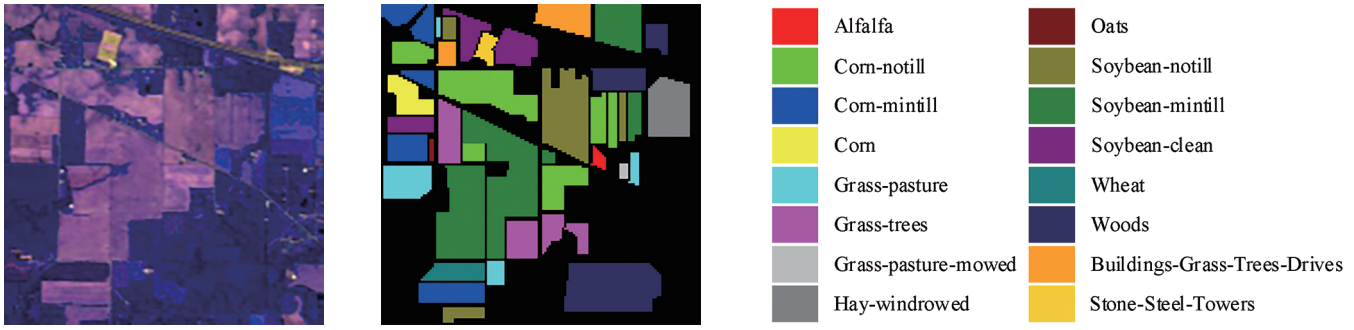

Figure 5. Indian Pines (IP) data set: (a) false color image (R = 28, G = 8, B = 99), (b) ground truth map, (c) land-cover classes. RGB = red, green, blue.

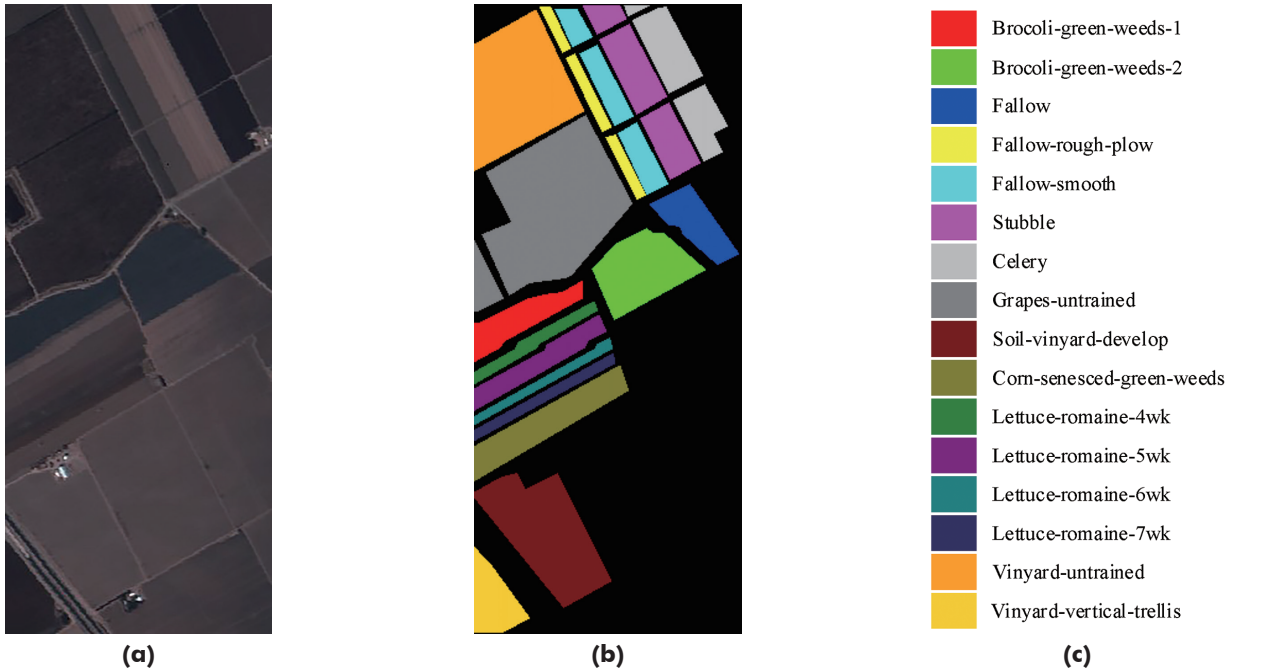

Figure 6. Salinas Valley (SV) data set: (a) false color image (R = 23, G = 11, B = 7), (b) ground truth map, (c) land-cover classes. RGB = red, green, blue.

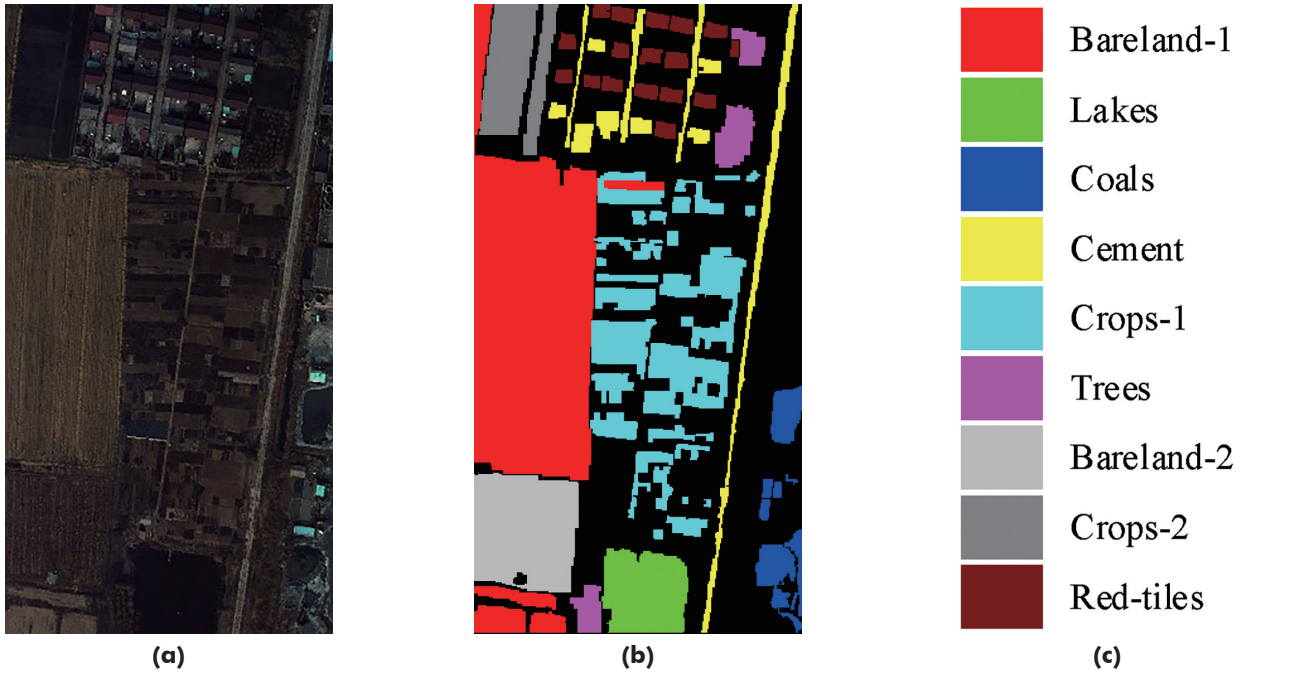

Figure 7. Xu Zhou (XZ) data set: (a) false color image (R = 38, G = 56, B = 23), (b) ground truth map, (c) land-cover classes. RGB = red, green, blue.

Comparison with Different Methods

To illustrate the advantage of the proposed model for hyperspectral image classification, this section compares the proposed model with the classical machine learning method SVM (Tarabalka *et al.* 2010) and several recently proposed deep learning methods, contextual deep convolutional neural network (CDCNN) (Lee and Kwon 2017), SSRN (Zhong *et al.* 2018), lightweight multi-attention fusion network (LMAFN) (Wang *et al.* 2021), SpectralFormer (Hong *et al.* 2021), spectral-spatial multilayer perceptrons (SS-MLP) (Meng *et al.* 2021). The CDCNN is a typical deep network, mainly composed of 11 2D convolution layers and one fully connected layer. The SSRN uses 3D convolution with the residual structure to exploit the joint spatial-spectral information. The LMAFN is a lightweight 2D CNN to achieve accurate classification under small training samples. The SpectralFormer (SF) is a VIT-based model that converts images into sequences to capture long-term dependency information from HSI. The SS-MLP is a new multi-layer perceptron architecture for HSI classification. The experiment was repeated 10 times, and the cube size of HSI was $9\times9\times B$, where B represents the number of bands in the HSI data set. The quantitative experimental results of different methods are shown in Tables 4–6, and the best results for each class are highlighted in boldface. The metrics include overall accuracy (OA), average accuracy (AA), and Kappa coefficient were used to evaluate the classification accuracy. In addition, the model size (Size), the number of parameters (NOP), FLOPS, training time (Train (s)), and test time (Test (s)) are used to evaluate the complexity and execution efficiency of the model.

From Tables 4–6, the following conclusions can be drawn:

(1) The results of HSI classification based on the deep learning method is better than the traditional classification method. Traditional classification methods use handcrafted features. When dealing with complex samples, these methods quickly fall into a bottleneck. However, the classification methods based on deep learning can automatically learn the abstract features of images through the hierarchical structure, so they have stronger feature extraction ability than the traditional classification methods.

(2) Although SF and SS-MLP perform well on large-scale data sets, too many parameters become a burden, leading to serious overfitting problems in HSI data sets with very limited labeled samples. Therefore, their performance is significantly worse than CNN based model in the experiment. In addition, the high computational burden and memory consumption bring challenges for deployment to mobile systems.

(3) Among all CNN classification methods, CDCNN has the worst performance. Compared with SSRN on the IP data set, the values of OA, AA, and Kappa drop by –9.76%, –8.36%, and –11.17%, respectively. In addition, although LMAFN adopts a lightweight design, compared with our network on the IP data set, the OA, AA, and Kappa values decreased by 5.41%, 6.28%, and 6.20%, respectively. The reason is that the pure 2D CNN cannot jointly extract spectral and spatial features in HSI, and the deep network structure also leads to the degradation of the model.

(4) On three real HSI data sets, the proposed method achieved the highest OA, AA, and Kappa values. On the one hand, the two-branch shallow network architecture and dense connection structure enhance the transmission and reuse of features, to overcome the gradient vanishing and model degradation. On the other hand, DWS conditional 3D convolution can effectively improve the representation ability of the model, and the merge attention mechanism can adaptively focus on important

Table 4. Classification results on the Indian Pines (IP) data set (five labeled samples per class).

Color	Train	SVM	CDCNN	SSRN	LMAFN	SF	SS-MLP	Proposed
■	5	29.30	32.26	38.68	91.62	57.97	37.27	**93.18**
■	5	44. 09	29.77	43.64	79.65	62.98	**85.42**	81.11
■	5	44.51	40.17	59.06	69.42	**74.15**	52.28	55.14
■	5	16.75	52.44	35.64	59.07	29.17	44.04	**80.71**
■	5	35.35	71	72.87	98.73	74.15	54.47	**99.46**
■	5	83.66	78.49	93.58	95.00	90.79	77.74	**96.43**
■	5	21.57	12.64	26.14	16.55	12.23	**53.66**	28.95
■	5	91.92	93.69	99.76	**100**	**100**	89.94	**100**
■	5	15.06	22.39	15.46	23.73	**25.00**	10.49	21.21
■	5	44.16	63.06	**82.75**	65.50	55.68	60.94	66.55
■	5	59.40	69.89	74.95	67.89	62.98	**76.83**	69.84
■	5	24.86	23.01	36.54	29.58	60.33	24.42	**83.10**
■	5	80.70	73.83	**90.57**	80.49	69.50	61.80	87.50
■	5	77.69	86.11	96.87	92.27	94.86	83.79	**98.33**
■	5	39.81	66.43	76.50	88.31	75.86	64.29	**94.63**
■	5	**98.67**	55.70	61.60	65.19	33.72	38.91	75.44
OA		50.62	58.51	68.27	73.93	66.97	65.56	**79.34**
AA		50.47	54.43	62.79	70.70	61.21	57.27	**76.98**
Kappa		44.52	53.20	64.37	70.30	62.37	61.29	**76.50**
Size (KB)		-	4,170	1,451	766	27,906	52,943	**195**
NOP (K)		-	1,064	310	161	7,129	13,546	**41**
FLOPs (M)		-	29.57	158.00	7.37	582.72	123.91	**6.21**
Train (s)		1.92	31.84	189.25	49.72	437.35	132.55	**45.60**
Test (s)		0.94	1.04	4.18	3.85	17.02	11.71	**3.49**

SVM = support vector machine; CDCNN = contextual deep convolutional neural network; SSRN = spectral-spatial residual network; LMAFN = lightweight multi-attention fusion network; SF = SpectralFormer; SS-MLP = spectral-spatial multilayer perceptrons; OA = overall accuracy; AA = average accuracy; NOP = number of parameters; FLOPs = floating-point operations per second.

Table 5. Classification results on Salinas Valley (SV) data set (five labeled samples per class).

Color	Train	SVM	CDCNN	SSRN	LMAFN	SF	SS-MLP	Proposed
■	5	96.03	89.69	58.65	99.85	98.98	99.75	**100**
■	5	98.55	98.30	99.87	99.47	95.99	99.22	**100**
■	5	77.12	93.92	91.65	93.36	89.18	94.97	**95.22**
■	5	97.38	92.31	**99.00**	85.73	76.00	88.07	93.64
■	5	88.14	94.32	99.80	99.53	85.88	90.28	**99.84**
■	5	99.85	99.85	**100**	99.62	99.90	99.77	99.77
■	5	97.77	97.87	**100**	**100**	99.62	98.78	**100**
■	5	69.98	83.80	85.20	**92.28**	83.86	84.67	88.28
■	5	*99.50*	96.23	99.29	96.91	99.11	99.16	98.55
■	5	76.99	81.78	91.59	90.86	80.24	93.29	**96.76**
■	5	75.97	86.12	**95.03**	85.38	70.53	76.03	94.40
■	5	97.63	98.24	93.74	**99.69**	88.91	99.58	99.12
■	5	54.52	88.29	91.44	96.84	98.71	97.09	**99.56**
■	5	69.12	91.47	**100**	95.52	98.02	90.20	97.79
■	5	64.90	**85.63**	64.60	75.91	65.14	66.05	75.17
■	5	85.95	60.49	97.47	**100**	97.97	97.31	**100**
OA		83.07	89.40	87.19	90.50	86.83	89.20	**93.11**
AA		84.43	89.89	91.71	93.47	89.33	92.13	**96.13**
Kappa		81.14	88.26	85.80	90.89	85.40	88.02	**92.34**
Size (KB)		-	4,240	1,475	770	27,908	53,015	**195**
NOP (K)		-	1,064	310	162	7,129	13,564	**41**
FLOPs (M)		-	29.57	161.21	7.38	582.76	124.08	**6.34**
Train (s)		2.28	34.56	219.72	64.83	492.35	150.01	**58.27**
Test (s)		5.33	5.68	23.40	22.52	82.54	57.43	**19.95**

SVM = support vector machine; CDCNN = contextual deep convolutional neural network; SSRN = spectral-spatial residual network; LMAFN = lightweight multi-attention fusion network; SF = SpectralFormer; SS-MLP = spectral-spatial multilayer perceptrons; OA = overall accuracy; AA = average accuracy; NOP = number of parameters; FLOPs = floating-point operations per second.

Table 6. Classification results on Xu Zhou (XZ) data set (five labeled samples per class).

Color	Train	SVM	CDCNN	SSRN	LMAFN	SF	SS-MLP	Proposed
■	5	78.69	99.42	96.09	97.49	96.95	98.47	**99.92**
■	5	99.11	76.45	100	96.52	89.38	95.01	**100**
■	5	67.36	84.56	48.41	91.78	91.43	85.30	**98.14**
■	5	97.65	74.04	**99.55**	90.09	92.27	86.46	95.39
■	5	59.82	94.20	**97.95**	89.33	93.15	92.60	93.23
■	5	26.17	64.74	66.94	**96.55**	41.93	85.20	79.00
■	5	21.43	69.57	73.31	82.73	**92.83**	78.38	76.83
■	5	95.08	83.84	93.68	93.21	96.39	96.41	**97.86**
■	5	63.72	**88.65**	84.19	84.89	77.60	68.34	82.30
OA		77.00	86.82	87.93	92.55	88.85	90.86	**94.93**
AA		73.34	81.72	84.50	91.73	86.10	87.35	**94.13**
Kappa		71.70	83.60	84.81	90.59	87.17	88.52	**93.63**
Size (KB)		-	8,296	2,866	1,249	28,020	57,177	**247**
NOP (K)		-	2,120	726	346	7,158	14,630	**53**
FLOPs (M)		-	64.21	347.05	15.78	585.17	133.69	**13.67**
Train (s)		2.86	39.62	259.20	76.10	525.30	163.58	**69.16**
Test (s)		6.51	18.75	62.09	60.57	93.74	65.08	**57.40**

SVM = support vector machine; CDCNN = contextual deep convolutional neural network; SSRN = spectral-spatial residual network; LMAFN = lightweight multi-attention fusion network; SF = SpectralFormer; SS-MLP = spectral-spatial multilayer perceptrons; OA = overall accuracy; AA = average accuracy; NOP = number of parameters; FLOPs = floating-point operations per second.

information that is conducive to classification. Therefore, the proposed method avoids the knowledge degradation caused by blindly reducing parameters and enhances the performance of classification. Compared with other deep learning models, our model has the lowest memory consumption, number of parameters, and computational complexity, so it is friendly to embedded systems.

The visual comparison of classification maps of seven methods is shown in Figures 8–10. As we expected, the classification maps predicted by SVM on the three data sets contain the most noise because the traditional methods are difficult to extract more discriminant features. Focusing on the IP data set, the high similarity and significant class imbalance between classes bring challenges to classification. Nevertheless, compared with other comparison methods, the classification maps generated by the proposed method have the least noise and are most consistent with the ground-truth map. For SV and XZ data sets, the classification results have been significantly improved compared with the IP data set due to sufficient samples of each category and more regular land cover. These results further prove that, compared with other classification methods, our method can achieve more satisfactory results even in the case of small training samples. In addition, it has fewer parameters, lower computational complexity, and less memory consumption.

Discussion

In this section, we investigate the proposed method in three aspects: First, an ablation study verifies the effectiveness of the merge attention mechanism, the dense connection structure, and the conditional convolution. Second, we evaluate the impact of different numbers of convolution kernels in DW convolution on classification performance. Third, we evaluate the classification performance of different methods in the different numbers of training samples.

Ablation Study

We conduct an ablation study by removing different components to understand the contribution of different components in the proposed model.

Effectiveness analysis of the merge attention mechanism: In the proposed model, the merge attention mechanism can adaptively focus on sensitive locations and spectral information that is conducive to classification and boost the performance of the model. To evaluate the effectiveness of the proposed attention mechanism, we remove it and check how the OA, AA, and Kappa change. Specifically, we remove the merge attention mechanism from each DWS conditional convolution unit. In DWS conditional convolution, the output features of multiple convolution kernels are no longer enhanced by the merge attention mechanism, but directly perform the element-wise sum operation as the final output. As can be seen from Table 7, the OA, AA, and Kappa of the model with the merge attention mechanism are higher than those of the model without the merge attention mechanism on the three data sets. This experiment proves the advantages of the merge attention mechanism.

Effectiveness analysis of the dense connection structure: to optimize the transmission and reuse of features, the proposed two-branch model adopts a dense connection structure. Therefore, we compare the performance by removing dense connections from the model to prove the effectiveness of the structure. As can be seen from Table 8, when the dense connection is removed, the OA, AA, and Kappa of the model are reduced. It can be concluded that dense connections can improve classification performance.

Effectiveness analysis of the conditional convolution: we further evaluate the effectiveness of the conditional convolution to improve the performance of the model. The benchmark model is the whole model proposed, while the comparison model is the version after removing the conditional convolution from the benchmark model. Therefore, the comparison model can be regarded as a pure DWS 3D convolution model. The experiment was conducted on IP, SV, and XZ data sets. In addition, five samples are selected for each class in the data set to train the model, and the remaining samples are used for testing the model. Table 9 reports the classification results of the experiment. It can be observed that the simple use of pure DWS 3D convolution reduces the parameters of the model but leads to obvious model degradation. Therefore, on the HSI data set lacking training samples, the classification performance has been significantly affected. In addition, compared with the pure DSW convolution model, conditional convolution significantly improves the performance of the model.

Table 7. Ablation study of the merge attention mechanism on the three data sets.

Data Set	Merge AM	OA	AA	Kappa
IP	√	79.34	76.98	76.50
	—	77.87	75.46	75.61
SV	√	93.11	96.13	92.34
	—	91.75	94.82	91.05
XZ	√	94.93	94.13	93.63
	—	92.67	91.88	91.85

AM = attention mechanism; OA = overall accuracy; AA = average accuracy; IP = Indian Pines; SV = Salinas Valley; XZ = Xu Zhou.

Table 8. Ablation study of the dense connection on the three data sets.

Data Set	Dense Connection	OA	AA	Kappa
IP	√	79.34	76.98	76.50
	—	78.27	75.70	75.35
SV	√	93.11	96.13	92.34
	—	92.32	94.88	91.40
XZ	√	94.93	94.13	93.63
	—	93.83	93.22	92.76

OA = overall accuracy; AA = average accuracy; IP = Indian Pines; SV = Salinas Valley; XZ = Xu Zhou.

Table 9. Ablation study of the conditional convolution on the three data sets.

Data Set	Conditional Convolution	OA	AA	Kappa
IP	√	79.34	76.98	76.50
	—	77.16	74.88	74.69
SV	√	93.11	96.13	92.34
	—	91.27	94.36	90.52
XZ	√	94.93	94.13	93.63
	—	92.22	91.30	91.29

OA = overall accuracy; AA = average accuracy; IP = Indian Pines; SV = Salinas Valley; XZ = Xu Zhou.

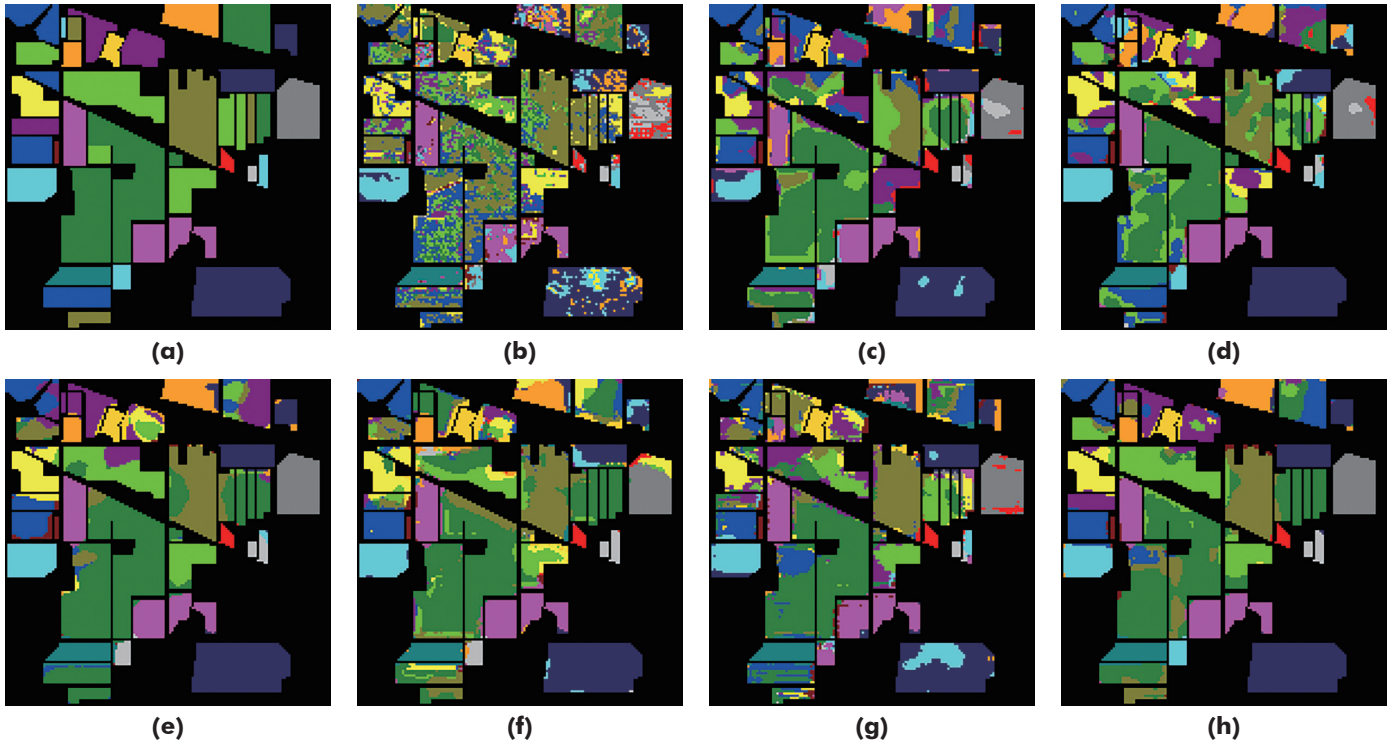

Figure 8. Classification maps on the Indian Pines (IP) data set: (a) ground-truth, (b) support vector machine (SVM), (c) contextual deep convolutional neural network (CDCNN), (d) spectral-spatial residual network (SSRN), (e) lightweight multi-attention fusion network (LMAFN), (f) SpectralFormer (SF), (g) spectral-spatial multilayer perceptrons (SS-MLP), and (h) Proposed.

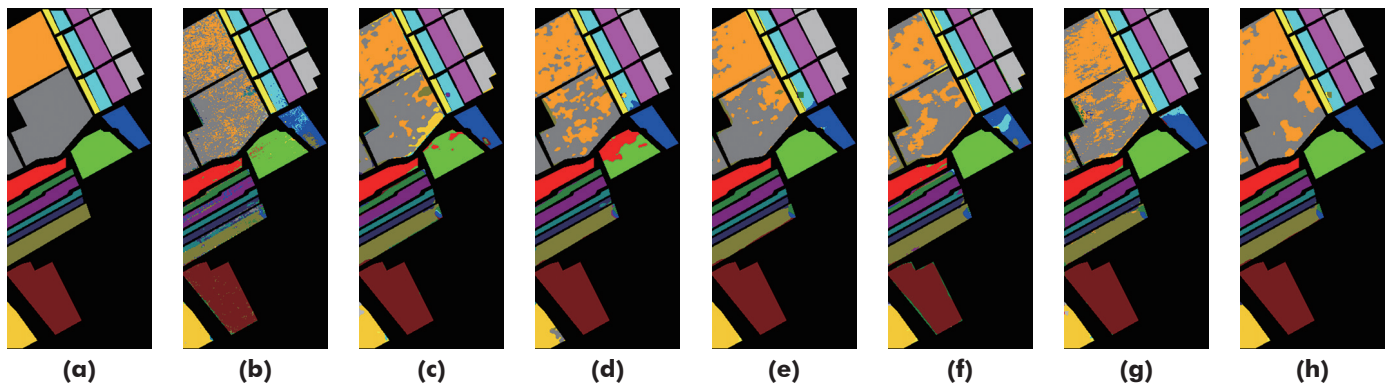

Figure 9. Classification maps on the Salinas Valley (SV) data set: (a) ground-truth, (b) support vector machine (SVM), (c) contextual deep convolutional neural network (CDCNN), (d) spectral-spatial residual network (SSRN), (e) lightweight multi-attention fusion network (LMAFN), (f) vision transformers (VIT), (g) spectral-spatial multilayer perceptrons (SS-MLP), and (h) Proposed.

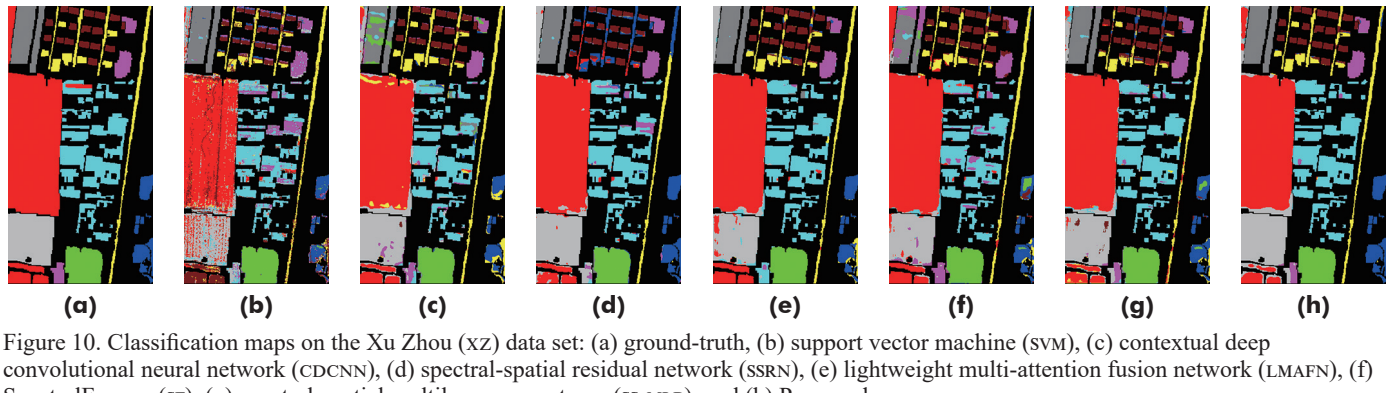

Figure 10. Classification maps on the Xu Zhou (XZ) data set: (a) ground-truth, (b) support vector machine (SVM), (c) contextual deep convolutional neural network (CDCNN), (d) spectral-spatial residual network (SSRN), (e) lightweight multi-attention fusion network (LMAFN), (f) SpectralFormer (SF), (g) spectral-spatial multilayer perceptrons (SS-MLP), and (h) Proposed.

Investigation of the Number of Convolution Kernels

In this paper, DWS conditional convolution is used to replace the standard convolution to improve the spatial and spectral feature extraction ability of the model. Therefore, this section discusses the impact of the number of convolution kernels used in DWS conditional convolution on classification accuracy. Specifically, 1, 2, 4, 8, and 16 convolution kernels are set for experiments. Figure 11 shows the OA values of the different numbers of convolution kernels on IP, SV, and XZ data sets. Each class randomly selects five labeled samples as the training set, five labeled samples as the validation set, and the rest as the test set. In addition, Table 10 reports the number of parameters of different numbers of convolution kernels on the three data sets. In general, the more convolution kernels used in DWS conditional convolution, the higher the OA value can be obtained. However, with limited training samples, the increase of OA value slows down when the number of convolution kernels reaches 4. To obtain the best performance and efficiency, the number of convolution kernels used in DWS conditional convolution is 4.

Investigation of the Number of Training Samples

Because deep learning is a data-driven algorithm, to explore the sensitivity of the model to the number of training samples, we used different numbers of training samples to conduct experiments on IP, SV, and XZ data sets. Specifically, in each category, 5, 10, and 15 samples are chosen to train the model. Figure 12 shows the impact of different numbers of training samples on classification results in three data sets. In our expectation, more training samples can significantly improve the classification accuracy of the model. In addition, compared with SVM, the classification method based on deep learning can get more benefits from increasing training samples. Our method has strong robustness and can get satisfactory results under a different number of training samples.

Table 10. The number of parameters of depth-wise separable (DWS) conditional convolution when using different numbers of convolution kernels.

Data Set	1	2	4	8	16
IP	21 906	28 244	40 920	66 272	116 976
SV	22 122	28 460	41 136	66 488	117 192
XZ	33 838	40 239	53 125	79 233	132 793

IP = Indian Pines; SV = Salinas Valley; XZ = Xu Zhou.

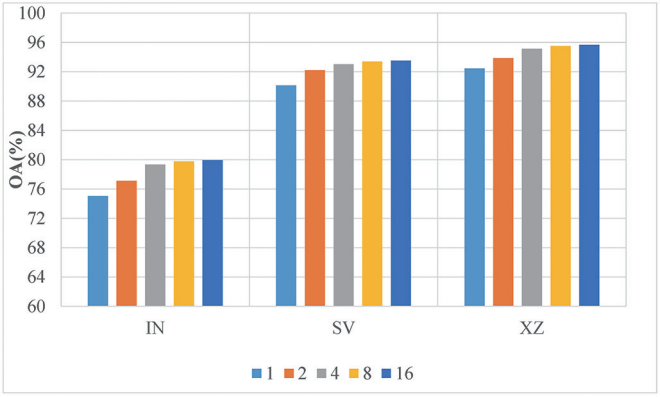

Figure 11. Overall Accuracy (OA) of depth-wise separable (DWS) conditional convolution when using different numbers of convolution kernels.

Conclusions

Recently, in mobile and embedded systems, real-time HSI classification methods must show good performance in terms of classification accuracy, training set size, model efficiency, and memory consumption. To this end, we build a new extremely lightweight and computational efficiency 3D CNN for HSI classification. Specifically, the proposed model adopts a shallow dual branch and dense connection structure to effectively overcome the model degradation caused by the deep network. Meanwhile, the DWS conditional convolution module is carefully designed to ensure the discriminative ability of the extracted features without too many parameters and computational burdens. Furthermore, the merge attention mechanism can adaptively focus on important information that is conducive to classification, thus further improving the performance of the model. We conducted experiments on three benchmark HSI data sets. The experimental results show that our model achieves higher execution speed and better classification performance compared with several state-of-the-art HSI classification models, highlighting the effectiveness of the proposed model in reducing computing and memory costs.

References

Abdel-Rahman, E. M., F. B. Ahmed and R. Ismail. 2013. Random forest regression and spectral band selection for estimating sugarcane leaf nitrogen concentration using EO-1 Hyperion hyperspectral data. *International Journal of Remote Sensing* 34(2):712–728.

Ahmad, M., S. Shabbir, S. K. Roy, D. Hong, X. Wu, J. Yao, A. M. Khan, M. Mazzara, S. Distefano and J. Chanussot. 2022. Hyperspectral image classification-traditional to deep models: A survey for future prospects. *IEEE Journal of Selected Topics in Applied Earth Observations and Remote Sensing* 15:968–999.

Bordes, A., X. Glorot, J. Weston and Y. Bengio. 2012. Joint learning of words and meaning representations for open-text semantic parsing. Pages 127–135 in *Proceedings of the Fifteenth International Conference on Artificial Intelligence and Statistics Vol. 22*, held in La Palma, Canary Islands, 21–23 April 2012.

Chen, Y., Z. Lin, X. Zhao, G. Wang and Y. Gu. 2014. Deep learning-based classification of hyperspectral data. *IEEE Journal of Selected Topics in Applied Earth Observations and Remote Sensing* 7(6):2094–2107.

Choudhary, T., V. Mishra, A. Goswami and J. Sarangapani. 2020. A comprehensive survey on model compression and acceleration. *Artificial Intelligence Review* 53(7):5113–5155.

Deng, L., G. Li, S. Han, L. Shi and Y. Xie. 2020. Model compression and hardware acceleration for neural networks: A comprehensive survey. *Proceedings of the IEEE* 108(4):485–532.

Fu, J., J. Liu, H. Tian, Y. Li, Y. Bao, Z. Fang and H. Lu. 2019. Dual attention network for scene segmentation. Pages 3146–3154 in *Proceedings of the IEEE/CVF Conference on Computer Vision and Pattern Recognition*, held in Long Beach, Calif., 16–20 June 2019.

Girshick, R., J. Donahue, T. Darrell and J. Malik. 2014. Rich feature hierarchies for accurate object detection and semantic segmentation. Pages 580–587 in *Proceedings 2014 IEEE Conference on Computer Vision and Pattern Recognition*, Columbus, Ohio, 23–28 June 2014.

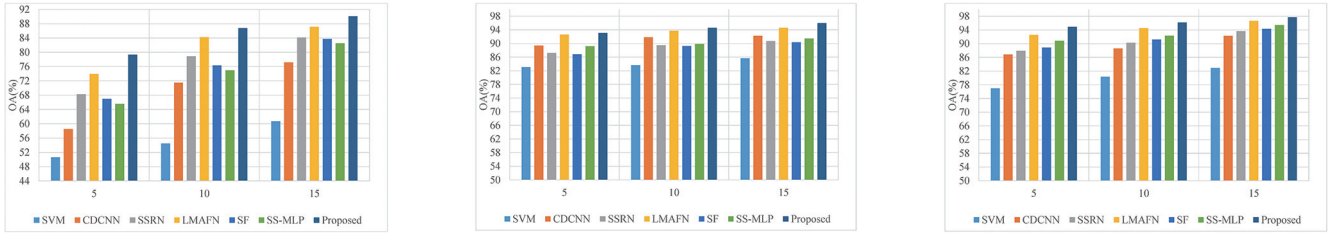

Figure 12. Overall Accuracy (OA) of different models when using different numbers of training samples on three data sets: (a) IP, (b) SV, and (c) XZ. IP = Indian Pines; SV = Salinas Valley; XZ = Xu Zhou.

Han, K., Y. Wang, Q. Tian, J. Guo, C. Xu and C. Xu. 2020. GhostNet: More features from cheap operations. Pages 1577–1586 in *Proceedings 2020 IEEE/CVF Conference on Computer Vision and Pattern Recognition (CVPR)*, held in Seattle, Wash., 13–19 June 2020.

He, L., J. Li, C. Liu and S. Li. 2018. Recent advances on spectral–spatial hyperspectral image classification: An overview and new guidelines. *IEEE Transactions on Geoscience and Remote Sensing* 56(3):1579–1597.

Hendrycks, D. and K. Gimpel. 2016. Gaussian error linear units (GELUS). *arXiv preprint*: arXiv:1606.08415. https://doi.org/10.48550/arXiv.1606.08415

Hong, D., Z. Han, J. Yao, L. Gao, B. Zhang, A. Plaza and J. Chanussot. 2021. SpectralFormer: Rethinking hyperspectral image classification with transformers. *IEEE Transactions on Geoscience and Remote Sensing* 60:1–15.

Huang, G., S. Liu, L.V.D. Maaten and K. Q. Weinberger. 2018. CondenseNet: An efficient DenseNet using learned group convolutions. Pages 2752–2761 in *Proceedings 2018 IEEE/CVF Conference on Computer Vision and Pattern Recognition*, held in Salt Lake City, Utah, 18–22 June 2018.

Huang, G., Z. Liu, L.V.D. Maaten and K. Q. Weinberger. 2017. Densely connected convolutional networks. Pages 2261–2269 in *Proceedings 2017 IEEE Conference on Computer Vision and Pattern Recognition (CVPR)*, held in Honolulu, Hawaii, 21–26 July 2017.

Huang, Z., X. Wang, L. Huang, C. Huang, Y. Wei and W. Liu. 2019. Ccnet: Criss-cross attention for semantic segmentation. Pages 603–612 in *Proceedings of the IEEE/CVF International Conference on Computer Vision*, held in Seoul, Korea, 27 October–2 November 2019.

Ioffe, S. and C. Szegedy. 2015. Batch normalization: Accelerating deep network training by reducing internal covariate shift. Pages 448–456 in *Proceedings International Conference on Machine Learning*, held in Lille, France, 6–11 July 2015.

Jain, R. and R. U. Sharma. 2019. Airborne hyperspectral data for mineral mapping in Southeastern Rajasthan, India. *International Journal of Applied Earth Observation and Geoinformation* 81:137–145.

Jia, S., Z. Lin, M. Xu, Q. Huang, J. Zhou, X. Jia and Q. Li. 2021. A lightweight convolutional neural network for hyperspectral image classification. *IEEE Transactions on Geoscience and Remote Sensing* 59(5):4150–4163.

Konar, J., P. Khandelwal and R. Tripathi. 2020. Comparison of various learning rate scheduling techniques on convolutional neural network. Pages 1–5 in *Proceedings 2020 IEEE International Students' Conference on Electrical, Electronics and Computer Science (SCEECS)*, held in Bhopal, India, 22–23 February 2020.

Krizhevsky, A., I. Sutskever and G. E. Hinton. 2012. Imagenet classification with deep convolutional neural networks. *Advances in Neural Information Processing Systems* 25.

Lee, H. and H. Kwon. 2017. Going deeper with contextual CNN for hyperspectral image classification. *IEEE Transactions on Image Processing* 26(10):4843–4855.

Li, R., S. Zheng, C. Duan, Y. Yang and X. Wang. 2020. Classification of hyperspectral image based on double-branch dual-attention mechanism network. *Remote Sensing* 12(3):582.

Li, T., J. Zhang and Y. Zhang. 2014. Classification of hyperspectral image based on deep belief networks. Pages 5132–5136 in *Proceedings 2014 IEEE International Conference on Image Processing (ICIP)*, held in Paris, France, 27–30 October 2014 .

Liang, L., L. Di, L. Zhang, M. Deng, Z. Qin, S. Zhao and H. Lin. 2015. Estimation of crop LAI using hyperspectral vegetation indices and a hybrid inversion method. *Remote Sensing of Environment* 165:123–134.

Liu, C., C. Xing, Q. Hu, S. Wang, S. Zhao and M. Gao. 2022. Stereoscopic hyperspectral remote sensing of the atmospheric environment: Innovation and prospects. *Earth-Science Reviews* 226:103958.

Liu, Y., Y. Sun, B. Xue, M. Zhang, G. G. Yen and K. C. Tan. 2021. A survey on evolutionary neural architecture search. *IEEE Transactions on Neural Networks and Learning Systems* 1–21.

Ma, L., M. M. Crawford and J. Tian. 2010. Local manifold learning-based k-nearest-neighbor for hyperspectral image classification. *IEEE Transactions on Geoscience and Remote Sensing* 48(11):4099–4109.

Ma, N., X. Zhang, H.-T. Zheng and J. Sun. 2018. ShuffleNet V2: Practical guidelines for efficient CNN architecture design. Pages 122–138 in *Proceedings Computer Vision–ECCV 2018*, held in Munich, Germany, 8–14 September 2018.

Meng, Z., F. Zhao and M. Liang. 2021. SS-MLP: A novel spectral-spatial MLP architecture for hyperspectral image classification. *Remote Sensing* 13(20):4060.

Paoletti, M. E., J. M. Haut, N. S. Pereira, J. Plaza and A. Plaza. 2021. Ghostnet for hyperspectral image classification. *IEEE Transactions on Geoscience and Remote Sensing* 59(12):10378–10393.

Paoletti, M. E., J. M. Haut, J. Plaza and A. Plaza. 2020. Scalable recurrent neural network for hyperspectral image classification. *The Journal of Supercomputing* 76(11):8866–8882.

Peyghambari, S. and Y. Zhang. 2021. Hyperspectral remote sensing in lithological mapping, mineral exploration, and environmental geology: An updated review. *Journal of Applied Remote Sensing* 15(3):031501.

Quesada-Barriuso, P., F. Argüello and D. B. Heras. 2014. Spectral–spatial classification of hyperspectral images using wavelets and extended morphological profiles. *IEEE Journal of Selected Topics in Applied Earth Observations and Remote Sensing* 7(4):1177–1185.

Sandler, M., A. Howard, M. Zhu, A. Zhmoginov and L. C. Chen. 2018. MobileNetV2: Inverted residuals and linear bottlenecks. Pages 4510–4520 in *Proceedings 2018 IEEE/CVF Conference on Computer Vision and Pattern Recognition*, held in Salt Lake City, Utah, 18–22 June 2018.

Serranti, S., R. Palmieri, G. Bonifazi and A. Cózar. 2018. Characterization of microplastic litter from oceans by an innovative approach based on hyperspectral imaging. *Waste Management* 76:117–125.

Sikakollu, P. and R. Dash. 2021. Ensemble of multiple CNN classifiers for HSI classification with Superpixel Smoothing. *Computers & Geosciences* 154:104806.

Tarabalka, Y., M. Fauvel, J. Chanussot and J. A. Benediktsson. 2010. SVM- and MRF-based method for accurate classification of hyperspectral images. *IEEE Geoscience and Remote Sensing Letters* 7(4):736–740.

Vaswani, A., N. Shazeer, N. Parmar, J. Uszkoreit, L. Jones, A. N. Gomez, Ł. Kaiser and I. Polosukhin. 2017. Attention is all you need. *Advances in Neural Information Processing Systems* 30.

Wang, J., R. Huang, S. Guo, L. Li, Z. Pei and B. Liu. 2022. HyperLiteNet: Extremely lightweight non-deep parallel network for hyperspectral image classification. *Remote Sensing* 14(4).

Wang, J., R. Huang, S. Guo, L. Li, M. Zhu, S. Yang and L. Jiao. 2021. NAS-guided lightweight multiscale attention fusion network for hyperspectral image classification. *IEEE Transactions on Geoscience and Remote Sensing* 59(10):8754–8767.

Wang, J., L. Jiao, H. Liu, S. Yang and F. Liu. 2015. Hyperspectral image classification by spatial–spectral derivative-aided kernel joint sparse representation. *IEEE Journal of Selected Topics in Applied Earth Observations and Remote Sensing* 8(6):2485–2500.

Wang, W., Y. Li, T. Zou, X. Wang, J. You and Y. Luo. 2020. A novel image classification approach via dense-MobileNet models. *Mobile Information Systems* 2020:7602384.

Wu, B., X. Dai, P. Zhang, Y. Wang, F. Sun, Y. Wu, Y. Tian, P. Vajda, Y. Jia and K. Keutzer. 2019. FBNet: Hardware-aware efficient ConvNet design via differentiable neural architecture search. Pages in 10726–10734 in *Proceedings 2019 IEEE/CVF Conference on Computer Vision and Pattern Recognition (CVPR)*, held in Long Beach, Calif., 16–20 June 2019.

Yang, B., G. Bender, Q. V. Le and J. Ngiam. 2019. Condconv: Conditionally parameterized convolutions for efficient inference. *Advances in Neural Information Processing Systems* 32.

Zhan, Y., D. Hu, Y. Wang and X. Yu. 2018. Semisupervised hyperspectral image classification based on generative adversarial networks. *IEEE Geoscience and Remote Sensing Letters* 15(2):212–216.

Zhang, H., Y. Li, Y. Jiang, P. Wang, Q. Shen and C. Shen. 2019. Hyperspectral classification based on lightweight 3-D-CNN with transfer learning. *IEEE Transactions on Geoscience and Remote Sensing* 57(8):5813–5828.

Zhang, X., X. Zhou, M. Lin and J. Sun. 2018. ShuffleNet: An extremely efficient convolutional neural network for mobile devices. Pages 6848–6856 in *Proceedings 2018 IEEE/CVF Conference on Computer Vision and Pattern Recognition*, held in Salt Lake City, Utah, 18–22 June 2018.

Zhong, Z., J. Li, D. A. Clausi and A. Wong. 2020. Generative adversarial networks and conditional random fields for hyperspectral image classification. *IEEE Transactions on Cybernetics* 50(7):3318–3329.

Zhong, Z., J. Li, Z. Luo and M. Chapman. 2018. Spectral–spatial residual network for hyperspectral image classification: A 3-D deep learning framework. *IEEE Transactions on Geoscience and Remote Sensing* 56(2):847–858.

Zhou, Y., J. Peng and C.L.P. Chen. 2015. Extreme learning machine with composite kernels for hyperspectral image classification. *IEEE Journal of Selected Topics in Applied Earth Observations and Remote Sensing* 8(6):2351–2360.

Call for *PE&RS* Special Issue Submissions

Ushering a New Era of Hyperspectral Remote Sensing to Advance Remote Sensing Science in the Twenty-first Century

Great advances are taking place in remote sensing with the advent of new generation of hyperspectral sensors. These include data from, already in orbit sensors such as: 1. Germany's Deutsches Zentrum fur Luftund Raumfahrt (DLR's) Earth Sensing Imaging Spectrometer (DESIS) sensor onboard the International Space Station (ISS), 2. Italian Space Agency's (ASI's) PRISMA (Hyperspectral Precursor of the Application Mission), and 3. Germany's DLR's Environmental Mapping and Analysis Program (EnMAP). Further, Planet Labs PBC recently announced the launch of two hyperspectral sensors called Tanager in 2023. NASA is planning for the hyperspectral sensor Surface Biology and Geology (SBG) to be launched in the coming years. Further, we already have over 70,000 hyperspectral images of the world acquired from NASA's Earth Observing-1 (EO-1) Hyperion that are freely available to anyone from the U.S. Geological Survey's data archives.

These suites of sensors acquire data in 200 plus hyperspectral narrowbands (HNBs) in 2.55 to 12 nm bandwidth, either in 400-1000 or 400-2500 nm spectral range with SBG also acquiring data in the thermal range. In addition, Landsat-NEXT is planning a constellation of 3 satellites each carrying 26 bands in the 400-12,000 nm wavelength range. HNBs provide data as "spectral signatures" in stark contrast to "a few data points along the spectrum" provided by multispectral broadbands (MBBs) such as the Landsat satellite series.

The goal of this special issue is to seek scientific papers that perform research utilizing data from these new generation hyperspectral narrowband (HNB) sensors for a wide array of science applications and compare them with the performance of the multispectral broadband (MBB) sensors such as Landsat, Sentinels, MODIS, IRS, SPOT, and a host of others.

Papers on the following topics are of particular interest:

1. Methods and techniques of understanding, processing, and computing hyperspectral data with specific emphasis on machine learning, deep learning, artificial intelligence (ML/DL/AI), and cloud computing.
2. Issues of hyperspectral data volumes, data redundancy, and overcoming Hughes' phenomenon.
3. Building hyperspectral libraries for purposes of creating reference training, testing, and validation data.
4. Utilizing time-series multispectral data and hyperspectral data over many years to build data cubes and apply advanced computational methods of ML/DL/AI methods and approaches on the cloud.
5. Discussions of hyperspectral data analysis techniques like full spectral analysis versus optimal band analysis.
6. Developing hyperspectral vegetation indices (HVIs) for targeted applications to model and map plant biophysical (e.g., Yield, biomass, leaf area index), biochemical (e.g., Nitrogen, anthocyanins, carotenoids), plant health/stress, and plant structural quantities.
7. Classification of complex vegetation and crop types/species using HNBs and HVIs and comparing them with the performance of multispectral broadband data.

All submissions will be peer-reviewed in line with *PE&RS* policy. Because of page limits, not all submissions recommended for acceptance by the review panel may be included in the special issue. Under this circumstance, the guest editors will select the most relevant papers for inclusion in the special issue. Authors must prepare manuscripts according to the *PE&RS* Instructions to Authors, published in each issue of *PE&RS* and also available on the ASPRS website, https://www.asprs.org/asprs-publications/pers/manuscript-submission.

Special Issue Editors

Dr. Prasad S. Thenkabail, pthenkabail@usgs.gov, thenkabail@gmail.com
Senior Scientist (ST), USGS, Flagstaff, Arizona

Dr. Itiya Aneece, ianeece@usgs.gov
USGS, Flagstaff, Arizona

Dr. Pardhasaradhi Teluguntla, pteluguntla@usgs.gov
USGS, Flagstaff, Arizona

Important Dates

Manuscripts Due — December 15, 2023

Final Papers Due — May 1, 2024

Tentative Publication Date — 2024

Please submit your manuscript — www.editorialmanager.com/asprs-pers/ select "Hyperspectral Remote Sensing"

Call for *PE&RS* Special Issue Submissions

Special Issue on the Scholarship and Impacts of Professor Nina S. N. Lam

Expected Date for Publication: 2024

Special Issue Editors
Michael Leitner (mleitne@lsu.edu)
Jane Read (jaread@syr.edu)

This special issue recognizes Professor Nina S. N. Lam's ~45 years of contribution to Geographic Information and Environmental Sciences. From her first publications on spatial/areal interpolation methods in the early 1980s, she evolved into an internationally recognized scholar known for her leadership in diverse research areas, from scale, resolution, and fractals to environmental health, disaster resilience, and sustainability. Professor Lam, who currently holds the E. L. Abraham Distinguished Professor of Louisiana Environmental Studies title, has been the recipient of many honors and awards, including the inaugural Carolyn Merry Mentoring Award from the UCGIS (2016), being named a Fellow of both the AAG (2020) and the UCGIS (2016), as well as being named a LSU Rainmaker, recognizing one of the top 100 research and creative faculty (2008), and the LSU Distinguished Faculty Award (2006). Her legacy in research, teaching, and service continues through her many students, who are actively contributing to Geographic Information Science (GISc) in academia, government, and the private sector, including the second co-guest editor of this special issue.

This special issue celebrates the outstanding scholarly work of Professor Lam. We invite original contributions from her students, collaborators, and anyone impacted and influenced by her work. Topics covered should be broadly situated within remote sensing, disaster/environmental sciences, sustainability, environmental health, and GISc, including but not limited to subjects related to her research and impact. Please contact special issue editors for questions and suggestions.

Interested authors should send a manuscript title and short abstract (about 250 words, including the authors' names and affiliations) to the special issue editors (mleitne@lsu.edu; jaread@syr.edu) by July 15, 2023 (see complete publication timeline below).

Manuscript length should be around 5,000-6,000 words. All submissions will be subject to standard *PE&RS* peer review processes. See Instructions for authors (https://www.asprs.org/asprs-publications/pers/pers-instructions-for-authors-submitting-a-manuscript-for-peer-review). All submissions should be made online at the Photogrammetric Engineering and Remote Sensing Manuscript Central site (https://www.editorialmanager.com/asprs-pers/). Authors must select "Special Issue" when they reach the "Article Type" step in the submission process and identify the "Scholarship and Impacts of Professor Nina S. N. Lam Special Issue" in their cover letter. New users should first create an account. Once logged on to the site, submissions should be made via the Author Dashboard. Online user guides and access to a help desk are available on this website.

Timeline for publication of *PE&RS* Special Issue

Manuscript Proposal Deadline (Title and Abstract)	July 15, 2023
Submission Deadline	January 31, 2024
Information about Acceptance	On a rolling basis
Submission of Revised Manuscript Deadline	June 30, 2024
Publication in *PE&RS*	2024

Multi-Level Perceptual Network for Urban Building Extraction from High-Resolution Remote Sensing Images

Yueming Sun, Jinlong Chen, Xiao Huang, and Hongsheng Zhang

Abstract

Building extraction from high-resolution remote sensing images benefits various practical applications. However, automation of this process is challenging due to the variety of building surface coverings, complex spatial layouts, different types of structures, and tree occlusion. In this study, we propose a multilayer perception network for building extraction from high-resolution remote sensing images. By constructing parallel networks at different levels, the proposed network retains spatial information of varying feature resolutions and uses the parsing module to perceive the prominent features of buildings, thus enhancing the model's parsing ability to target scale changes and complex urban scenes. Further, a structure-guided loss function is constructed to optimize building extraction edges. Experiments on multi-source remote sensing data sets show that our proposed multi-level perception network presents a superior performance in building extraction tasks.

Introduction

Urban buildings are an essential element in urban environments and serve as an important indicator of the state and scope of urban development. A city building map depicts the distribution, shape, and size of city structures (Zhou *et al.* 2021), which plays a significant role in a variety of city projects (Wang *et al.* 2022). With the continuous development of remote sensing science and technology, the resolution of remote sensing images has been continuously improved (Shao *et al.* 2021). As high-resolution remote sensing images contain rich ground object information such as color, spectrum, texture, shape, and context (Guo *et al.* 2021), they have become an important data source for urban building extraction. The extraction of urban buildings from high-resolution satellite images benefits a variety of fields and tasks, including detecting urban changes, analyzing land use, inspecting and remediating housing safety problems, drawing and updating maps, urban digital three-dimensional modeling, urban planning and construction, to list a few (Alshehhi *et al.* 2017; Zhu *et al.* 2021).

In recent years, with the rapid advancement of deep learning, automated building extraction from high-resolution remote sensing images has become a common practice (Cheng and Han 2016; Luo *et al.* 2021; Shen *et al.* 2022). Convolutional neural networks (CNN)-based deep learning models are widely used in natural image categorization, object identification, and semantic segmentation (Ma *et al.* 2019). The superior performance of CNNs has been demonstrated in automated building extraction from high-resolution remote sensing images (Guo *et al.* 2021; Liu *et al.* 2018). However, CNN retains many notable issues, such as limited perceptual area, erroneous edge segmentation, and spatial information loss (Zhu *et al.* 2021). Following its proposal in 2017 (Shelhamer *et al.* 2017), the fully convolutional network (FCN) has achieved great success in semantic segmentation (Sun *et al.* 2022; Zhuang *et al.* 2019). Marcos *et al.* (2018) propose Rotation Equivariant Vector Field Network (RotEgNet) to encode rotation equivariance in the network itself. Rotation equivariance reduces the model size and runtime memory requirements while keeping most of the orientation information.

It is important to apply deep learning well to building extraction from high-resolution remote sensing images. Shao *et al.* (2020) proposed the Building Residual Refinement Network (BRRNet), which consists of two parts: a prediction module and a residual refinement module. The prediction module is based on an encoder-decoder structure that introduces unordered convolutions with different expansion rates to extract more global features. The residual refinement module refines the residuals between the results of the prediction module and the actual results in one step, thus improving the accuracy of building extraction.

DR-Net uses deeplabv3+ encoder/decoder backbone, combined with densely connected convolutional neural network and residual network structure to greatly reduce the number of parameters in the building extraction model (Chen *et al.* 2018; Yang *et al.* 2020). Combine a grid-based attention gate and a trackless spatial pyramidal pooling module on top of the encoder-decoder architecture to capture and restore building features progressively and efficiently to distinguish buildings from their complex surroundings (Deng *et al.* 2021).

PolygonCNN first performs coarse segmentation to extract the initial building outline (Chen *et al.* 2020), then uses a modified PointNet to learn the shape prior and predicts the deformation of polygon vertices to generate fine-grained building vector results. Xu *et al.* (2022) proposed a gated spatial memory module (GSM) and a centroid-aware head (CH). The GSM transmits semantic information from top down to enhance important features and complement missing information. The CH is used to regress the geometric center of each building to facilitate complete recognition of irregularly shaped buildings. To enhance the boundary extraction of buildings, holistic nested edge detection is used to first extract edge features at the encoder, and then in the boundary enhancement module, the extracted edges and segmentation masks are combined to share mutual information (Jung *et al.* 2022).

CFENet uses the spatial fusion module, the focus enhancement module, and the feature decoder module to perform level-by-level refinement extraction of buildings (Chen *et al.* 2022). A coarse-to-fine boundary refinement network is proposed to extract buildings from remote sensing images accurately (Guo *et al.* 2022). The result of refinement is used as a pseudo-label in the self-supervised process, which increases the robustness of the model against noisy labels or obstacles. Kokila and Jayachandran (2023) proposed a convolutional

Yueming Sun and Jinlong Chen are with the State Key Laboratory of Information Engineering in Surveying, Mapping and Remote Sensing, Wuhan University, Wuhan 430072, China.

Xiao Huang is with the Department of Geosciences, University of Arkansas, Fayetteville, AR 72701.

Hongsheng Zhang is with the Quanzhou Planning and Surveying Institute, School of Urban Design, Wuhan University, Quanzhou 350500, China.

Corresponding author: Jinlong Chen (chenjinlong@whu.edu.cn)

Contributed by Petra Helmholz, July 27, 2022 (sent for review February 8, 2023; reviewed by Andrew Hansen, Dimitri Bulatov).

Photogrammetric Engineering & Remote Sensing
Vol. 89, No. 7, July 2023, pp. 427–434.
0099-1112/22/427–434

doi: 10.14358/PERS.22-00103R1

neural network input layer, three hidden layers, and shifted variation of output layer for accurate detection of buildings from satellite images.

Although the above methods can extract buildings from high-resolution images effectively, issues remain for existing deep learning techniques. In high-resolution remote sensing images, buildings have very complex features with diverse sizes and shapes. The traditional fully convolutional neural networks have a short apparent field of vision and is often insufficient to encompass massive structures and the surrounding background, leading to its poor performance in building extraction (Huang *et al.* 2019). The capability of FCN in extracting building edges is relatively poor when dealing with buildings with complicated edges. Furthermore, current high-resolution remote sensing picture building extraction algorithms suffer from issues such as building shadows, tree occlusions, and incomplete building extraction (Xu *et al.* 2018). In urban areas with complex scenes, there exist many different types of building surface coatings, complicated spatial layouts, and various building shapes and structures. These factors bring great challenges to the automatic extraction of buildings from high-resolution remote sensing images (Huang *et al.* 2019).

In this study, we propose a multi-layer perceptual network-based method for building extraction from high-resolution remote sensing images, aiming to mitigate some of the issues of existing methods, such as differences in building scale, occlusion by trees and shadows, and low accuracy of building edge extraction, and to better parse complex visual environment scenes. The main contributions of this work include: 1) a multi-layer perception network for building extraction from high-resolution remote sensing images. The purpose is to obtain rich, multi-scale features and perceive the outstanding characteristics of buildings, thereby enhancing the model's ability to analyze building scale changes and complex urban scenes in high-resolution remote sensing images. 2) We apply the attention mechanism to the network, aiming to construct a parsing module to enhance the connection of pixels inside buildings and an understanding of their surroundings in the channel and spatial dimensions. As a result, the robustness of building feature extraction under complex backgrounds, shadows, and tree occlusions is improved. 3) We construct a structure-guided loss function to solve the problem of sample imbalance in the building extraction task, where a higher weight is given to the fuzzy boundary to optimize the edge of building extraction.

The remainder of this article is structured as follows. The section "Related Work" presents relevant studies on building extraction using deep learning. The section "Multi-Level Perception Network" explains the proposed multi-layer perceptron network. The "Experimental Results" section describes the experiments and findings. The last section concludes this study.

Related Work

This section compares deep learning-based building extraction approaches to classic high-scoring image building extraction methods and provides an overview of relevant work on building extraction from high-resolution remote sensing images.

Methods for automatically extracting buildings from remote sensing images can be categorized into two groups, i.e., traditional algorithms and deep learning-based techniques (Huang *et al.* 2016). Traditional algorithms are approaches based on artificially designed features, such as building colors, forms, and textures (Shao *et al.* 2020; Zhou and Zhou 2014), which mostly rely on human observation, comprehension, and induction of building attributes (Deng *et al.* 2021). Traditional algorithms can be classified into three types, i.e., edge and vertex detection methods (Sirmacek and Unsalan 2009), region segmentation methods (Lee *et al.* 2003), and multi-source data fusion approaches (Haala and Brenner 1999). However, the extraction results of traditional algorithms often have insufficient accuracy, missing edges, fail to solve the problem of building scale disparities, and fail to match the demands of actual scenes (Liu *et al.* 2022). In comparison, deep learning approaches are characterized by their high extraction accuracy, quick extraction speed, low operating cost, and great repeatability over traditional approaches that rely on artificially constructed features (Gong *et al.* 2020).

Alshehhi *et al.* (2017) proposed a single, patch-based Convolutional Neural Network (CNN) architecture for the extraction of roads and buildings from high-resolution remote sensing data. Liu *et al.* (2018) proposed a multi-level learning framework for building detection from remote sensing images based on CNNs, which can extract the features of buildings at different scales and spatial resolutions. Li *et al.* (2019) proposed a U-Net-based semantic segmentation method for the extraction of building from high-resolution, multispectral satellite images. Guo *et al.* (2021) proposed a new arrangement of a deep learning network named multi-task parallel attention network (MTPA-Net) that considers the scene prior. Hu *et al.* (2021) proposed a novel method called Deep Automatic Building Extraction Network (DABE-Net) for automatic building extraction from remote sensing images. Wang *et al.* (2022) proposed an urban building extraction method based on a multi-scale recurrent conditional generative adversarial network (MSR-cGAN). The extraction accuracy and efficiency of the model have been greatly improved via deep learning, as the area, distribution, number, and position information of building objects can be acquired in a rapid and effective manner.

Multi-Level Perception Network

In this section, we describe the multi-level perception network's fundamental structure and present the key network components, such as the feature extraction module, feature fusion module, and parser module, respectively.

CNN-extracted shallow features are often rich with detailed information, while deep features are rich with semantic information. The traditional building extraction network faces information loss issues due to the multiple pooling process. In this article, we use multi-level network parallelism and feature fusion to connect high-resolution and low-resolution image features, as well as parsing modules, to build a multi-level perception network that effectively improves the extraction accuracy of building information. On one hand, the multi-level parallel structure can simultaneously integrate and interact with multi-level feature information to obtain multi-scale feature perception fields and better capture buildings of various scales, while also effectively retaining the feature information of different resolutions and minimizing the loss of spatial information. On the other hand, the parser module uses spatial attention to direct the network's attention to pixels that correspond to buildings, with channel attention benefiting the discrimination among pixel categories. In this manner, the proposed network is able to suppress non-building information, while giving more weight to building information.

The network structure proposed in this study is shown in Figure 1. After the original image enters the network, 3×3 convolution downsampling with a stride of 2 is used to reduce the size of the feature map, leading to reduced computational demand. Then, we use four bottleneck blocks or basic blocks for feature extraction. After each set of features is extracted, the feature fusion module is used to generate and interact with high- and low-resolution features. A total of four levels are generated, that is, four features with different resolutions, and each level mains an unchanged feature resolution, i.e., the length and width of the feature map are constant.

Further, we input the feature map of the deeper level into the parsing module, restore the scale of the feature information, and continuously upsample the feature map of other levels to the feature map size of the first level. Finally, the feature maps of the four levels are merged and upsampled to the original image size, and the final building prediction map is generated via the softmax function.

Feature Extraction Module

This study is inspired by the residual connection design in the ResNet network module (He *et al.* 2016). The bottleneck module first reduces the dimension of the feature image through 1×1 convolution and then performs a 3×3 convolution operation. Then, the dimension is restored by 1×1 convolution, followed by batch normalization and ReLU layers, with a residual connection to the input. The basic module

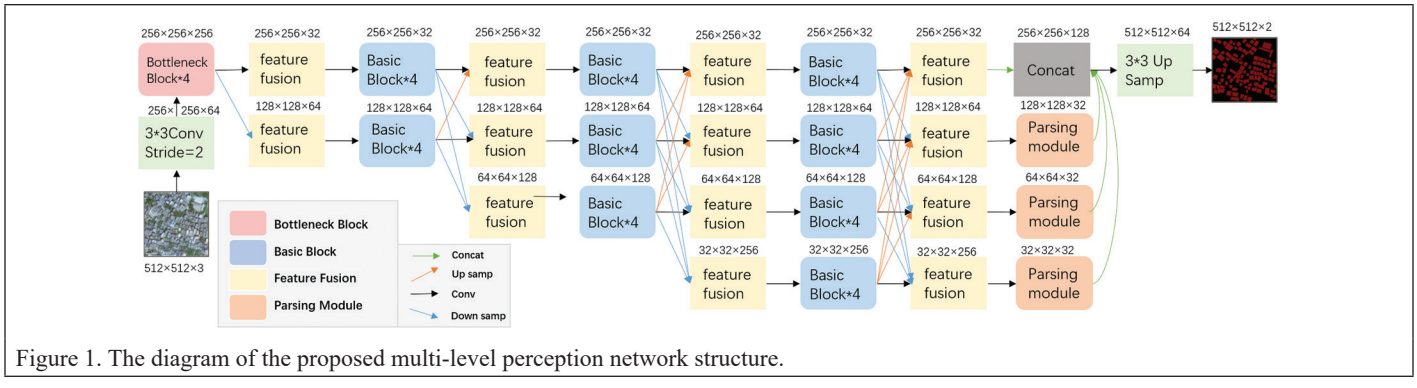

Figure 1. The diagram of the proposed multi-level perception network structure.

contains two 3 × 3 convolution operations and one residual connection, as shown in Figure 2.

Feature Fusion Module

The feature fusion module constructed in this paper is shown in Figure 3, which is used to strengthen the combination and use of deep and shallow features between different layers of networks. For each level of the feature fusion module, we keep the feature map obtained by this level of feature extraction unchanged. For the feature maps obtained from other levels of feature extraction, the low-resolution feature map is passed through a 1 × 1 convolution to keep the number of channels in the same dimension as the feature map of this level. Then, the low-resolution feature map is changed to the same size as the feature map of this level using upsampling interpolation. The high-resolution feature map is passed through a convolution kernel of size 3 × 3 with a step size of 2. The convolution with the same number of channels as the feature map of this level is down-sampled to the size of the feature map of this level. Further, the channels of the feature maps at each level are superimposed to achieve feature fusion.

Parser Module

The parsing module constructed in this paper is shown in Figure 4. The parsing module recalibrates the input features in both spatial and channel dimensions, allowing the network to learn more meaningful feature maps.

We set $U = [u^{1,1}, u^{1,2}, u^{i,j}, \ldots, u^{H,W}]$ as input feature, where $u^{i,j} \in \mathbb{R}^{1\times1\times C}$ represents the channel characteristics of each spatial location, $i \in \{1, 2, \ldots, H\}$, $j \in \{1, 2, \ldots, W\}$. H, W, and C are the height, width, and number of input channels, respectively. In the spatial attention cell, the input features are first convolved by a 1 × 1 kernel to produce their two-dimensional spatial attention maps $q(q \in \mathbb{R}^{H\times W})$. We activate the obtained q by the sigmoid function σ. The obtained spatial weight values set more attention to the building-related spatial locations to obtain the calibrated spatial feature map $\hat{U}$.

$$\hat{U} = [\sigma(q^{1,1})u^{1,1}, \ldots, \sigma(q^{i,j})u^{i,j}, \ldots, \sigma(q^{H,W})u^{H,W}] \quad (1)$$

In the channel attention cell, each channel of the spatial feature map is weighted to indicate the correlation between the channel and the key information. Global average pooling is used to generate the channel global feature S vectors, $S \in \mathbb{R}^{1\times1\times C}$,

$$S = \frac{1}{H \cdot W}\sum_{i}^{H}\sum_{j}^{W}\hat{u}(i,j)\# \quad (2)$$

Then a bottleneck structure with two fully connected (FC) layers used, where the first FC layer is dimensionally reduced and the second FC layer restores the original dimensionality. Then, the channel weights are obtained via the sigmoid layer,

$$\hat{S} = \sigma(W_2(\zeta(W_1 S))) \quad (3)$$

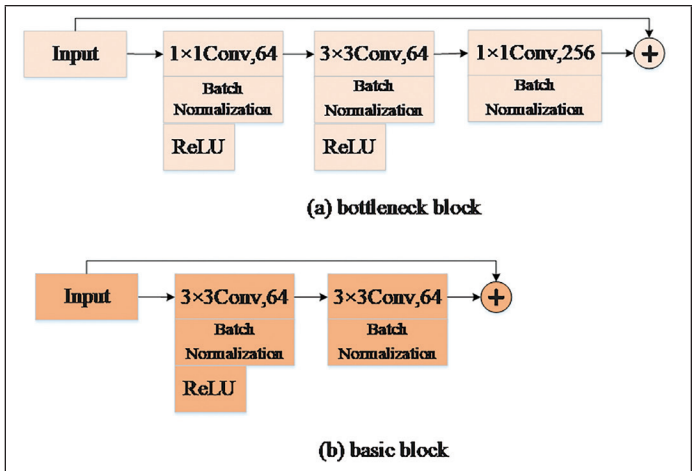

Figure 2. The feature extraction module of the proposed multi-level perception network.

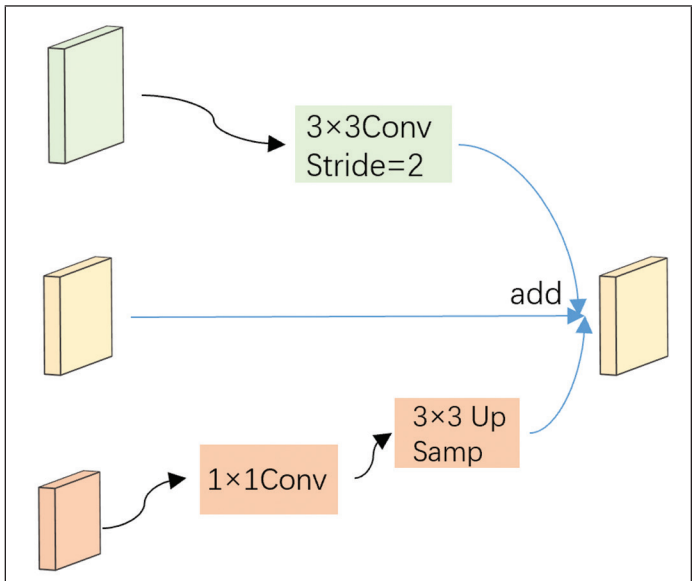

Figure 3. The feature fusion module of the proposed multi-level perception network.

where ζ denotes the ReLU activation function, $W_1 \in \mathbb{R}^{C\times\frac{C}{r}}$ and $W_2 \in \mathbb{R}^{\frac{C}{r}\times C}$ represent the FC layers, and σ denotes the sigmoid activation function. The obtained channel weights recalibrate the feature map $\ddot{U}$:

$$\ddot{U} = [\hat{s}_1\hat{u}_1, \hat{s}_i\hat{u}_i, \ldots, \hat{s}_C\hat{u}_C] \quad (4)$$

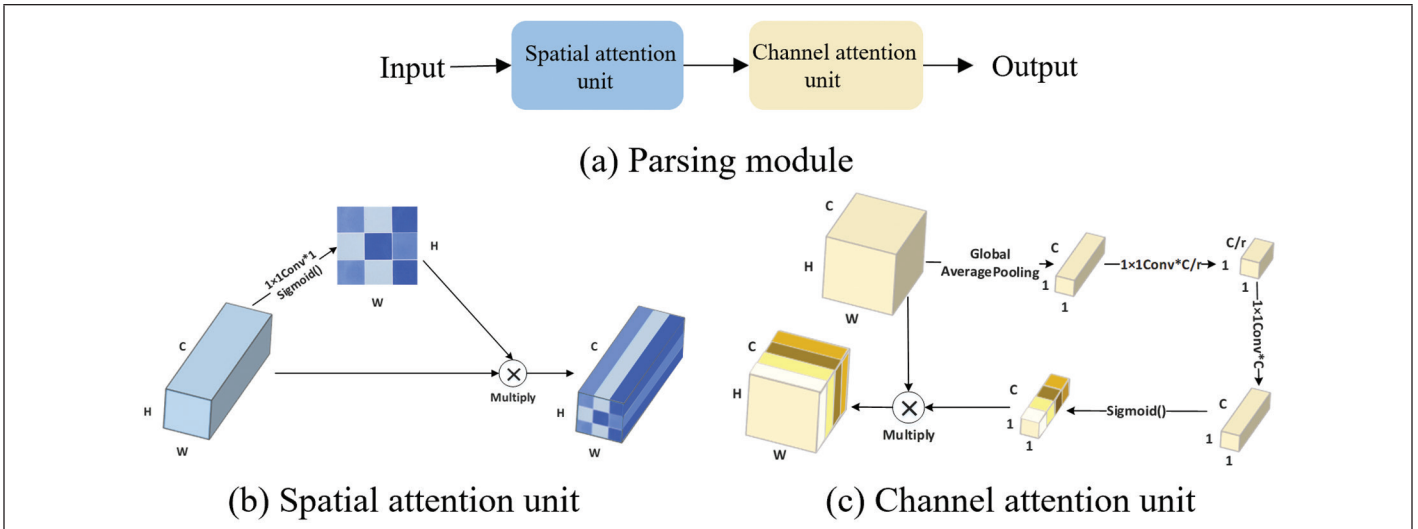

Figure 4. The parsing module of the proposed multi-level perception network.

Loss Function

The focus loss function introduces a focus parameter γ for constructing the modulation coefficient $(1 - g_i)^{\gamma}$, where $\gamma \geq 0$. The modulation factors allow the model to focus more on a smaller number of categories (Lin *et al.* 2017). Multi-scale structural similarity (MS-SSIM) is a measure of the similarity of two images (Wang *et al.* 2004, 2003). MS-SSIM takes into account the local domain of pixels and assigns a higher weight to the boundary, even if the predicted probability on the boundary is the same as the rest of the foreground, with the loss near the boundary relatively higher. Therefore, in order to get higher quality area segmentation effect and clearer boundary, we construct a hybrid loss function for building extraction, aiming to obtain clear boundaries of multi-scale targets and address the imbalance issue in building and background information.

$$L_{\text{ms-ssim}} = 1 - \prod_{m=1}^{M} \left[\frac{2\mu_p \mu_g + C_1}{\mu_p^2 + \mu_g^2 + C_1} \right]^{\beta_m} \left[\frac{2\sigma_{pg} + C_2}{\sigma_p^2 + \sigma_g^2 + C_2} \right]^{\gamma_m} \tag{5}$$

$$L_{fl} = -\sum_{i=1}^{I} \alpha_i \left(1 - g_i\right)^{\gamma} \log(g_i) \tag{6}$$

$$L_{\text{building}} = L_{fl} + L_{\text{ms-ssim}} \tag{7}$$

where p is the sample and g is the network output label. μ_p, μ_g and σ_p, σ_g are the mean and variance of p and g. σ_{pg} represents their covariance. β_m and γ_m define the relative importance of the two components in each scale. m stands for different scales and is five in total. $\beta_1 = \gamma_1 = 0.0448$, $\beta_2 = \gamma_2 = 0.2856$, $\beta_3 = \gamma_3 = 0.3001$, $\beta_4 = \gamma_4 = 0.2363$, $\beta_5 = \gamma_5 = 0.1333$. $C_1 = 0.01^2$ and $C_2 = 0.03^2$ aim to avoid zero division.

Experimental Results

In order to evaluate the performance of the proposed network in the building extraction task, experimental analysis is performed in this section. The next section, "Training and Testing" introduces the data set used for the experiments. The section "Evaluation" presents the objective metrics used to evaluate the experimental results. The "Implementation" section shows the results of the comparative experiments of the proposed method on the Fujian building intelligence census data set, and evaluates the results qualitatively and quantitatively. The section "Generalization" shows the results of the proposed method on the Quanzhou high-resolution building data set. It fully illustrates the superiority and generalizability of multi-level perceptual network in the extraction of buildings from high resolution remote sensing images.

Training and Testing

To test the effectiveness of the multi-level perception network, we use a publicly available Fujian building intelligence census data set (Fujian building intelligence census (Fbic) data set: https://tianchi.aliyun.com/competition/entrance/231767/information). The Fbic data set contains 0.8 m resolution *Gaofen-2* satellite images from eight representative experimental areas, each covering an area of about 12 square kilometers. We randomly crop a total of 10 000 small patches (512 × 512) from the data set without overlapping, of which 8000 are used as the training set, 1000 as the validation set, and 1000 as the test set. Some examples of this data set are presented in Figure 5.

In addition, in order to verify the reliability and generalization of the model, we construct a Quanzhou high-resolution building data set (Quanzhou high-resolution building (Qhrb) data set) with high-view satellite remote sensing images of a resolution of 0.5 m. We select high-resolution remote sensing images that cover cities, towns, and rural areas and label them manually by drawing vectors of building rooftop outlines. The data set includes a total of 1494 high-resolution remote sensing images with a size of 512 × 512 pixels, covering buildings with different structures, roofing forms, and materials. Some examples in the Qhrb data set are presented in Figure 6.

Evaluation

We apply pixel-level evaluation metrics that include Intersection over Union (IoU), F1 score, mean Intersection over Union (MIoU), and mean Pixel Accuracy (MPA).

IoU refers to the ratio of the intersection and union of the prediction result of a certain category and the true value of the model:

$$\text{IoU} = \frac{\text{TP}}{\text{TP} + \text{FP} + \text{FN}} \tag{8}$$

where TP means true positive, FP means false positive, FN means false negative.

The F1 score is equivalent to the harmonic mean of the precision and recall, with 1 being the best value and 0 being the worst:

$$\text{Precision} = \frac{\text{TP}}{\text{TP} + \text{FP}} \tag{9}$$

$$\text{Recall} = \frac{TP}{\text{TP} + \text{FN}} \tag{10}$$

$$F1 = 2 \cdot \frac{\text{precision} \cdot \text{recall}}{\text{precision} + \text{recall}} \tag{11}$$

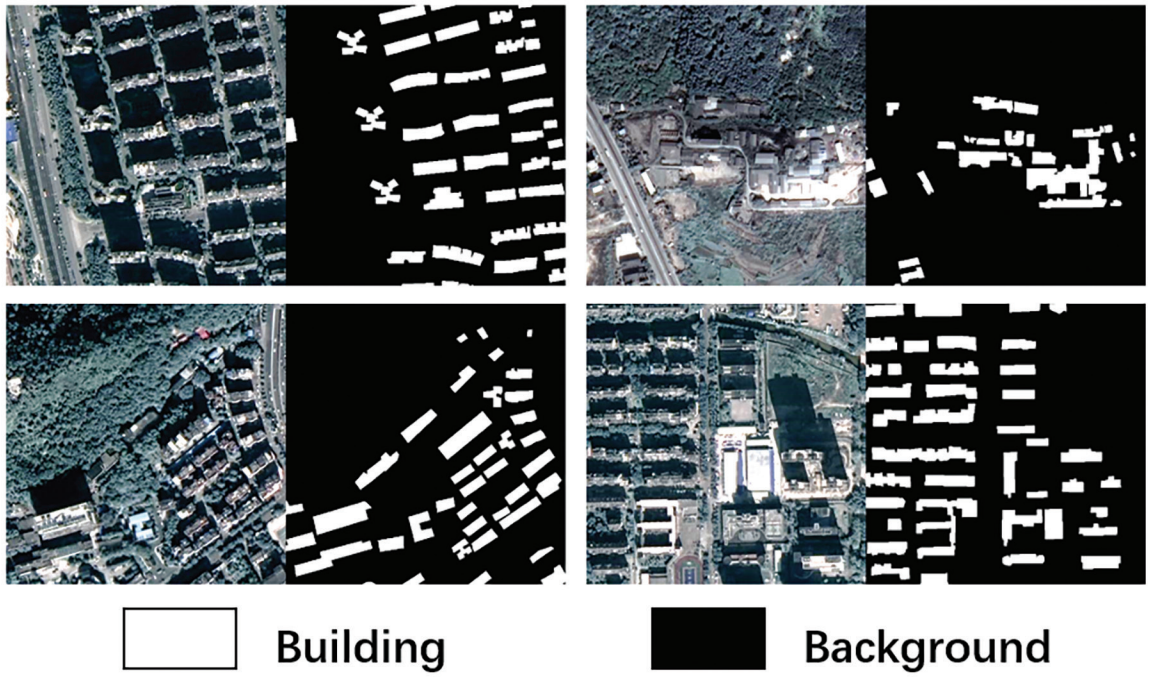

Figure 5. Examples of Fujian building intelligence census (Fbic) data set.

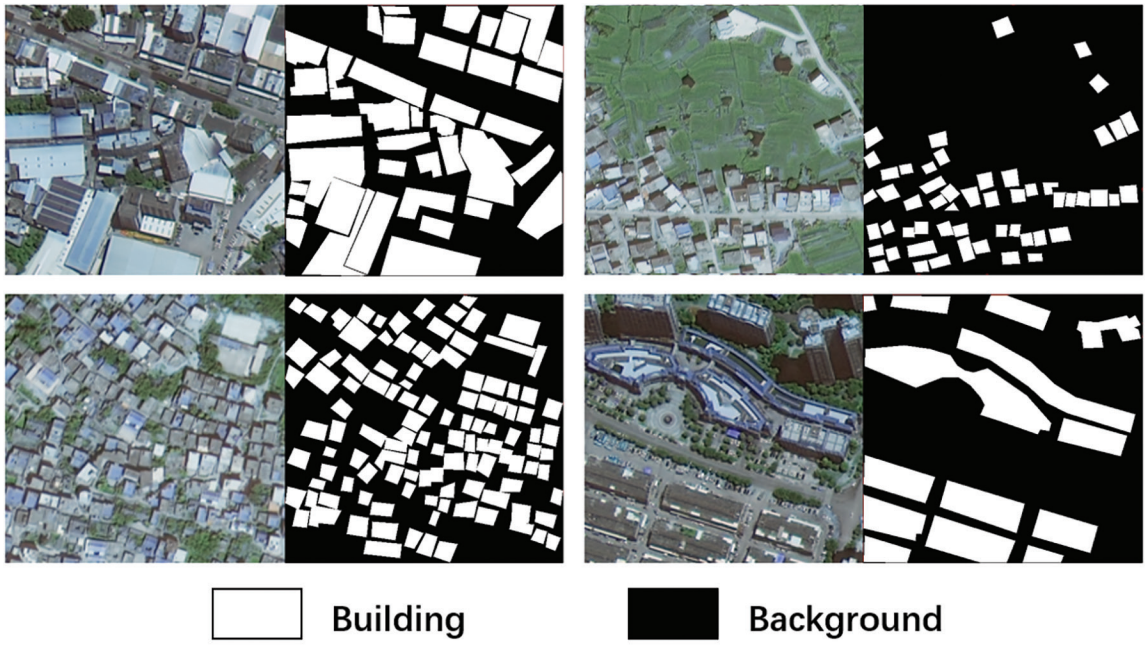

Figure 6. Examples of the Quanzhou high-resolution building (Qhrb) data set.

MIoU refers to the ratio of the intersection and union of the result of the model's prediction for each category and the true value. The calculation formula of the summed and averaged results is as follows:

$$\mathrm{MIoU} = \frac{1}{k+1}\sum_{i=0}^{k}\frac{pii}{\sum_{j=0}^{k}p_{ij}+\sum_{j=0}^{k}p_{ji}-p_{ii}} \tag{12}$$

where i represents the true value, j represents the predicted value, and p_{ij} represents the prediction of i as j.

MPA refers to the average pixel accuracy of the category:

$$\mathrm{MPA} = \frac{\mathrm{sum}(Pi)}{N} \tag{13}$$

where P_i is the pixel accuracy of each category and N is the number of categories.

Implementation

We implement our model in Tensorflow. All experiments run on a desktop computer with two CPUs, 64 GB of memory, and four NVIDIA Quadro K620 GPUs under the Ubuntu 16.04 OS. The model uses the Adam optimizer for gradient descent. The learning rate reduces to half, if the loss of the validation set fails to drop in three epochs. We set the batch size to 16, the initial learning rate to 1e-4, and the total epoch to 300.

In the same training environment, we conduct a comparative analysis with three widely used deep learning models, i.e., U-Net (Ronneberger *et al.* 2015), Pspnet (Zhao *et al.* 2017), and Deeplabv3+ (Chen *et al.* 2018). Table 1 shows comparative test results of the

proposed model again the other three competing methods. It can be seen that the overall extraction accuracy of our proposed method is better than that of U-Net, Pspnet, and Deeplabv3+. For the IOU, our method achieves 92.44% and 98.98% accuracy in building extraction and background identification, respectively, 8.29% and 1.18% higher than the second-best performing U-Net network. For F1, our method achieves 96.07% and 99.48% accuracy in building extraction and background identification, respectively, 4.68% and 0.59% higher than the second-best performing U-Net. The accuracy of our method reaches 95.71% and 97.64% in MIoU and MPA metrics, respectively, 4.73% and 2.86% higher than the second-best performing U-Net. The above results suggest that our proposed method is very effective in extracting buildings from high-resolution remote sensing images.

Selected building extraction results on the Fbic data set using U-Net, Pspnet, Deeplabv3+, and the proposed method are shown in Figure 7. As shown in Figure 7a, we notice that U-Net, Pspnet, and Deeplabv3+ have notable insufficiency identified building extraction results. Compared with other methods, the red part representing underclassification and the blue part representing misclassification are much less in the extraction results of our method, which fully demonstrates that the buildings extracted by our method are more accurate. The highlighted yellow boxes suggest regions where our method outperforms other competing methods, as it demonstrates the completeness of building details. As shown in Figures 7b and 7c, we notice that U-Net, Pspnet, and Deeplabv3+ fail to identify small building targets in complex backgrounds, as they have insufficient background analysis for dense building areas. In comparison, our method outperforms the other three methods in both complex background parsing and small object recognition. As shown in Figure 7d, for the scale change problem of automatic building extraction from high-resolution remote sensing images, our method also achieves satisfactory performance in large-scale target recognition and building boundary extraction. As shown in Figure 7e, the other three methods are prone to the problem of blurred boundaries when dealing with irregular targets. However, the proposed model outperforms the competing models in terms of identifying irregular objects. The above quantitative and qualitative evidence demonstrates the superiority of our proposed model well in extracting buildings.

Generalization

Generalizability refers to the ability of a model to be trained to apply to new data and make accurate predictions (Ji *et al.* 2019). In this study, the generalizability of the multi-level perception network is verified using the Qhrb data set with a higher spatial resolution. The validation results

Table 1. Comparison of building extraction accuracy between our method and U-Net, Pspnet, and Deeplabv3+ deep learning network models.

	IoU (%)		F1 (%)		MIoU	MPA
Methods	**Building**	**Background**	**Building**	**Background**	**(%)**	**(%)**
U-net	84.15	97.8	91.39	98.89	90.98	94.78
Pspnet	77.71	96.78	87.45	98.36	87.24	92.74
Deeplabv3+	80.59	97.14	89.25	98.55	88.86	93.45
Ours	92.44	98.98	96.07	99.48	95.71	97.64

IoU = Intersection over Union; F1 = F1 score; MIoU = mean Intersection over Union; MPA = mean Pixel Accuracy.

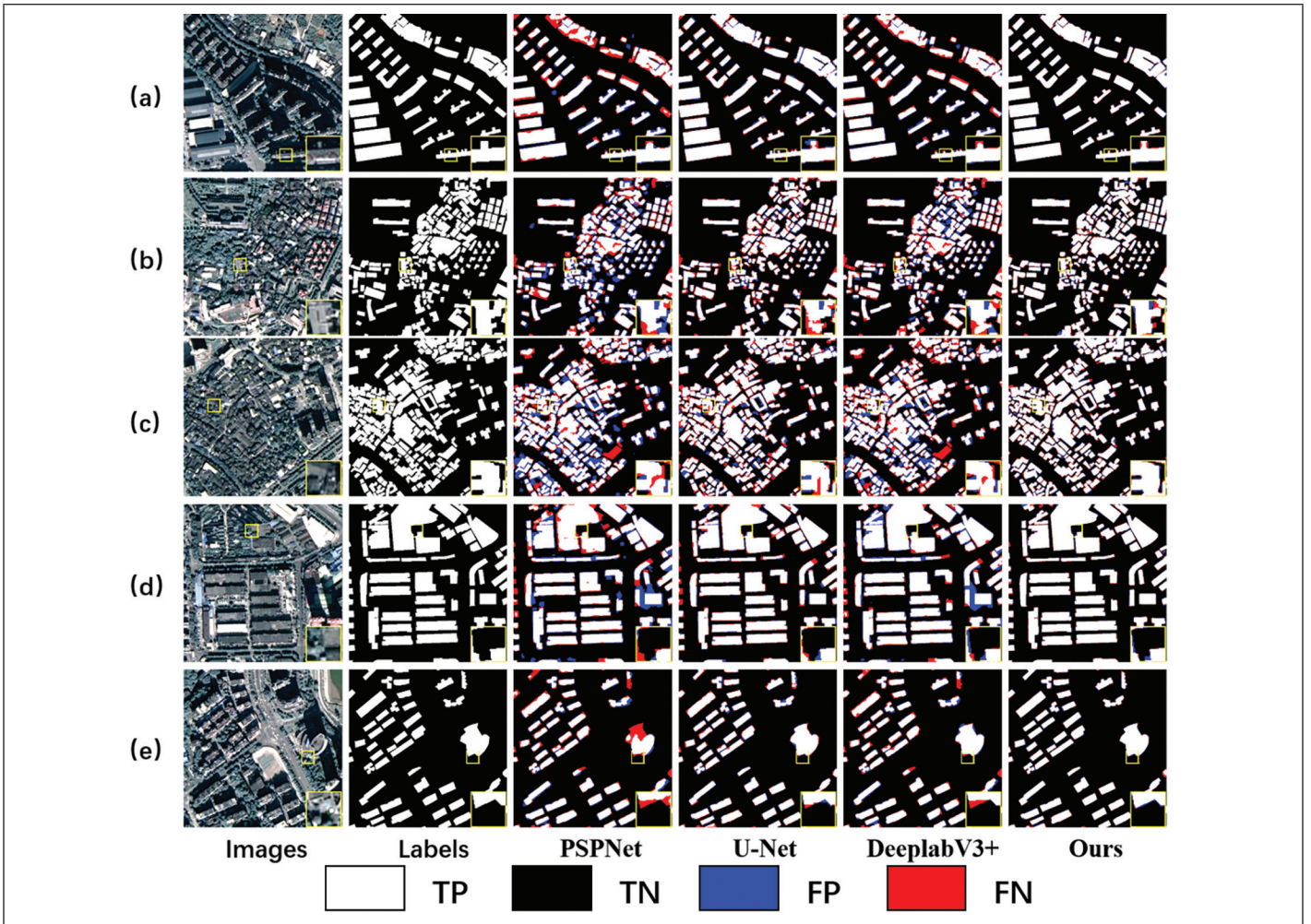

Figure 7. Building extraction results on the Fujian building intelligence census (Fbic) data set with U-Net, Pspnet, Deeplabv3+, and the proposed model.

are shown in Table 2, and selected building extraction results are shown in Figure 8. It can be found that the method proposed in this study maintains great extraction results in different regions using data sources, suggesting its superior generalizability. The test results on the high-view satellite image of Quanzhou City suggest that the MIoU reaches 88.47% and MPA reaches 97.89%. As can be seen in Figure 8, most of the buildings are accurately recognized, with complete edges and satisfactory detection for dense small/large buildings and irregular buildings.

Table 2. Building extraction accuracy among our model on the Quanzhou high-resolution building (Qhrb) data set.

	IoU (%)		F1 (%)		MIoU	MPA
Methods	**Building**	**Background**	**Building**	**Background**	**(%)**	**(%)**
Ours	81.06	91.99	89.54	99.48	88.47	97.89

IoU = Intersection over Union; F1 = F1 score; MIoU = mean Intersection over Union; MPA = mean Pixel Accuracy.

Conclusions

In this paper, we propose a multi-layer perception network for building extraction from high-resolution remote sensing images, which effectively improves the accuracy of building extraction. By constructing parallel networks at different levels, we extract deep semantic features while retaining shallow detail information, at the same time, fusing multi-level feature information to obtain multi-scale feature receptive fields. To improve the detection in complex urban environments, the analysis module is used to recognize the important features of the structure and suppress the importance of irrelevant elements, thus improving the performance and adaptability of the model in practical applications of large-scale, high-resolution image building extraction with complex scenes. Additionally, the concept of multi-scale structural similarity is introduced to construct a loss function that facilitates the generation of clear boundaries. The efficacy and efficiency of the suggested strategy for various building extraction tasks in complex visual environments are demonstrated by a comparative study using multi-source, high-resolution remote sensing image building data sets. Compared with other deep learning algorithms, the proposed method can effectively solve the problems of large changes in target scale, complex building background, severe tree and shadow occlusion, and irregular building edge extraction. In future work, we will perform a lightweight design of the model and find more suitable attention modules and multi-scale feature fusion mechanisms.

References

Alshehhi, R., P. R. Marpu, W. L. Woon and M. D. Mura. 2017. Simultaneous extraction of roads and buildings in remote sensing imagery with convolutional neural networks. *ISPRS Journal of Photogrammetry and Remote Sensing* 130:139–149. https://doi.org/10.1016/j.isprsjprs.2017.05.002.

Chen, J., D. Zhang, Y. Wu, Y. Chen and X. Yan. 2022. A context feature enhancement network for building extraction from high-resolution remote sensing imagery. *Remote Sensing* 14:1–19. https://doi.org/10.3390/rs14092276.

Chen, L.-C., Y. Zhu, G. Papandreou, F. Schroff and H. Adam. 2018. Encoder-decoder with atrous separable convolution for semantic image segmentation BT. Pages 833–851 in *Proceedings European Conference on Computer Vision (ECCV) 2018*, held in Munich, Germany, 8–14 September 2018. Edited by V. Ferrari, M. Hebert, C. Sminchisescu and Y. Weiss. https://doi.org/10.48550/arXiv.1802.02611.

Chen, Q., L. Wang, S. L. Waslander and X. Liu. 2020. An end-to-end shape modeling framework for vectorized building outline generation from aerial images. *ISPRS Journal of Photogrammetry and Remote Sensing* 170:114–126. https://doi.org/10.1016/j.isprsjprs.2020.10.008.

Cheng, G. and J. Han. 2016. A survey on object detection in optical remote sensing images. *ISPRS Journal of Photogrammetry and Remote Sensing* 117:11–28. https://doi.org/10.1016/j.isprsjprs.2016.03.014.

Deng, W., Q. Shi and J. Li. 2021. Attention-gate-based encoder-decoder network for automatical building extraction. *IEEE Journal of Selected Topics in Applied Earth Observations and Remote Sensing* 14:2611–2620. https://doi.org/10.1109/JSTARS.2021.3058097.

Gong, J., C. Liu and X. Huang. 2020. Advances in urban information extraction from high-resolution remote sensing imagery. *Science China Earth Sciences* 63:463–475. https://doi.org/10.1007/s11430-019-9547-x.

Guo, H., B. Du, L. Zhang and X. Su. 2022. A coarse-to-fine boundary refinement network for building footprint extraction from remote sensing imagery. *ISPRS Journal of Photogrammetry and Remote Sensing* 183:240–252. https://doi.org/10.1016/j.isprsjprs.2021.11.005.

Guo, H., Q. Shi, B. Du, L. Zhang, D. Wang and H. Ding. 2021. Scene-driven multitask parallel attention network for building extraction in high-resolution remote sensing images. *IEEE Transactions on Geoscience and Remote Sensing* 59:4287–4306. https://doi.org/10.1109/TGRS.2020.3014312.

Haala, N. and C. Brenner. 1999. Extraction of buildings and trees in urban environments. *ISPRS Journal of Photogrammetry and Remote Sensing* 54:130–137. https://doi.org/10.1016/S0924-2716(99)00010-6.

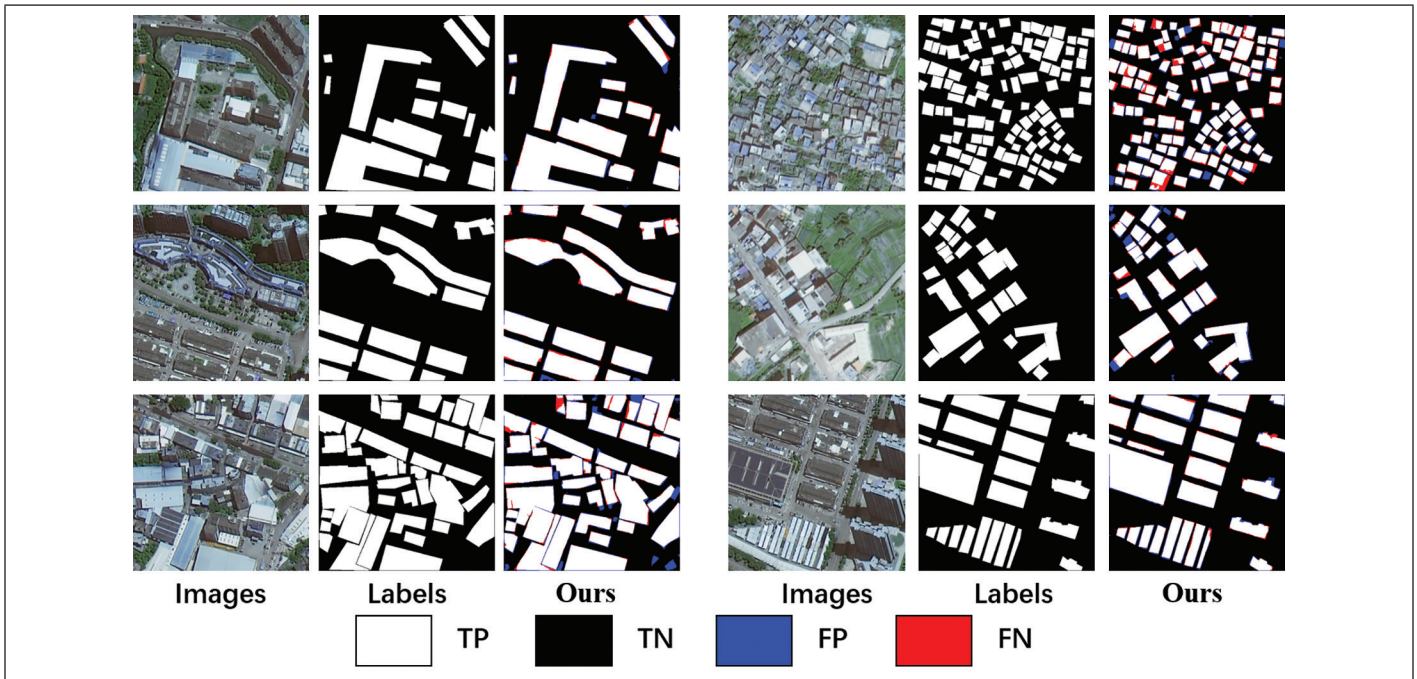

Figure 8. Building extraction results on the Quanzhou high-resolution building (Qhrb) data set from the proposed multi-level perception network.

He, K., X. Zhang, S. Ren and J. Sun. 2016. Deep residual learning for image recognition. Pages 770–778 in *Proceedings IEEE Conference on Computer Vision and Pattern Recognition (CVPR)*, held in Las Vegas, Nev., 27–30 June 2016. https://doi.org/10.1109/CVPR.2016.90.

Hu, Q., L. Zhen, Y. Mao, X. Zhou and G. Zhou. 2021. Automated building extraction using satellite remote sensing imagery. *Automation in Construction* 123:103509. https://doi.org/10.1016/j.autcon.2020.103509.

Huang, J., X. Zhang, Q. Xin, Y. Sun and P. Zhang. 2019. Automatic building extraction from high-resolution aerial images and LiDAR data using gated residual refinement network. *ISPRS Journal of Photogrammetry and Remote Sensing* 151:91–105. https://doi.org/10.1016/j.isprsjprs.2019.02.019.

Huang, Z., G. Cheng, H. Wang, H. Li, L. Shi and C. Pan. 2016. Building extraction from multi-source remote sensing images via deep deconvolution neural networks. Pages 1835–1838 in *Proceedings 2016 IEEE International Geoscience and Remote Sensing Symposium (IGARSS)*, held in Beijing, China, 10–15 July 2016. https://doi.org/10.1109/IGARSS.2016.7729471.

Ji, S., S. Wei and M. Lu. 2019. Fully convolutional networks for multisource building extraction from an open aerial and satellite imagery data set. *IEEE Transactions on Geoscience and Remote Sensing* 57:574–586. https://doi.org/10.1109/TGRS.2018.2858817.

Jung, H., H. S. Choi and M. Kang. 2022. Boundary enhancement semantic segmentation for building extraction from remote sensed image. *IEEE Transactions on Geoscience and Remote Sensing* 60:1–12. https://doi.org/10.1109/TGRS.2021.3108781.

Kokila, S. and A. Jayachandran. 2023. Bias variance Toeplitz matrix based shift invariance classifier for building detection from satellite images. *Remote Sensing Applications: Society and Environment* 29:100881. https://doi.org/10.1016/j.rsase.2022.100881.

Lee, D. S., J. Shan and J. S. Bethel. 2003. Class-guided building extraction from Ikonos imagery. *Photogrammetric Engineering & Remote Sensing* 69:143–150. https://doi.org/10.14358/PERS.69.2.143.

Li, W., C. He, J. Fang, J. Zheng, H. Fu and L. Yu. 2019. Semantic segmentation-based building footprint extraction using very high-resolution satellite images and multi-source GIS data. *Remote Sensing* 11(4):403. https://doi.org/10.3390/rs11040403

Lin, T. Y., P. Goyal, R. Girshick, K. He and P. Dollar. 2017. Focal loss for dense object detection. Pages 2999–3007 in *Proceedings 2017 IEEE International Conference on Computer Vision (ICCV)*, held in Venice, Italy, 22–29 October 2017. https://doi.org/10.1109/ICCV.2017.324.

Liu, X., Y. Chen, M. Wei, C. Wang, W. N. Goncalves, J. Marcato and J. Li. 2022. Building instance extraction method based on improved hybrid task cascade. *IEEE Geoscience and Remote Sensing Letters* 19:19–23. https://doi.org/10.1109/LGRS.2021.3060960.

Liu, Y., Z. Zhang, R. Zhong, D. Chen, Y. Ke, J. Peethambaran, C. Chen and L. Sun. 2018. Multilevel building detection framework in remote sensing images based on convolutional neural networks. *IEEE Journal of Selected Topics in Applied Earth Observations and Remote Sensing* 11:3688–3700. https://doi.org/10.1109/JSTARS.2018.2866284.

Luo, L., P. Li and X. Yan. 2021. Deep learning-based building extraction from remote sensing images: A comprehensive review. *Energies* 14:1–25. https://doi.org/10.3390/en14237982.

Ma, L., Y. Liu, X. Zhang, Y. Ye, G. Yin and B. A. Johnson. 2019. Deep learning in remote sensing applications: A meta-analysis and review. *ISPRS Journal of Photogrammetry and Remote Sensing* 152:166–177. https://doi.org/10.1016/j.isprsjprs.2019.04.015.

Marcos, D., M. Volpi, B. Kellenberger and D. Tuia. 2018. Land cover mapping at very high resolution with rotation equivariant CNNs: Towards small yet accurate models. *ISPRS Journal of Photogrammetry and Remote Sensing* 145:96–107. https://doi.org/10.1016/j.isprsjprs.2018.01.021.

Ronneberger, O., P. Fischer and T. Brox. 2015. U-Net: Convolutional networks for biomedical image segmentation. In *Medical Image Computing and Computer-Assisted Intervention–MICCAI 2015*, edited by N. Navab, J. Hornegger, W. M. Wells and A. F. Frangi, 234–241. Cham, Germany: Springer International Publishing. https://doi.org/10.48550/arXiv.1505.04597.

Shao, Z., P. Tang, Z. Wang, N. Saleem, S. Yam and C. Sommai. 2020. BRRNet: A fully convolutional neural network for automatic building extraction from high-resolution remote sensing images. *Remote Sensing* 12:1–17. https://doi.org/10.3390/rs12061050.

Shao, Z., W. Wu and D. Li. 2021. Spatio-temporal-spectral observation model for urban remote sensing. *Geo-Spatial Information Science* 24:372–386. https://doi.org/10.1080/10095020.2020.1864232.

Shelhamer, E., J. Long and T. Darrell. 2017. Fully convolutional networks for semantic segmentation. *IEEE Transactions on Pattern Analysis and Machine Intelligence* 39(4):640–651. https://doi.org/10.1109/TPAMI.2016.2572683.

Shen, Y., T. Ai, H. Chen and J. Li. 2022. Multilevel mapping from remote sensing images: A case study of urban buildings. *IEEE Transactions on Geoscience and Remote Sensing* 60:1–16. https://doi.org/10.1109/TGRS.2021.3062751.

Sirmacek, B. and C. Unsalan. 2009. Urban-area and building detection using SIFT keypoints and graph theory. *IEEE Transactions on Geoscience and Remote Sensing* 47:1156–1167. https://doi.org/10.1109/TGRS.2008.2008440.

Sun, Y., X. Zhang, J. Huang, H. Wang and Q. Xin. 2022. Fine-grained building change detection from very high-spatial-resolution remote sensing images based on deep multitask learning. *IEEE Geoscience and Remote Sensing Letters* 19:1–5. https://doi.org/10.1109/LGRS.2020.3018858.

Wang, Z., A. C. Bovik, H. R. Sheikh and E. P. Simoncelli. 2004. Image quality assessment: From error visibility to structural similarity. *IEEE Transactions on Image Processing* 13:600–612. https://doi.org/10.1109/TIP.2003.819861.

Wang, Z., E. Simoncelli and A. C. Bovik. 2003. Multiscale structural similarity for image quality assessment. Pages 1398–1402 in *Proceedings Thirty-Seventh Asilomar Conference on Signals, Systems & Computers*, held in Pacific Grove, Calif., 9–12 November 2003. https://doi.org/10.1109/ACSSC.2003.1292216.

Wang, Z., N. Xu, B. Wang, Y. Liu and S. Zhang. 2022. Urban building extraction from high-resolution remote sensing imagery based on multi-scale recurrent conditional generative adversarial network. *GIScience Remote Sensing* 59:861–884. https://doi.org/10.1080/15481603.2022.2076382.

Xu, L., Y. Li, J. Xu and L. Guo. 2022. Gated spatial memory and centroid-aware network for building instance extraction. *IEEE Transactions on Geoscience and Remote Sensing* 60:1–14. https://doi.org/10.1109/TGRS.2021.3073164.

Xu, Y., L. Wu, Z. Xie and Z. Chen. 2018. Building extraction in very high resolution remote sensing imagery using deep learning and guided filters. *Remote Sensing* 10(1):144. https://doi.org/10.3390/rs10010144.

Yang, Z., H. Yu, M. Feng, W. Sun, X. Lin, M. Sun, Z. H. Mao and A. Mian. 2020. Small object augmentation of urban scenes for real-time semantic segmentation. *IEEE Transactions on Image Processing* 29:5175–5190. https://doi.org/10.1109/TIP.2020.2976856.

Zhao, H., J. Shi, X. Qi, X. Wang and J. Jia. 2017. Pyramid scene parsing network. Pages 6230–6239 in *Proceedings 2017 IEEE Conference on Computer Vision and Pattern Recognition (CVPR)*, held in Honolulu, Hawaii, 21–26 July 2017. https://doi.org/10.1109/CVPR.2017.660.

Zhou, D., G. Wang, G. He, R. Yin, T. Long, Z. Zhang, S. Chen and B. Luo. 2021. A large-scale mapping scheme for urban building from Gaofen-2 images using deep learning and hierarchical approach. *IEEE Journal of Selected Topics in Applied Earth Observations and Remote Sensing* 14:11530–11545. https://doi.org/10.1109/JSTARS.2021.3123398.

Zhou, G. and X. Zhou. 2014. Seamless fusion of LiDAR and aerial imagery for building extraction. *IEEE Transactions on Geoscience and Remote Sensing* 52:7393–7407. https://doi.org/10.1109/TGRS.2014.2311991.

Zhu, Q., C. Liao, H. Hu, X. Mei and H. Li. 2021. MAP-Net: Multiple attending path neural network for building footprint extraction from remote sensed imagery. *IEEE Transactions on Geoscience and Remote Sensing* 59:6169–6181. https://doi.org/10.1109/TGRS.2020.3026051.

Zhuang, J., J. Yang, L. Gu and N. Dvornek. 2019. Shelfnet for fast semantic segmentation. Pages 847–856 in *Proceedings 2019 IEEE/CVF International Conference on Computer Vision Workshop (ICCVW)*, held in Seoul, Korea (South), 27–28 October 2019. https://doi.org/10.1109/ICCVW.2019.00113.

SUSTAININGMEMBERS

ACI USA Inc.
Weston, Florida
https://acicorporation.com/
Member Since: 2/2018

Aerial Services, Inc.
Cedar Falls, Iowa
www.AerialServicesInc.com
Member Since: 5/2001

Airworks Solutions Inc.
Boston, Massachusetts
Member Since: 3/2022

Applanix
Richmond Hill, Ontario, Canada
http://www.applanix.com
Member Since: 7/1997

Ayres Associates
Madison, Wisconsin
www.AyresAssociates.com
Member Since: 1/1953

Cardinal Systems, LLC
Flagler Beach, Florida
www.cardinalsystems.net
Member Since: 1/2001

Dewberry
Fairfax, Virginia
www.dewberry.com
Member Since: 1/1985

Esri
Redlands, California
www.esri.com
Member Since: 1/1987

GeoCue Group
Madison, Alabama
http://www.geocue.com
Member Since: 10/2003

Geographic Imperatives LLC
Centennial, Colorado
Member Since: 12/2020

GeoWing Mapping, Inc.
Richmond, California
www.geowingmapping.com
Member Since: 12/2016

GPI Geospatial Inc.
Orlando, Florida
www.aca-net.com
Member Since: 1/1994

Halff Associates, Inc.
Richardson, Texas
www.halff.com
Member Since: 8/2021

Keystone Aerial Surveys, Inc.
Philadelphia, Pennsylvania
www.kasurveys.com
Member Since: 1/1985

Kucera International
Willoughby, Ohio
www.kucerainternational.com
Member Since: 1/1992

L3Harris Technologies
Broomfield, Colorado
www.l3harris.com
Member Since: 6/2008

Merrick & Company
Greenwood Village, Colorado
www.merrick.com
Member Since: 4/1995

Miller Creek Associates
SeaTac Washington
www.mcamaps.com
Member Since: 12/2014

Nearmap
South Jordan, Utah
www.nearmap.com
Member Since: 6/2023

NV5 Geospatial
Sheboygan Falls, Wisconsin
www.quantumspatial.com
Member Since: 1/1974

Pickett and Associates, Inc.
Bartow, Florida
www.pickettusa.com
Member Since: 4/2007

PixElement
Belmont, Michigan
https://pixelement.com
Member Since: 2/2017

Riegl USA, Inc.
Orlando, Florida
www.rieglusa.com
Member Since: 11/2004

Robinson Aerial Surveys, Inc.(RAS)
Hackettstown, New Jersey
www.robinsonaerial.com
Member Since: 1/1954

Sanborn Map Company
Colorado Springs, Colorado
www.sanborn.com
Member Since: 10/1984

Surdex Corporation
Chesterfield, Missouri
www.surdex.com
Member Since: 12/2011

Surveying And Mapping, LLC (SAM)
Austin, Texas
www.sam.biz
Member Since: 12/2005

T3 Global Strategies, Inc.
Bridgeville, Pennsylvania
https://t3gs.com/
Member Since: 6/2020

Towill, Inc.
San Francisco, California
www.towill.com
Member Since: 1/1952

Woolpert LLP
Dayton, Ohio
www.woolpert.com
Member Since: 1/1985

SUSTAININGMEMBER**BENEFITS**

Membership

- ✓ Provides a means for dissemination of new information
- ✓ Encourages an exchange of ideas and communication
- ✓ Offers prime exposure for companies

Benefits of an ASPRS Membership

- Complimentary and discounted Employee Membership*
- E-mail blast to full ASPRS membership*
- Professional Certification Application fee discount for any employee
- Member price for ASPRS publications
- Discount on group registration to ASPRS virtual conferences
- Sustaining Member company listing in ASPRS directory/website
- Hot link to company website from Sustaining Member company listing page on ASPRS website
- Press Release Priority Listing in *PE&RS* Industry News
- Priority publishing of Highlight Articles in *PE&RS* plus, 20% discount off cover fee
- Discount on *PE&RS* advertising
- Exhibit discounts at ASPRS sponsored conferences (exception ASPRS/ILMF)
- Free training webinar registrations per year*
- Discount on additional training webinar registrations for employees
- Discount for each new SMC member brought on board (Discount for first year only)

*quantity depends on membership level

WHO'S WHO IN ASPRS

Founded in 1934, the American Society for Photogrammetry and Remote Sensing (ASPRS) is a scientific association serving thousands of professional members around the world. Our mission is to advance knowledge and improve understanding of mapping sciences to promote the responsible applications of photogrammetry, remote sensing, geographic information systems (GIS) and supporting technologies.

BOARD OF DIRECTORS

BOARD OFFICERS

President
Lorraine B. Amenda, PLS, CP
Towill, Inc

President-Elect
Bandana Kar
Oak Ridge National Lab

Vice President
Amr Abd-Elrahman
University of Florida

Past President
Christopher Parrish, Ph.D
Oregon State University

Treasurer
John McCombs
NOAA

Secretary
Harold Rempel
ESP Associates, Inc.

COUNCIL OFFICERS

ASPRS has six councils. To learn more, visit https://www.asprs.org/Councils.html.

Sustaining Members Council
Chair: Ryan Bowe
Deputy Chair: Melissa Martin

Technical Division Directors Council
Chair: Hope Morgan
Deputy Chair:

Standing Committee Chairs Council
Chair:
Deputy Chair:

Early-Career Professionals Council
Chair: Youssef Kaddoura
Deputy Chair:

Region Officers Council
Chair: Demetrio Zourarakis
Deputy Chair: Jason Krueger

Student Advisory Council
Chair: Oscar Duran
Deputy Chair:

TECHNICAL DIVISION OFFICERS

ASPRS has seven professional divisions. To learn more, visit https://www.asprs.org/Divisions.html.

Geographic Information Systems Division
Director: Denise Theunissen
Assistant Director: Jin Lee

Lidar Division
Director: Ajit Sampath
Assistant Director: Mat Bethel

Photogrammetric Applications Division
Director: Ben Wilkinson
Assistant Director: Hank Theiss

Primary Data Acquisition Division
Director: Srini Dharmapuri
Assistant Director: Ravi Soneja

Professional Practice Division
Director: Hope Morgan
Assistant Director: Matt Elious

Remote Sensing Applications Division
Director: Tao Liu
Assistant Director: Indu Jeyachandran

Unmanned Autonomous Systems (UAS)
Director: Jacob Lopez
Assistant Director: Bahram Salehi

REGION PRESIDENTS

ASPRS has 13 regions to serve the United States. To learn more, visit https://www.asprs.org/regions.html.

Alaska Region

Cascadia Region
Jimmy Schulz

Eastern Great Lakes Region
Craig Fry

Florida Region
Matt LaLuzerne

Gulf South
Cody Condron

Heartland Region
Whit Lynn

Mid-South Region
David Hughes

North Atlantic Region
Kurt Lutz

Northeast Region

Pacific Southwest Region
Omar Mora

Potomac Region
Jason Brown

Rocky Mountain Region
Trent Casi

Western Great Lakes Region
Adam Smith

Classifying Building Roof Damage Using High Resolution Imagery for Disaster Recovery

Elaina Gonsoroski, Yoonjung Ahn, Emily W. Harville, Nathaniel Countess, Maureen Y. Lichtveld, Ke Pan, Leslie Beitsch, Samendra P. Sherchan, and Christopher K. Uejio

Abstract

Post-hurricane damage assessments are often costly and time-consuming. Remotely sensed data provides a complementary method of data collection that can be completed comparatively quickly and at relatively low cost. This study focuses on 15 Florida counties impacted by Hurricane Michael (2018), which had category 5 strength winds at landfall. The present study evaluates the ability of aerial imagery collected to cost-effectively measure blue tarps on buildings for disaster impact and recovery. A support vector machine model classified blue tarp, and parcels received a damage indicator based on the model's prediction. The model had an overall accuracy of 85.3% with a sensitivity of 74% and a specificity of 96.7%. The model results indicated approximately 7% of all parcels (27 926 residential and 4431 commercial parcels) in the study area as having blue tarp present. The study results may benefit jurisdictions that lacked financial resources to conduct on-the-ground damage assessments.

Introduction

In the United States, hurricanes cause substantial economic damage and are responsible for nearly 7000 deaths since 1980 (NOAA 2023). In response to hurricanes and other disasters, the Federal Emergency Management Agency (FEMA) provides aid to qualified communities. FEMA's Public Assistance (PA) Program provides grants to governments and nonprofits after disasters to aid community recovery (FEMA 2023). The Individual Assistance (IA) Program is meant to supplement individuals' insurance, providing funds for basic needs and recovery costs (FEMA 2022). IA has been found to be one of the most vital programs for recovery in the immediate aftermath of a disaster (Lamba-Nieves and Santiago-Bartolomei 2022). In addition, FEMA and the Army Corps of Engineers may offer the Blue Roof Operation after a disaster. The goal of this collaboration is to install blue tarpaulin (tarp) at no-cost on roofs of eligible homes to temporarily prevent further damage of homes until permanent repairs can be completed (FEMA 2017). While they are meant to be short-term solutions, blue tarps have been observed for years after an event (Rowan and Kwiatkowski 2020).

Elaina Gonsoroski, Nathaniel Countess, and Christopher K. Uejio are with the Department of Geography, College of Social Sciences and Public Policy, Florida State University, Tallahassee, FL 32306.

Yoonjung Ahn is with the Institute of Behavioral Science, University of Colorado, Boulder, CO 80309.

Emily W. Harville, Ke Pan, and Samendra P. Sherchan are with the Department of Epidemiology, School of Public Health and Tropical Medicine, Tulane University, New Orleans, LA 70112.

Maureen Y. Lichtveld is with the Department of Environmental and Occupational Health, School of Public Health, University of Pittsburgh, Pittsburgh, PA, 15261.

Leslie Beitsch is with the Department of Behavioral Sciences and Social Medicine, College of Medicine, Florida State University, Tallahassee, FL 32306.

Corresponding author: Elaina Gonsoroski (edg17@fsu.edu)

Contributed by Prasad S. Thenkabail, August 1, 2022 (sent for review November 29, 2022; reviewed by Junhak Lee, Tianqi Zhang).

Although tarps will not be used for severely damaged buildings, the presence of blue tarps still gives insight into how much damage communities experienced and how they are recovering (Miller *et al.* 2013; Miura *et al.* 2020; Naito *et al.* 2020; Rathfon *et al.* 2012).

The present study has two main objectives. First, we seek to quantify the number of parcels with blue tarp present in counties designated by FEMA for individual and public assistance (Area A) versus just public assistance (Area B) after Hurricane Michael (October 2018). Unlike previous work, the current study seeks to classify damage over a large geographical area, including severely and relatively minimally affected counties. We investigated whether accurate results could be obtained across diverse environments. Blue tarps are an indicator of post-hurricane destruction that are also relatively spectrally distinguishable from other infrastructure (Rathfon *et al.* 2012; Miura *et al.* 2020). Second, while multiple short- and medium-term recovery programs are based on county-level damage assessments, few studies have actually quantified the number of buildings impacted by severe conditions within all disaster affected counties (Gurley and Masters 2011; Walker 2011; Tomiczek *et al.* 2014). We determined whether there are small pockets of damage to households outside of counties eligible for IA. The results of the study provide a finer scale to evaluate damage and quantify how many households may be missed when relying on county-level damage assessments.

High-resolution remotely sensed data is capable of identifying blue tarps over the entire affected area. Ground-based damage surveys are accurate and reliable but frequently focus on a specific municipality with a limited sample size (Gurley and Masters 2011). Furthermore, many communities lack the resources needed to even conduct such surveys (FEMA 2016). Alternatively, remotely sensed data collection can aid in disaster response (e.g., routing relief supplies) and recovery efforts. Such data can assess damage over a wide area relatively quickly and cost-effectively when compared to ground-based surveys (Jiang and Friedland 2016). For this study, we used high spatial resolution (<0.5 ft2) optical imagery to detect blue tarps as indicators of small areas of damage after Hurricane Michael. While high-resolution imagery provides superior ability to detect small areas of damage, it has drawbacks in terms of the data size and expertise needed to use the data (e.g., access and skill to use high-performance computing clusters) (Sun *et al.* 2020).

High-performance computing has contributed to a growing body of work using machine learning and deep learning methods to classify imagery and study disaster impacts. One such method includes the support vector machine (SVM) classifier. SVMs have been applied to assess disaster damage and recovery with comparable results to deep learning methods such as convolutional neural networks (CNNs) (Hasan *et al.* 2019). Using SVM, researchers have accurately identified collapsed buildings after disasters demonstrating the method's suitability in urban and rural contexts (Moya *et al.* 2018; Sheykhmousa *et al.* 2019). CNNs have produced highly accurate results, as well detecting different levels of damage (none, minor, major, and destroyed) with improvement over an SVM in Bay County, Florida and portions of its neighboring counties after Hurricane Michael (Berezina and Liu 2022). However, this study

Photogrammetric Engineering & Remote Sensing
Vol. 89, No. 7, July 2023, pp. 437–443.
0099-1112/22/437–443

doi: 10.14358/PERS.22-00106R2

chose an SVM over deep learning methods since it is relatively accurate with smaller training data and shallow data structures (Wang *et al.* 2021). We relied on publicly available optical imagery with only three bands to detect blue tarps after Hurricane Michael.

The results of the classification were used to determine whether blue tarps were located in counties ineligible for IA. In response to environmental disasters such as hurricanes, governors of affected states can request a Major Disaster Declaration based on a variety of factors, including damage severity and state funds available. If accepted, federal programs including IA, PA, and/or Hazard Mitigation Assistance may be available based on the request and preliminary damage assessments (FEMA 2022). Recent evidence has shown that certain vulnerable populations are more likely to be denied aid even if located in an eligible area (García 2022; Lamba-Nieves and Santiago-Bartolomei 2022). After Hurricane Maria struck Puerto Rico in 2017, large numbers of homeowners were denied aid for reasons such as being unable to prove homeownership and scheduling inspections (García 2022). In addition, areas with higher populations of foreign-born individuals were found to have lower damage estimates and therefore less aid (Grube *et al.* 2018). However, when looking at social vulnerability factors and damage at the county level, damage severity is still the largest predictor of IA aid (Emrich *et al.* 2022). This is expected and gives credibility to the way the program is operating, but county-level assessments still leave opportunity for households to be missed.

Methods

Study Area and Event

Hurricane Michael made landfall in Bay County, Florida on October 10, 2018. The storm contributed to 45 fatalities and over $25 billion in damages (NOAA 2023). Power outages spanned six US states and included 1.7 million customers (Woodward and Marcy 2018). The hurricane was the strongest on record to hit the Florida panhandle and, as a result, federal disasters were declared for counties across the area. This study covered 15 of those counties located in the Florida panhandle: Bay, Calhoun, Franklin, Gadsden, Gulf, Hamilton, Holmes, Jackson, Jefferson, Liberty, Madison, Taylor, Wakulla, Walton, and Washington. These counties generally had higher rates of poverty (12.2–29.9%) and populations without health insurance coverage (8.9–18.3%) than national rates (11.8% and 8.8%, respectively). In addition, these counties had lower rates of employment than the national average as well as lower average educational attainment (US Census Bureau 2018). For the purpose of quantifying damage at a building level, we relied on parcel data. Parcels are legally owned areas of land with a defined location, boundary, and a specific type of usage or development designation. In total, the data included 461 106 parcels located within the study area. Of this total, 101 596 of the parcels were commercial, with the remaining 359 510 parcels (78%) classified as residential. FEMA designated these 15 counties eligible for assistance following Hurricane Michael. The most severely impacted counties qualified for IA and PA from FEMA. These included Bay, Calhoun, Franklin, Gadsden, Gulf, Holmes, Jackson, Liberty, Taylor, Wakulla, and Washington counties. The remaining four counties qualified for PA alone (Figure 1) (FEMA 2018).

Data Sources

The post-Hurricane Michael imagery used in this study were sourced from aerial photographs taken through the Florida Department of Revenue and stored in the Florida Department of Environmental Protection's Land Boundary Information System (LABINS) (LABINS 2019). The images were captured between December 2018 and February 2019, and have 0.5-foot spatial resolution with red, green, and blue spectral bands. Each image tile covers one square mile and in total the data required 5 terabytes of storage.

Parcel Data

Parcel data were sourced from the University of Florida's GeoPlan Center and contain the Florida Department of Revenue's tax roll information from 2018 (FGDL 2019). In addition to information about the property (e.g., year the structure was built, value, use), these data contain spatial polygon information. When matched by location in a Geographic Information Systems software, these data can be used to determine how many households had blue tarps present within the study area. These parcel data are publicly available.

Image Classification

The study area includes a variety of landcover types. However, the class of interest only included blue tarps to indicate whether a structure was damaged or not. Therefore, the final classification result was obtained through two steps: first, a multi-class classification and second, a binary classification distinguishing blue tarps from all other classes. The multi-class schema contained seven training classes: *Blue Tarp, Pool Water, Impervious Surface, Vegetation, Bare Soil, Roof,* and *Large Waterbody*. These training classes are created by taking samples of pixels belonging to these different classes from different areas in the image. Researchers then created a signature file in ESRI ArcMap software using these training samples. We manually entered the mean values from the signature file to train the "Train Support Vector Machine (SVM) Classifier" in Python 3 using the scikit-learn package (Pedregosa *et al.* 2011). SVM classifiers distinguish classes by creating a linear hyperplane to separate the data. While SVM was originally used for binary classifications, the Support Vector Classification tool in scikit-learn implements a "one-versus-one" approach for multi-class problems. This approach reduces the problem to a collection of binary problems

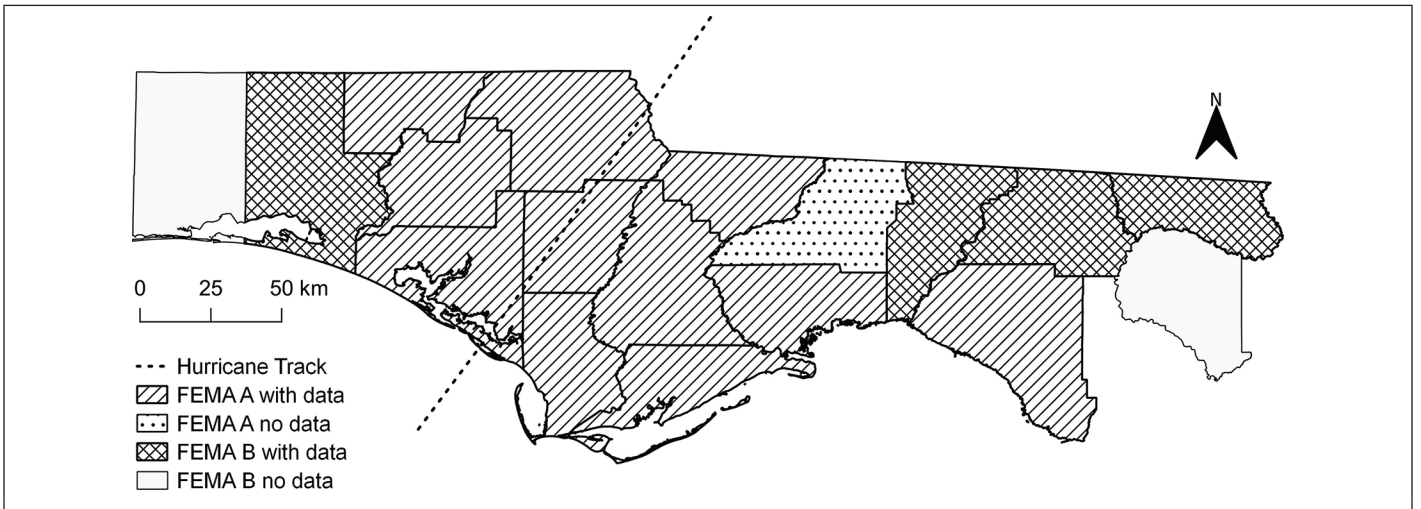

Figure 1. Map of the Florida panhandle showing counties that were affected by Hurricane Michael. Federal Emergency Management Agency (FEMA) A indicates a county was eligible for both individual and public assistance. FEMA B counties were only eligible for public assistance.

(Foody *et al.* 2006). SVM models are commonly applied to classification problems and perform relatively well compared to other deep learning methods even with limited training samples (Jozdani *et al.* 2019).

Batch processing tools were required to not only classify the aerial photographs (raster tiles), but also to convert the output into vector data for intersection with parcel information. A scripted batch code handled data classification and processing. The Rasterio package (GitHub 2019) read in the imagery as three-dimensional Numpy arrays (Harris *et al.* 2020). Each image was flattened to a two-dimensional array and run through the SVM classifier. The results were recoded to a binary classification (tarp or not tarp) and then converted to polygons using the Fiona package (GitHub 2019) to compare to the parcel information. We separately assessed the accuracy of the 1) multispectral classification and 2) multispectral classification with a spatial filter which excluded tarp polygons less than 200 square feet to reduce noise in the classification. Sensitivity testing filtering smaller polygons (50 and 100 square feet) did not reduce the noise while removing areas larger than 200 feet resulted in more false negatives and reduced the overall accuracy.

The accuracy assessments were based on a separate validation sample of 300 randomly positioned points (150 points per class). The points were placed within parcels with a minimum of 328 feet (100 meters) between points. Each point was manually checked for correct classification by looking for the presence or absence of visible blue tarps within a parcel in the aerial imagery. Researchers then calculated the overall and target class accuracies for the multispectral classification and multispectral classification with a spatial filter.

Results

The results of the classification accuracy assessment are reported in a confusion matrix (Table 1). The accuracy assessment was conducted for both the spatially filtered and unfiltered results. Before the application of the spatial filter, the overall accuracy was 78%. The final filtered results indicated an overall accuracy of 85.3% with a kappa coefficient of approximately 0.71, indicating an improvement over the result that was not filtered. The user's accuracies of the blue tarp class and non-tarp class in the filtered result were 95.7% and 78.8%, and producer's accuracies were 74% and 96.7%, respectively. Pools and roofs, which were highly reflective, were more commonly confused with blue tarp than impervious surfaces, vegetation, or darker roofs. The spatial filter by polygon area improved the specificity of the tarp classification from 82% to 96.7%.

The presence of any blue tarps indicated whether a parcel had been damaged by the hurricane and received a damage designation in the classification (Figure 2). Within the study area, blue tarps were located in approximately 7% of all parcels (27 926 residential and 4431 commercial). Examining just residential parcels by county, results showed Calhoun County had the largest proportion of all parcels with blue tarps at approximately 22.6%, followed by Bay County at 20.5% and Jackson and Gulf Counties at 16.9% and 13.9%, respectively (Table 2). In general, the counties in Area B including Hamilton, Jefferson, Madison, and Walton had relatively lower percentages of parcels (0.3–2.9%) with tarps, which is in agreement with the FEMA aid classification. These counties were all located farther from the hurricane track (Figure 3).

Discussion

Main Findings

The results of this study demonstrated that we could determine individual building damage across a large disaster-affected area at relatively low cost and time. Other studies using various methods, including CNNs and combinations of remote sensing and survey data, have resulted in higher accuracies. However, these studies generally focused on a smaller area or on just one or more urban centers (Berezina and Liu 2022; Gurley and Masters 2011; Miura *et al.* 2020; Naito *et al.* 2020). However, the present study covered a much wider geographical area with more variability in environment (urban versus rural, coastal versus inland) and included photographs taken on different days, which may result in differences in reflectance of blue tarps. Despite these challenges, the SVM model used still resulted in an acceptable accuracy (85.3%) when identifying buildings that had blue tarps present on their roofs. Common confusion with the blue tarp class included high reflectance surfaces (e.g., metal roofs) and pools. Further refinement of the model could improve the accuracy and the introduction of other machine learning and/or object oriented classification methods may allow for detection of damage beyond tarps (Miura *et al.* 2020).

Filtering polygons by removing those with an area under 200 square feet did successfully reduce the noise in the model output. Researchers compared the accuracy between the spatially filtered and unfiltered results using the same methodology. The spatial filter improved the overall accuracy by approximately 7% and had a large impact on improving the model specificity. Previous studies have used object size to reduce classification errors (Jiménez-Jiménez *et al.* 2020; Palmer *et al.* 2018). Similar to the current study, these studies reduced

Table 1. Two class accuracy assessment of 300 independent and randomly distributed points. The spatially filtered results (bottom) show improvement in the overall accuracy and specificity over the unfiltered results (top).

Unfiltered				
Class	**Tarp**	**Other**	**Total**	**User's Accuracy:**
Tarp	111	27	138	80.4%
Other	39	123	162	75.9%
Total	150	150	300	
Producer's Accuracy:	74%	82%		Overall Accuracy: 78%
Spatially Filtered				
Class	**Tarp**	**Other**	**Total**	**User's Accuracy:**
Tarp	111	5	116	95.7%
Other	39	145	184	78.8%
Total	150	150	300	
Producer's Accuracy:	74%	96.7%		Overall Accuracy: 85.3%

Table 2. The proportion of residential parcels in each county where the model detected blue tarps as a percentage of all residential parcels within that county.

County	**Parcels with Tarps (%)**
Area A	
Bay	20.5
Calhoun	22.6
Franklin	3.5
Gadsden	7.0
Gulf	13.9
Holmes	4.8
Jackson	16.9
Liberty	9.3
Taylor	1.2
Wakulla	1.1
Washington	7.3
Area B	
Hamilton	0.7
Jefferson	0.9
Madison	0.8
Walton	3.5

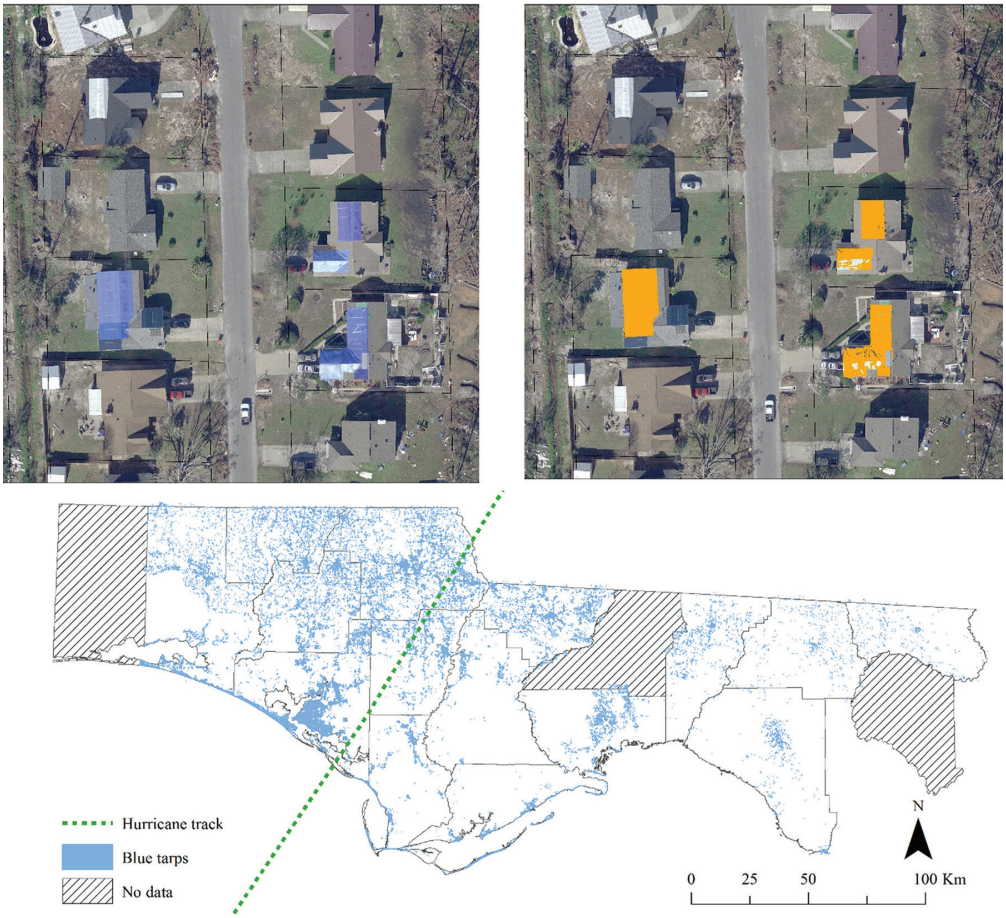

Figure 2. The unaltered aerial photograph is shown (top left) followed by the results of the classification overlayed in orange (top right). The model classified tarps in all counties which had imagery available and were disaster designated by Federal Emergency Management Agency (FEMA) (bottom).

Figure 3. The map shows the percentage of residential parcels with tarps by county with high proportions located in counties nearer to the hurricane track.

noise by eliminating areas too small to be the roof in a primary structure. The improvement indicates the filter was appropriate for reducing the number of false positives in the final model results.

In addition, our results did indicate that some damaged homes were located in counties not eligible for individual assistance from FEMA. While the proportion was small (0.3–2.9%), the results still suggest there are households with damaged structures located in areas ineligible for assistance. To further investigate the pre-hurricane blue tarp prevalence, we counted the number of blue tarps present in Bay (FEMA A) and Jefferson (FEMA B) counties using data from the National Agriculture Imagery Program (NAIP). The NAIP images were collected in 2017 for Florida, approximately one year before the hurricane. The results showed low percentages of tarp in Bay (0.07%) and Jefferson (0.02%) counties, which are significantly less than after the hurricane (Bay 20.5% and Jefferson 0.9%). These findings show that while there may be blue tarps present before the storm, it is likely most were installed post-storm. In addition, the results provide evidence that there are areas in FEMA B that sustained damage. Media reports suggest that FEMA may be more likely to deny aid requests in rural areas struck by local disasters. Yet, aid is approved in statewide disasters, even if the damage they cause is less severe (Harris and Eaton 2022). This study provides an objective way for FEMA to target IA to sub-county areas that suffered infrastructure damage. If there is no state aid available, homeowners have few ways to seek financial aid.

Furthermore, there is evidence that communities that were economically disadvantaged and/or hosted a higher proportion of people of color were more likely to have aid requests rejected, which further compounds existing inequalities (Grube *et al.* 2018; Domingue and Emrich 2019). Previous studies have found evidence of pre-storm inequalities in that racial/ethnic minorities and populations with lower socioeconomic status are more exposed to inland flooding (Collins *et al.* 2019). Furthermore, these same populations are often living in areas with more poorly maintained infrastructure, older housing that may be built to less stringent building code requirements, and face lengthier recovery times (Peacock 2014; Wyczalkowski *et al.* 2019). Future work monitoring damage at the household level may provide further insight into inequities in storm damage and recovery and the impacts living in more severely damaged areas may have on health (Pan *et al.* 2021).

Blue tarps are distributed to qualified homeowners to provide temporary covering, protecting structures from further damage while repairs are being made. While the tarps are only meant to last a few months, studies have found the coverings are present from two to three months to over two years after a disaster (Rathfon *et al.* 2012; Rowan and Kwiatkowski 2020). There are various reasons why individuals are unable to repair their homes within the timeframe blue tarps are designed to last and for the most part, the most vulnerable face the greatest challenges. For example, although federal aid is available, it may be denied for failure to prove home ownership or issues during the home inspection process. In addition, even if approved for funds, in some cases the monetary amount can be insufficient to repair the home (García 2022). Failure to repair or have the home covered in the interim can result in further damage to the home (Allen 2007).

The study results have implications for health and indoor environments and methods can be applied for investigating these environments after disasters. Unsafe housing has a number of negative implications, including towards human health such as exposure to mold, mental health impacts, and chemical exposure. Studies conducted after Hurricane Katrina have examined the effects of dampness in the home on human health. Researchers found respiratory symptoms were associated with exposure to water damaged homes during clean-up activities in New Orleans following Katrina (Chulada *et al.* 2012; Cummings *et al.* 2008; Grimsley *et al.* 2012; Mitchell *et al.* 2012). In addition, flooding from hurricanes and debris removal can expose residents to harmful chemicals. After Hurricane Katrina residents were concerned about chemical exposures in air, soil, and water (Picou 2009). Lastly, studies have consistently found worsened mental health associated with disasters (Goldmann and Galea 2014). Although these health effects are linked to direct exposures such as injury, the long-term impacts of the disaster, such as loss of property, can lead to high levels of stress. Prolonged stress is associated with some of the most common mental health conditions after disasters, including posttraumatic stress disorder and major depressive disorder (Foa *et al.* 2006; Nillni *et al.* 2013; North and Baron 2021). Therefore, alleviating the stress associated with damaged housing has implications for improving mental health.

Limitations

This study has some limitations. First, we did not account for blue tarps in the entire study area that may have been present before Hurricane Michael struck Florida. However, we did provide estimates in two counties using NAIP imagery taken before the hurricane. Second, the images used to classify blue tarps were taken between two and four months after the hurricane made landfall. Some homes may have been repaired within this timeframe. In addition, for blue tarps to be installed by the Army Corps of Engineers, the roof must have less than 50% structural damage (FEMA 2017). Therefore, any residences too heavily damaged to install blue tarps are not considered through this classification. Third, blue tarps not located on roofs (e.g., blue tarps used to cover sheds or vehicles) would also be identified by the model. These tarps were largely excluded by the spatial filter that removed any areas under 200 square feet. Additionally, by limiting the analysis to occupied residential parcels, we excluded parcel land use codes without homes such as common areas and vacant residential properties. While we excluded these properties in an effort to limit inclusion of non-residences, it is difficult to distinguish multi-building damage within a parcel; for instance, if the non-primary structure on the property was damaged. Object-based classifiers may improve the accuracy of detecting blue tarp and other forms of roof damage.

Lastly, the study results did not include the severity of the damage. With building footprint data, it may be possible to provide the proportion of the damage for each structure. However, by relying on blue tarp presence alone, it is not possible to assess the severity of damage. Instead, blue tarp presence provides a practical assessment of damage to help frontline responders direct resources efficiently and effectively. Introducing a CNN and additional data (e.g., building footprints) may improve the accuracy as well as provide additional information about the damage sustained (Berezina and Liu 2022). CNN could also make use of spatial information and account for information in nearby pixels (Hasan *et al.* 2019). In addition, using image segmentation methods may help to improve the accuracy of the classification particularly when using such high-resolution data. Deep learning methods that can make use of the rich spatial information in the data may improve the accuracy of the model and eliminate some of the class confusion (e.g., confusion between blue tarps and pools) (Qi *et al.* 2020).

Conclusion

This study presents evidence that high resolution imagery provides a feasible method to detect post-disaster damage and recovery. Remotely sensed imagery has the advantage of being able to cover a wide area relatively quickly at relatively low cost compared to ground surveys. However, computing abilities and storage may limit the applicability of high-resolution data. Spatially filtering the model output improved the overall model accuracy and specificity. While this study focused on identifying blue tarps in counties affected by Hurricane Michael, future studies could expand this methodology to include more frequent data collection and deep learning methods to detect roof damage more generally and track recovery over time. Detection of damage in areas outside of those eligible for individual assistance also has the potential to provide further evidence of inequitable aid distribution. Safe housing is a basic need for disaster survivors and denying or providing inadequate aid has long-term implications for community resilience and recovery (He *et al.* 2021; Lichtveld *et al.* 2020; Shultz and Galea 2017). Remote sensing provides a means to assess damage quickly and monitor recovery in the months after a disaster to understand where disaster effects persist.

Acknowledgments

Research reported in this publication was supported by National Institute of Environmental Health Sciences (NIEHS) of the National Institutes of Health under award number R21ES031020. The content is solely the responsibility of the authors and does not necessarily represent the official views of the National Institutes of Health. The computing for this project was performed on the HPC at the Research Computing Center at the Florida State University (FSU).

References

Allen, B. L. 2007. Environmental justice, local knowledge, and after-disaster planning in New Orleans. *Technology in Society* 29:153–159.

Berezina, P. and D. Liu. 2022. Hurricane damage assessment using coupled convolutional neural networks: A case study of hurricane Michael. *Geomatics, Natural Hazards and Risk* 13(1):414–431.

Chulada, P. C., S. Kennedy, M. M. Mvula, K. Jaffee, J. Wildfire, E. Thornton, R. D. Cohn, L. F. Grimsley, H. Mitchell, J. El-Dahr, Y. Sterling, W. J. Martin, L. White, K. U. Stephens and M. Lichtveld. 2012. The Head-off environmental asthma in Louisiana (HEAL) study—Methods and study population. *Environmental Health Perspectives* 120(11):1592–1599.

Collins, T. W., S. E. Grineski, J. Chakraborty and A. B. Flores. 2019. Environmental injustice and Hurricane Harvey: A household-level study of socially disparate flood exposures in Greater Houston, Texas, USA. *Environmental Research* 179:108772.

Cummings, K. J., J. Cox-Ganser, M. A. Riggs, N. Edwards, G. R. Hobbs and K. Kreiss. 2008. Health effects of exposure to water-damaged New Orleans homes six months after Hurricanes Katrina and Rita. *American Journal of Public Health* 98(5):869–875.

Domingue, S. J. and C. T. Emrich. 2019. Social vulnerability and procedural equity: Exploring the distribution of disaster aid across counties in the United States. *The American Review of Public Administration* 49(8):897–913.

Emrich, C. T., S. K. Aksha and Y. Zhou. 2022. Assessing distributive inequities in FEMA's disaster recovery assistance fund allocation. *International Journal of Disaster Risk Reduction* 74:102855.

Federal Emergency Management Agency (FEMA). 2016. *Damage Assessment Operations Manual*. 460. <https://www.fema.gov/media-library-data/1558541566358-30e29cac50605aae39af77f7e25a3ff0/Damage_Assessment_Manual_4-5-2016.pdf> Accessed 14 February 2022.

Federal Emergency Management Agency (FEMA). 2017. *Frequently Asked Questions About Operation Blue Roof [R4 DR-4337-FL FS 001]*. <https://www.fema.gov/news-release/20200220/haeufig-gestellte-fragen-operation-blue-roof> Accessed 20 January 2023.

Federal Emergency Management Agency (FEMA). 2018. *Designated Areas: Disaster 4399*.

https://www.fema.gov/disaster/4399/designated-areas Accessed 13 March 2023.

Federal Emergency Management Agency (FEMA). 2022. *Individual Assistance*. <https://www.fema.gov/assistance/individual> Accessed 31 January 2023.

Federal Emergency Management Agency (FEMA). 2023. *Assistance for Governments and Private Non-Profits After a Disaster*. <https://www.fema.gov/assistance/public> Accessed 31 January 2023.

Florida Geographic Data Library (FGDL). 2019. *FGDL Metadata Explorer. University of Florida's GeoPlan Center*. <https://www.fgdl.org/metadataexplorer/explorer.jsp> Accessed 20 January 2023.

Foa, E. B., D. J. Stein and A. C. McFarlane. 2006. Symptomatology and psychopathology of mental health problems after disaster. *Journal of Clinical Psychiatry* 67(SUPPL. 2):15–25.

Foody, G. M., A. Mathur, C. Sanchez-Hernandez and D. S. Boyd. 2006. Training set size requirements for the classification of a specific class. *Remote Sensing of Environment* 104(1):1–14.

García, I. 2022. Deemed ineligible: Reasons homeowners in Puerto Rico were denied aid after Hurricane María. *Housing Policy Debate* 32(1):14–34.

GitHub. 2019. Rasterio: Geospatial Raster I/O for {Python} Programmers. *GitHub*. <https://github.com/rasterio/rasterio> Accessed 13 March 2023.:

Goldmann, E. and S. Galea. 2014. Mental health consequences of disasters. *Annual Review of Public Health* 35:169–183.

Grimsley, L. F., P. C. Chulada, S. Kennedy, L. A. White, J. Wildfire, R. D. Cohn, H. Mithcell, E. Thornton, J. El-Dahr, M. M. Mvula, Y. Sterling, W. J. Martin, K. U. Stephens and M. Lichtveld. 2012. Indoor environmental exposures for children with asthma enrolled in the HEAL study, post-Katrina New Orleans. *Environmental Health Perspectives* 120(11):1600–1606.

Grube, L. E., R. Fike and V. H. Storr. 2018. Navigating disaster: An empirical study of federal assistance following Hurricane Sandy. *Eastern Economic Journal* 44(4):576–593.

Gurley, K. R. and F. J. Masters. 2011. Post-2004 hurricane field survey of residential building performance. *Natural Hazards Review* 12(4):177–183.

Harris, B. and J. Eaton. 2022. 'They don't offer anything': Disaster survivors left behind when FEMA, states don't help. *NBC News*. <https://www.nbcnews.com/news/us-news/fema-individual-assistance-disaster-survivors-rcna19495> Accessed 20 January 2023.

Harris, C. R., K. J. Millman, S. J. van der Walt, R. Gommers, P. Virtanen, D. Cournapeau, E. Wieser, J. Taylor, S. Berg, N. J. Smith, R. Kern, M. Picus, S. Hoyer, M. H. van Kerkwijk, M. Brett, A. Haldane, J. Fernández del Río, M. Wiebe, P. Peterson, P. Gérard-Marchant, K. Sheppard, T. Reddy, W. Weckesser, H. Abbasi, C. Gohlke and T. E. Oliphant. 2020. Array programming with NumPy. *Nature* 585:357–362.

Hasan, H., H.Z.M. Shafri and M. Habshi. 2019. A comparison between support vector machine (SVM) and convolutional neural network (CNN) models for hyperspectral image classification. *IOP Conference Series: Earth and Environmental Science* 357(1):0–10.

He, Y., B. Wu, P. He, W. Gu and B. Liu. 2021. Wind disasters adaptation in cities in a changing climate: A systematic review. *PloS One* 16(3):e0248503.

Jiang, S. and C. J. Friedland. 2016. Automatic urban debris zone extraction from post-hurricane very high-resolution satellite and aerial imagery. *Geomatics, Natural Hazards and Risk* 7(3):933–952.

Jiménez-Jiménez, S. I., W. Ojeda-Bustamante, R. E. Ontiveros-Capurata and M. de J. Marcial-Pablo. 2020. Rapid urban flood damage assessment using high resolution remote sensing data and an object-based approach. *Geomatics, Natural Hazards and Risk* 11(1):906–927.

Jozdani, S. E., B. A. Johnson and D. Chen. 2019. Comparing deep neural networks, ensemble classifiers, and support vector machine algorithms for object-based urban land use/land cover classification. *Remote Sensing* 11(14):1713.

Lamba-Nieves, D. and R. Santiago-Bartolomei. 2022. Who gets emergency housing relief? An analysis of FEMA individual assistance data after Hurricane María. *Housing Policy Debate*:1–21.

Land Boundary Information System (LABINS). 2019. *Survey Data for Florida, Aerial Images*. Florida Department of Environmental Protection. <https://www.labins.org/mapping_data/aerials/aerials.cfm> Accessed 8 November 2020.

Lichtveld, M., H. Covert, J. El-Dahr, L. F. Grimsley, R. Cohn, C. H. Watson, E. Thornton and S. Kennedy. 2020. A community-based participatory research approach to Hurricane Katrina: When disasters, environmental health threats, and disparities collide. *American Journal of Public Health* 110(10):1485–1489.

Miller, C., M. Gibbons, K. Beatty and A. Boissonnade. 2013. Topographic speed-up effects and observed roof damage on Bermuda following Hurricane Fabian (2003). *Weather and Forecasting* 28(1):159–174.

Mitchell, H., R. D. Cohn, J. Wildfire, E. Thornton, S. Kennedy, J. M. El-Dahr, P.C. Chulada, M.M. Mvula, L. F. Grimsley, M. Y. Lichtveld, L. E. White, Y. M. Sterling, K. U. Stephens and W. J. Martin. 2012. Implementation of evidence-based asthma interventions in post-Katrina New Orleans: The head-off environmental asthma in Louisiana (HEAL) Study. *Environmental Health Perspectives* 120(11):1607–1612.

Miura, H., T. Aridome and M. Matsuoka. 2020. Deep learning-based identification of collapsed, non-collapsed and blue tarp-covered buildings from post-disaster aerial images. *Remote Sensing* 12(12):1924.

Moya, L., F. Yamazaki, W. Liu and M. Yamada. 2018. Detection of collapsed buildings from lidar data due to the 2016 Kumamoto earthquake in Japan. *Natural Hazards and Earth System Sciences* 18(1):65–78.

Naito, S., H. Tomozawa, Y. Mori, T. Nagata, N. Monma, H. Nakamura, H. Fujiwara and G. Shoji. 2020. Building-damage detection method based on machine learning utilizing aerial photographs of the Kumamoto earthquake. *Earthquake Spectra* 36(3):1166–1187.

Nillni, Y. I., E. Nosen, P. A. Williams, M. Tracy, S. F. Coffey and S. Galea. 2013. Unique and related predictors of major depressive disorder, posttraumatic stress disorder, and their comorbidity after Hurricane Katrina. *The Journal of Nervous and Mental Disease* 201(10):841–847.

National Oceanic and Atmospheric Administration (NOAA) National Centers for Environmental Information (NCEI). 2023. *U.S. Billion-Dollar Weather and Climate Disasters*. <https://www.ncei.noaa.gov/access/billions/> Accessed 20 January 2023.

North, C. S. and D. Baron. 2021. The symptom structure of postdisaster major depression: convergence of evidence from 11 disaster studies using consistent methods. *Behavioral Sciences* 11(1):8.

Palmer, D., E. Koumpli, I. Cole, R. Gottschalg and T. Betts. 2018. A GIS-based method for identification of wide area rooftop suitability for minimum size PV systems using LiDAR data and photogrammetry. *Energies* 11(12):3506.

Pan, K., L. Beitsch, E. Gonsoroski, S. P. Sherchan, C. K. Uejio, M. Y. Lichtveld and E. W. Harville. 2021. Effects of Hurricane Michael on access to care for pregnant women and associated pregnancy outcomes. *International Journal of Environmental Research and Public Health* 18(2):390.

Peacock, W. G., S. Van Zandt, Y. Zhang and W. E. Highfield. 2014. Inequities in long-term housing recovery after disasters. *Journal of the American Planning Association* 80(4):356–371.

Pedregosa, F., G. Varoquaux, A. Gramfort, V. Michel, B. Thirion, O. Grisel, M. Blondel, P. Prettenhofer, R. Weiss, V. Dubourg, J. Vanderplas, A. Passos, D. Cournapeau, M. Brucher, M. Perrot and E. Duchesnay. 2011. Scikit-learn: Machine Learning in Python. *Journal of Machine Learning Research* 12(85):2825−2830.

Picou, J. S. 2009. Katrina as a Natech disaster: Toxic contamination and long-term risks for residents of New Orleans. *Journal of Applied Social Science* 3(2):39–55.

Qi, X., K. Li, P. Liu, X. Zhou and M. Sun. 2020. Deep attention and multi-scale networks for accurate remote sensing image segmentation. *IEEE Access* 8:146627–146639.

Rathfon, D., R. Davidson, J. Bevington, A. Vicini and A. Hill. 2012. Quantitative assessment of post-disaster housing recovery: A case study of Punta Gorda, Florida, after Hurricane Charley. *Disasters* 37(2):333–355.

Rowan, S. and K. Kwiatkowski. 2020. Assessing the relationship between social vulnerability, social capital, and housing resilience. *Sustainability (Switzerland)* 12(18):7718.

Shultz J. M. and S. Galea. 2017. Mitigating the mental and physical health consequences of Hurricane Harvey. *JAMA* 318(15):1437–1438.

Sheykhmousa, M., N. Kerle, M. Kuffer and S. Ghaffarian. 2019. Post-disaster recovery assessment with machine learning-derived land cover and land use information. *Remote Sensing* 11(10):1174.

Sun, W., P. Bocchini and B. D. Davison. 2020. Applications of artificial intelligence for disaster management. *Natural Hazards* 103:631–2689. https://doi.org/10.1007/s11069-020-04124-3.

Tomiczek, T., A. Kennedy and S. Rogers. 2014. Collapse limit state fragilities of wood-framed residences from storm surge and waves during Hurricane Ike. *Journal of Waterway, Port, Coastal, and Ocean Engineering* 140(1):43–55.

US Census Bureau. 2018. *QuickFacts*. <https://www.census.gov/quickfacts/fact/table/US/PST045221> Accessed 20 January 2023.

Walker, G. R. 2011. Modelling the vulnerability of buildings to wind—A review. *Canadian Journal of Civil Engineering* 38(9):1031–1039.

Wang, P., E. Fan and P. Wang. 2021. Comparative analysis of image classification algorithms based on traditional machine learning and deep learning. *Pattern Recognition Letters* 141(3):61–67.

Woodward, M. and C. Marcy. 2018. *Hurricane Michael Caused 1.7 Million Electricity Outages in the Southeast United States*. U.S. Energy Information Administration. <https://www.eia.gov/todayinenergy/detail.php?id=37332#> Accessed 20 January 2023.

Wyczalkowski, C. K., E. J. van Holm, A. Esnard and B. S. Lai. 2019. Uneven neighborhood recovery: Hurricane damage and neighborhood change in the Houston–Galveston region since 1970. *City & Community* 18(2):689–709.

In-Press Articles

Edge Detection Method for High-Resolution Remote Sensing Imagery by Combining Superpixels with Dual-Threshold Edge Tracking. Yanxiong Liu, Zhipeng Dong, Yikai Feng, Yilan Chen, and Long Yang.

Expansion of Urban Impervious Surfaces in Lahore (1993–2022) Based on GEE and Remote Sensing Data. Muhammad Nasar Ahmad, Zhenfeng Shao, Akib Javed, and Fakhrul Islam.

Small Object Detection in Remote Sensing Images Based on Window Self-Attention Mechanism. Jiaxin Xu, Qiao Zhang, Yu Liu, and Mengting Zheng.

Leveraging NAIP Imagery for Accurate Large-Area Land Use/Land Cover Mapping: A Case Study in Central Texas. Mukti Ram Subedi, Carlos Portillo-Quintero, Samanthaa S. Kahl, Nancy E. McIntyre, Robert D. Cox, and Gad Perry.

Effect of Latitude as a Significant Element on the Results of Direct UTM Coordinates Transformation Method. Mohammed Anwer Jassim and Darin Mohammed Tofiq Mohammed.

CFAR Edge Detection Using Hysteresis Thresholding for Polarimetric SAR Imagery. Chaoyang Niu, Wanjie Lu, Wei Liu, Tao Hu, Shiju Wang, and Yajie Wu.

ASPRS
CODE OF ETHICS

Honesty, justice, and courtesy form a moral philosophy which associated with mutual interest among people should be the principles on which ethics are founded.

Each person who is engaged in the use development and improvement of the mapping sciences (Photogrammetry Remote Sensing Geographic Information Systems and related disciplines) should accept those principles as a set of dynamic guides for conduct and a way of life rather than merely for passive observance. It is an inherent obligation to apply oneself to one's profession with all diligence and in so doing to be guided by this Code of Ethics.

Accordingly, each person in the mapping sciences profession shall have full regard for achieving excellence in the practice of the profession and the essentiality of maintaining the highest standards of ethical conduct in responsibilities and work for an employer all clients colleagues and associates and society at large and shall…

asprs THE IMAGING & GEOSPATIAL INFORMATION SOCIETY

www.asprs.org

1. Be guided in all professional activities by the highest standards and be a faithful trustee or agent in all matters for each client or employer.
2. At all times, function in such a manner as will bring credit and dignity to the mapping sciences profession.
3. Not compete unfairly with anyone who is engaged in the mapping sciences profession by:
   a. Advertising in a self-laudatory manner;
   b. Monetarily exploiting one's own or another's employment position;
   c. Publicly criticizing other persons working in or having an interest in the mapping sciences;
   d. Exercising undue influence or pressure or soliciting favors through offering monetary inducements.
4. Work to strengthen the profession of mapping sciences by:
   a. Personal effort directed toward improving personal skills and knowledge;
   b. Interchange of information and experience with other persons interested in and using a mapping science with other professions and with students and the public;
   c. Seeking to provide opportunities for professional development and advancement of persons working under his or her supervision;
   d. Promoting the principle of appropriate compensation for work done by person in their employ..
5. Undertake only such assignments in the use of mapping sciences for which one is qualified by education training and experience and employ or advise the employment of experts and specialists when and whenever clients' or employers' interests will be best served thereby.
6. Give appropriate credit to other persons and/or firms for their professional contributions.
7. Recognize the proprietary privacy legal and ethical interests and rights of others. This not only refers to the adoption of these principles in the general conduct of business and professional activities but also as they relate specifically to the appropriate and honest application of photogrammetry remote sensing geographic information systems and related spatial technologies. Subscribers to this code shall not condone promote advocate or tolerate any organization's or individual's use of these technologies in a manner that knowingly contributes to:
   a. deception through data alteration;
   b. circumvention of the law;
   c. transgression of reasonable and legitimate expectation of privacy.
8. Promote equity, inclusion and intellectual diversity in the mapping sciences. Encourage participation without regard to race, religion, gender, disability, age, national origin, political affiliation, sexual orientation, gender identity, or gender expression.

Estimation of the Forest Stand Biomass and Greenhouse Gas Emissions Using Lidar Surveys

Rida Sultanova and Radik Mustafin

Abstract

At the research points, the relationship between the Normalized Difference Vegetation and Normalized Green Red Difference indices is characterized by a determination coefficient equal to 0.52. The estimation of the emission of carbon dioxide and nitrogen oxide in the forest air at an altitude of 40 m above the level of the soil cover during the growing season showed differences in their values during the daytime and at night. The results helped determine promising methods of inventory of the carbon landfill forest area for aboveground woody biomass assessment based on data obtained from several sources and land forest estimation research. The research involved: 1) integration of an unmanned aerial vehicle -based digital camera and lidar sensors in order to optimize the efficiency and cost of data collection; 2) taking advantage of high-resolution aerial photographs and sparse lidar point clouds using an information fusion approach and the ability to compensate for their shortcomings.

Introduction

The strategic approach to the use of forests is estimated by its productivity and an increase in the sustainability of forest ecosystems (IUFRO 2020). The problems of urbanized territories, including pollution of the atmosphere, soil, water bodies, increased greenhouse effect, and others, cannot be solved without the participation of forest ecosystems. When forest resources are limited and forest development is intensive, the improvement of forest management methods assumes a greater scientific and economic importance. Climate change, the degradation of the environment with the growth of the world's urban population, and a resource-intensive lifestyle challenges the forest industry to find the most effective methods of forest monitoring. Anthropogenic transformation of natural ecosystems significantly reduces carbon sequestration, leading to the predominance of emission processes over the absorption of greenhouse gases. Natural ecosystems of the Republic of Bashkortostan changed by people occupy the main areas including forests and agricultural lands. Therefore, the main task of managing previously disturbed natural ecosystems involves carbon sequestration during progressive successions.

Aboveground woody biomass (AGB) is one of the major elements of the global carbon cycle (Chan *et al.* 2021; Shoot *et al.* 2021), providing the organic carbon deposition (sequestration and storage). According to the research of Pugh *et al.* (2019), the maximum amount of carbon is concentrated in the aboveground woody biomass of the stand, while the maximal proportion of carbon deposited in the dead soil cover (woody detritus) is 4%. AGB monitoring and mapping allow estimating the carbon budget in forests, which contributes to solving scientific and practical problems in the strategy of forest adaptation to climate change and forest management regulation by developing intensive forest assessment methods (Hein *et al.* 2018; Abzhanova *et al.* 2018; Togisbayeva *et al.* 2022). Highly accurate assessment of aboveground woody biomass requires detailed land forest estimation, which is still a basic method. However, field research requires a lot of time and effort (Machar *et al.* 2016; Mukhametov *et al.* 2018; Sakharova *et al.* 2022).

Methods based on obtaining image data using remote sensing (multispectral or radar methods) demonstrate significant potential for rapid and up-to-date determination of plant biomass. They are affordable methods for determining vegetation cover indicators in remote areas (Wiggins *et al.* 2019). In the last two decades, studies based on a combination of field measurements and Landsat remote sensing data have become widespread, including studies on long-term dynamics of forest area and biomass density (Deo *et al.* 2017; Matasci *et al.* 2018). Landsat is especially popular in estimating forest biomass and sample sites since the images have an average spatial (30 m × 30 m) and temporal (16 days) resolution and wide coverage (Li *et al.* 2020). This spatial resolution of Landsat is similar to the size of sample plots in the national forest inventories of many countries, which reduces spatial errors when comparing pixels and sample plots (Nguyen *et al.* 2020).

Aerial laser scanning or laser altimetry is a method of active remote sensing that determines the topography of the Earth's surface by measuring the duration of the passage of the emitted laser pulse. The method involves the use of a photodiode that registers the echo reflected by a laser emitting short, infrared pulses to the Earth's surface. The photodiode allows for obtaining high-accuracy, three-dimensional data from large areas of forest plots, which are important for the management of forest resources. The spectral information provided by optical images can be used to identify tree species necessary for an accurate biomass assessment.

However, satellite images usually have a rough spatial resolution. In addition, because of exposure to aerosols and water vapor, remote sensing images require calibration and correction. An unmanned aerial system with multiple sensors may be relevant for collecting ultra-high spatial resolution data. As an alternative to optical remote sensors, light identification detection and ranging (lidar) can provide accurate structural information on forests for biomass assessment (Tijerín-Triviño *et al.* 2022). Wiggins *et al.* (2019) note that lidar survey is a cost-effective alternative to monitoring, which can provide high-resolution characterization of variations in forest structure depending on the type of terrain. The study on the forests of the Sierra de San Pedro Martir National Park (Baja California, Mexico) estimated the error of the processed lidar surveys data on trees of various height classes. The study also involved assessment of the total number of trees and the evaluation of the structure and spatial distribution in comparison with the results of forest estimation measurements. The consistency between lidar and field estimates of the forest structure, density, and spatial distribution was maximized by removing trees less than 12 m high.

Guo *et al.* (2017) used lidar to obtain data on woodlands of natural subregions of boreal and foothill forests of Alberta (Canada). Based on the data obtained, they note that lidar can accurately measure the three-dimensional structure of vegetation and can be widely used in the wild for habitat mapping, species distribution modeling, and for guiding biodiversity monitoring and species conservation assessment at the regional level (Gamoń *et al.* 2022). In addition, according to Ruiz *et al.* (2018),

Federal State Budgetary Educational Establishment of Higher Education "Ufa State Petroleum Technological University", Kosmonavtov, 1, Ufa, 450064, Russian Federation.

Corresponding Author: Rida Sultanova (ridasultanova1@rambler.ru)

Contributed by Desheng Liu, January 24, 2023 (sent for review February 17, 2023; reviewed by Ligong Pan, Raziya Issayeva, Sergey Golovatyi).

Photogrammetric Engineering & Remote Sensing
Vol. 89, No. 7, July 2023, pp. 445–454.
0099-1112/22/445–454

doi: 10.14358/PERS.23-00006R2

mapping of Mediterranean forest structure variables using object-oriented classification methods based on lidar data with low density (0.5 m^{-2}.), and nationally available multispectral Sentinel images, provides important information for assessing woody biomass, carbon stocks, and pasture suitability for forest fires prevention and control.

The study aims to test methods for monitoring current greenhouse gas levels of a representative forest landscape of a carbon polygon, obtain and process data of terrestrial woody biomass using lidar surveys, and to assess carbon dioxide (CO_2) and nitrogen oxide (NO_2) emissions in the air in a forest area.

Materials and Methods

The object of studies were plantings of the reserves of the forest–steppe region of the European part of Russia on the territory of the Republic of Bashkortostan with an area of 90 hectares (compartments 19 and 20 of the Ufa forestry of the Dmitrievsky district representing the "urban green belt" around Ufa city industrial center (Table 1)). The above plantings are homogeneous in climatic, edaphic, phytocenotic conditions, relief, and hydrology. The altitude in the area varies between 215 and 211 m; the elevation difference is 4 m. The area has a temperate continental climate with average temperatures of +19 °C in July and –15 °C in January. The maximum amount of precipitation is up to 500–600 mm, the minimum is 400–500 mm. The coordinates of the polygon are between north–west 54.763901 N, 55.711393 W, north–east 54.763881 N, 55.716268 W, south–east 54.762258 N, 55.716150 W, and south–west 54.762091 N, 55.710022 W.

The study used the last version of the Normalized Difference Vegetation Index (NDVI) data set, NDVI3g.v1. The data were obtained using NOAA's advanced Very High Resolution Radiometer (AVHRR) sensors as part of the Global Inventory Monitoring and Modeling System (GIMMS) (Tucker *et al.* 2005). The data were processed by the GIMMS team using an adaptive decomposition of the empirical model to solve problems related to calibration, sensor degradation, survey geometry, orbit drift, atmospheric pollution, and sampling associated with the AVHRR sensor (Pinzón *et al.* 2005). Pixels with average annual NDVI values of less than 0.1 were removed from satellite images (Zhou *et al.* 2001). The annual NDVI trend was calculated. Using delta interpolation and Hermite interpolation polynomial methods, the Climatic Research Unit data were scaled down from 0.5 degrees to a spatial resolution of 8 km to provide a similar resolution with NDVI data (Mosier *et al.* 2014).

The choice of NDVI was conditioned by the most commonly used indicators for predicting and evaluating various biophysical parameters, such as forest canopy, biomass, volume, and carbon (Vafaei *et al.* 2018). Normalized Green Red Difference Index (NGRDI), which evaluates the greening of the surface and is used to approximate green biomass at any stage of plant development, was obtained by calculating the reflection coefficient of the green and red zones of the electromagnetic spectrum, which are obtained from the true color image. This index can be used for phenological monitoring, which makes it possible to assess the surface greening and can be used to approximate green biomass at any stage of development. However, visual vegetation indices are not used as often as near-infrared indices due to the difference in digital numbers between the green and red stripes for vegetation and soil compared to the near-infrared and red stripes. Vegetation data were analyzed using allometric equations with a determination coefficient (R^2) of 0.85 (Malimbwi *et al.* 2016). Aboveground carbon was converted to carbon using a coefficient of 0.49 (IPCC Good Practice Guidance). The biomass was calculated for mixed coniferous-deciduous trees.

Aerial photography of the experimental forest plot of the carbon landfill was carried out. High-precision point cloud data for the study area were obtained using the DJI ZENMUSE L1 lidar created on the basis of a high-tech LIVOX AVIA solid-state laser sensor with triple reflection registration, a 70-degree view, a scanning frequency of 720 points per second, and a measurement range over s200 m. Test flights were conducted strictly along the same route at a speed of 5 m/s at an altitude of 45 meters; the wind speed in the flight echelon of the aircraft was 3–4 m/s. Lidar was installed on board DJI MATRICE 300 RTK. A permanent EFT network was used as a reference station. DJI ZENMUSE L1 laser scanning data processing was performed in DJI TERRA software.

Table 1. Brief characteristic of sample areas.

No	Area, ha	Age, Years	Composition	Diameter, cm	Height, m	Density	Volume, Cubic Meters
1	0.8	45	6 lindens	16.0	19.0	0.7	130.0
			4 birches	24.0	21.0		90.0
2	57.5	95	10 lindens	36.0	24.0	0.6	290.0
3	1.0	35	4 lindens	12.0	12.0	0.5	30.0
			3 elms	8.0	10.0		20.0
			2 maples	8.0	8.0		10.0
			1 aspen	18.0	19.0		10.0
4	1.7	35	7 birches	14.0	19.0	0.8	180.0
			3 lindens	12.0	13.0		80.0
5	3.7	45	5 birches	18.0	21.0	0.7	280.0
			3 lindens	14.0	17.0		170.0
			1 aspen	20.0	21.0		60.0
			1elm	16.0	15.0		30.0
6	4.4	95	8 birches	30.0	24.0	0.6	770.0
			1 birch	28.0	24.0		100.0
			1 linden	26,0	21.0		100.0
7	0.9	45	7 lindens	12.0	17.0	0.8	160.0
			2 birches	18.0	19.0		50.0
			1 maple	22.0	19.0		20.0

Table 2. Zenmuse L1technical parameters.

Parameter	Value
Pulse repetition rate	100 kHz
Laser wavelength	1550 nm
Pulse duration	3.5 ns
Laser beam divergence	≤0.5 millirad
Separation of multiple targets with one shot	0.6 m
Width-pulse returned resolution	0.15 m
Scan template	parallel scanning
Range of scanning angles	30°
Ground sample spot diameter	0.5 m (at a flight altitude of 1000 m)

The plot is a square measuring 800 × 800 m, divided into 20 small squares measuring 40 × 40 m. The inventory of 11 203 trees was made. Ground measurements were synchronized with hyperspectral data using the *WorldView-3* satellite. *WorldView-3* (*WV-3*) launched in 2014 is a commercial high-resolution imaging satellite operated by DigitalGlobe. Currently, the satellite is controlled from the United States by Maxar Technologies. The *WV-3* thermal imager provides one of the highest commercial data transmission solutions, with a resolution of only 30 cm. Such high performance allowed the creation of new applications for processing satellite data, including counting bird populations in remote areas. The satellite covers a ground swath of 13.1 km, and also allows getting images with multiple bands to create mosaic images and stereo images. The *WV-3* has a predicted absolute geolocation accuracy of less than 3.5 m CE90 (90% circular error) without ground control. The satellite is in a sun-synchronous orbit, at an altitude of 617 km and an inclination of 98 °. Local time on the descending node (LTDN) is 1330 hours and the period is 97 minutes. Spectral range is 60 nm, spectral resolution –3 nm at 700 nm, and 10 nm at 1400/2100 nm; sampling interval of 1.4 nm at 350 nm to 1050 nm and 2 nm at a wavelength from 1000 to 2500 nm and a scanning interval of 0.1 seconds. Bright, dark, and some typical ground objects were measured for atmospheric correction of the hyperspectral image. High-density aerial photography data were obtained in August 2022. The lidar LIVOX system included a Zenmuse L1 laser scanner. Zenmuse L1 gives a complete waveform analysis that provides a detailed vertical structure of the forest. Zenmuse L1 parameters are given in Table 2.

The flight covered an area of 2 km² with a flight height of 150–170 m, which corresponds to a relative flight height above the crown of about 100 m. Eight runways with a side overlap of 90% were obtained. The points density was approximately 12 points/m². The classification of points, the generation of a digital surface model (DSM) and a digital terrain model (DTM, Figure 1) were carried out using the TerraScan software (TerraSolid, Helsinki, Finland).

The crown height model (Figure 2a) was calculated using the difference between the DSM and the DTM with a resolution of 0.5 m. A digital orthophoto with a resolution of 0.2 m was generated based on DSM and DTM images obtained using lidar and TerraPhoto software (TerraSolid, Helsinki, Finland).

Hyperspectral data were also obtained in August 2022 (Figure 2b). The data were being collected from 10:00 A.M. to 2:00 P.M. The spectral mode provides up to 288 spectral bands. The spatial mode applied during the experiment provided a spatial resolution of 0.5 m when using 23 spectral bands of 1484 pixels. First, radiometric and geometric corrections of raw hyperspectral images were made using Itres V1.2 (ITRES, Calgary, AB, Canada). As a result, brightness images with a ground sampling distance of 1 m were obtained. Then an empirical calibration of the line was used for atmospheric correction to calibrate the emissions according to the reflection coefficient of the surface. After that, the empirical line calibration method assumes that there is a linear relationship between the brightness recorded by the sensor and the corresponding spectral reflectivity measured locally, which requires two or more bright and dark targets in the image coverage area. In this study, a power line pole acted as dark and bright targets, respectively. The field spectra of dark and bright targets were measured simultaneously.

DJI ZENMUSE L1 equipment was used together with a professional visualized analytical software Sniffer4D Mapper gas analyzer to make a survey of the same territory. Sniffer4D Mapper quickly transmits air sampling data, displays gas concentration in real time, takes pictures, and records a video. We used the method of direct carbon measurement. Measurements of carbon dioxide (CO_2) and nitrogen oxide (NO_2) emissions in the air at a height of 100, 150, 200 в 250 и 300 м in the Tilia cordata Mill plantation were carried out using a Sniffer4D gas analyzer. Sniffer4D can scan specific areas in two-dimensional/three-dimensional formats and generate intuitive and maximally accurate data. Sniffer4D is installed on drones and cars and used for searching, mapping, monitoring gases, and air pollution control. Other stationary monitoring stations are much more low-functioning. Compared to a

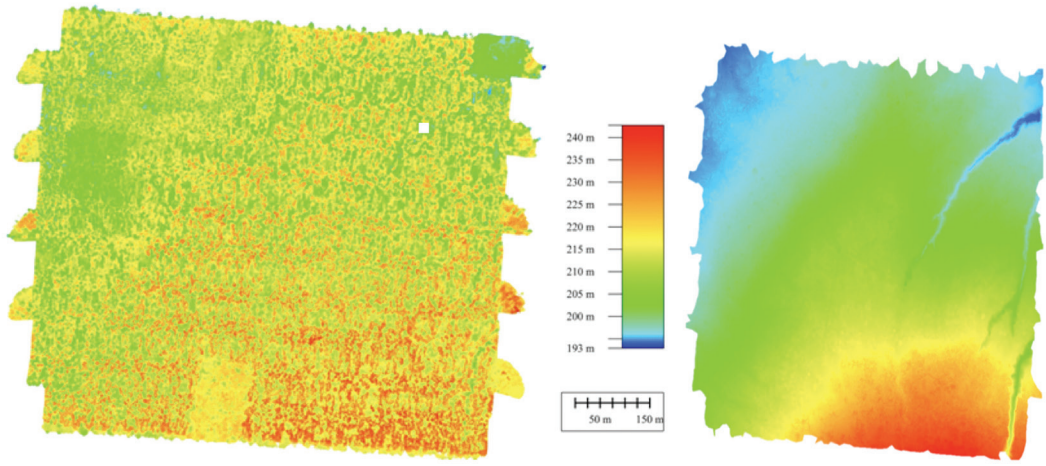

Figure 1. Digital surface model, (DSM) (a) and digital terrain model, (DTM) (b).

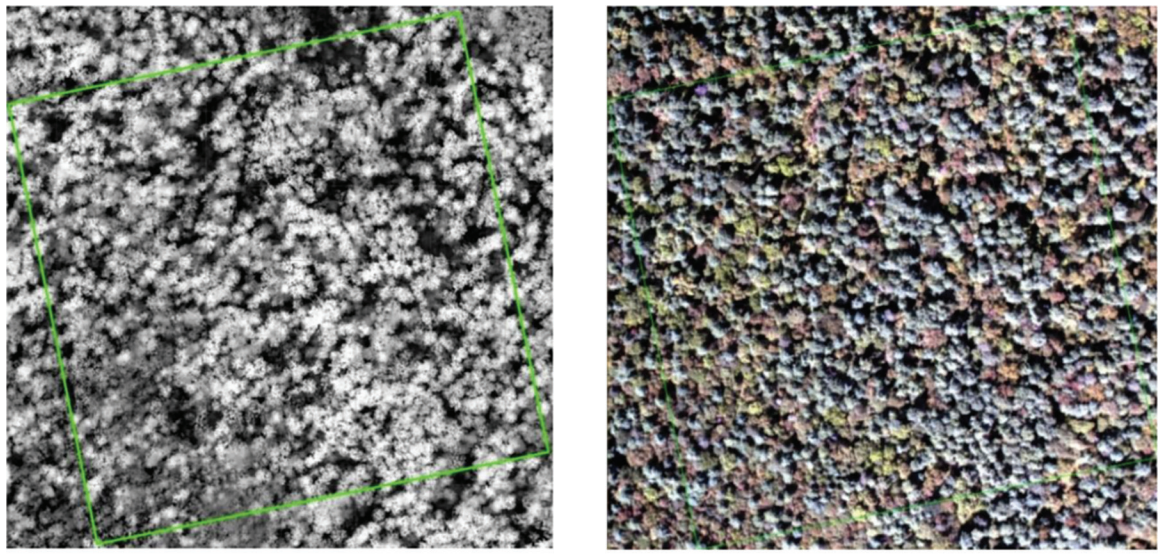

Figure 2. Processed images of the study area.

scientific-level monitoring station, the correlation of long-term data (R^2) ranges from 0.81 to 0.95; long-term root-mean-square errors after calibration are <±10%.

Statistical Analysis

The measurements of trees obtained using lidar were processed using regression models and cross-validation to estimate the crown diameter and biomass of trees within the site.

Results

For three-dimensional visualization of contours and surface analysis, a digital relief model was obtained. The model demonstrates the shape of the surface between points at a given level and interpolation of the elevations' data obtained during remote sensing. Each lidar point is a reverse pulse, color-mapping its location and altitude above sea level. The technology of the tree segmentation by splitting one crown layer at a time, removing it from the point cloud, and segmenting the crowns inside it allows outlining individual trees, and automatically get their relative height (Figure 3). Processing of laser scanning indicators allows obtaining the object geometry.

The DJI ZENMUSE L1 aerial laser scanning system has proven to be simple and easy to use when planning flights and processing data. It allows getting a detailed point cloud and use it for further work on the ground, to solve operational monitoring tasks and create three-dimensional terrain models. Using this equipment in forest taxation becomes possible tanks to the quality and detail degree of data recording of laser scanning of the structure of trees, trunks, and branches. Using a remote-sensing technique in the study of a carbon landfill allowed obtaining accurate data on the location of trees and their height. However, the survey was carried out during the most active vegetation period when the canopy density was high, which affected the accuracy of measurements of the diameter of trees obtained using lidar filming. This fact is confirmed by the survey results. The diameter indicators turned out to be less than the diameters obtained during ground-based forest studies. Thus, the taxation indicators obtained by lidar filming should be supplemented by ground-based studies.

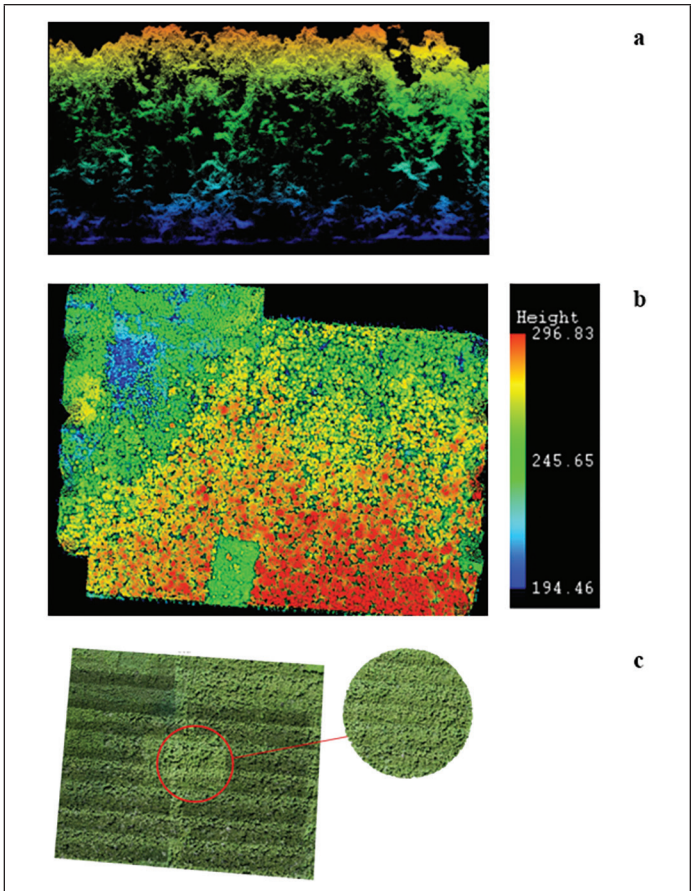

Figure 3. Mapping of a forest compartment: (a) vertical profile; (b) horizontal profile; (c) contours of individual trees.

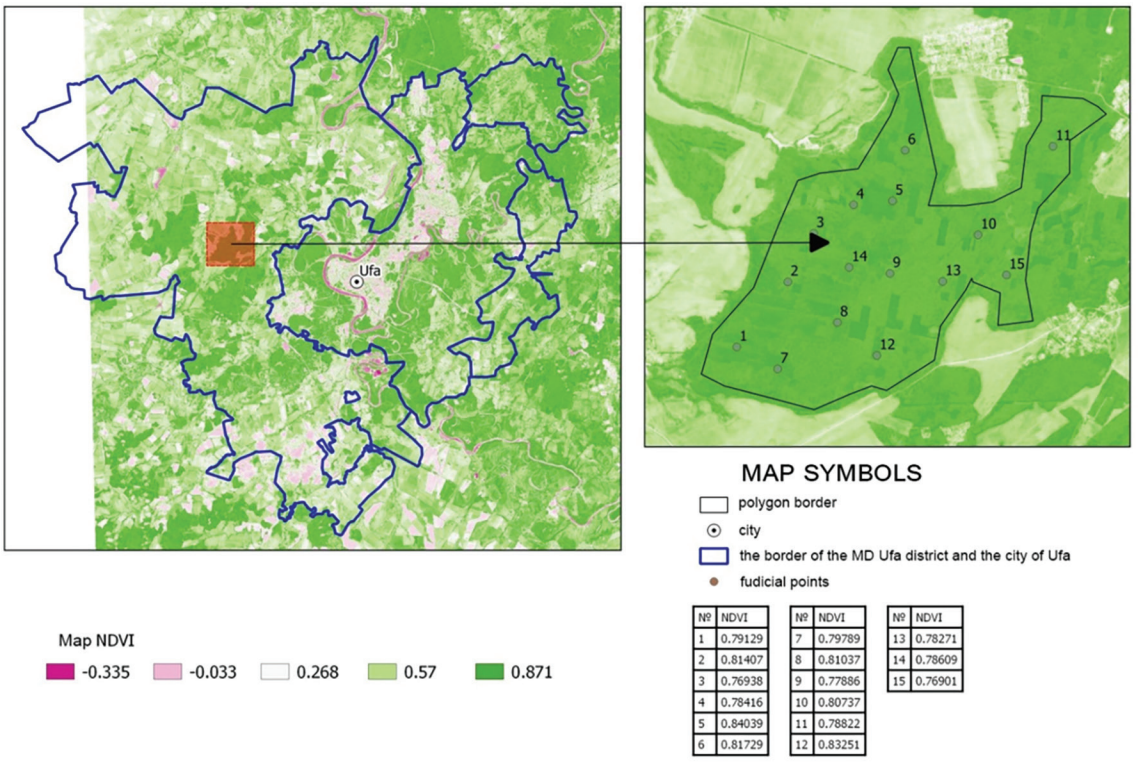

Figure 4. Normalized Difference Vegetation Index (NDVI) map of the carbon landfill forest compartment.

Extensive experience has been accumulated in the successful

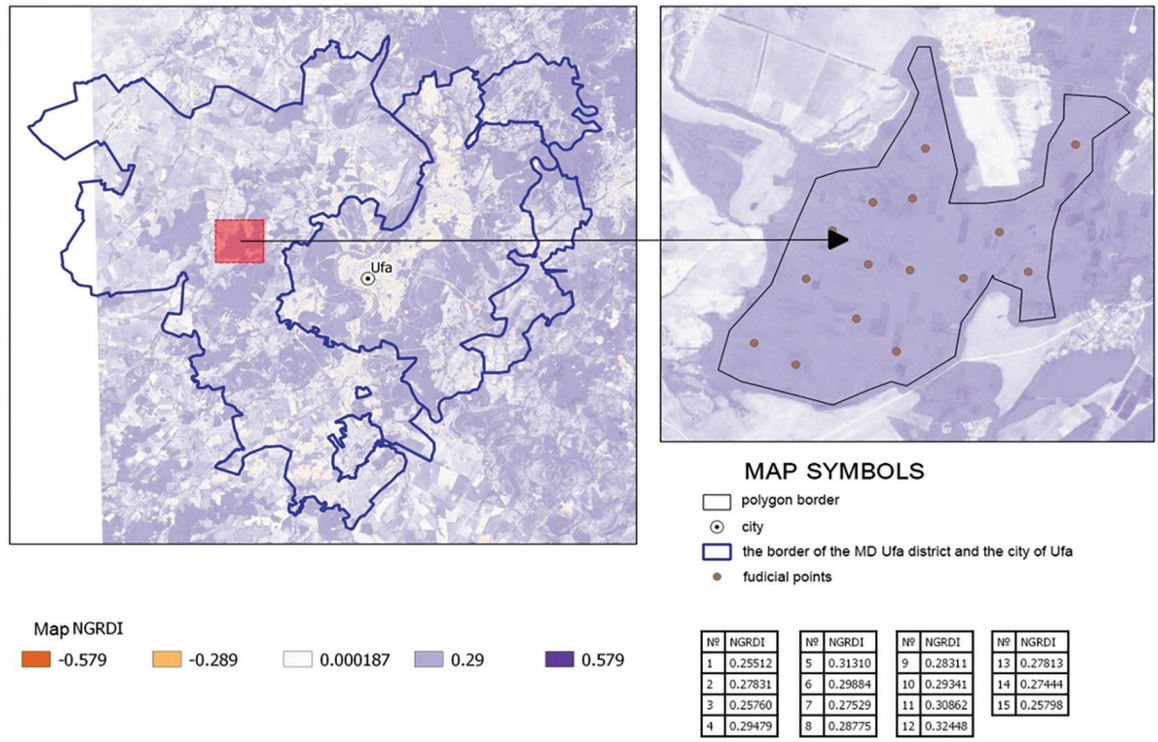

№	NGRDI
1	0.25512
2	0.27831
3	0.25760
4	0.29479

№	NGRDI
5	0.31310
6	0.29884
7	0.27529
8	0.28775

№	NGRDI
9	0.28311
10	0.29341
11	0.30862
12	0.32448

№	NGRDI
13	0.27813
14	0.27444
15	0.25798

Figure 5. Normalized Green Red Difference Index (NGRDI) map of the carbon landfill forest compartment.

application of vegetation indices for the diagnosis of vegetation conditions at different phenological stages.

The research estimated the relationship between the biomass of the studied area with the NDVI (Figure 4), which reflects the chlorophyll content in plants, and approximates biomass, and the NGRDI (Figure 5), which assesses the surface greening and is used to approximate green biomass at any stage of plant development.

Figure 6 shows the distribution of terrestrial biomass based on lidar-shooting indicators: tree heights, crown diameter and area, number of trees, etc. (indicators: TreeID, TreeLocationX, TreeLocationY, TreeHeight, diameter breast height (DBH), CrownDiameter, CrownArea, CrownVolume, OldID).

The assessment and correlation of the above-ground biomass of the studied area with NDVI and NGRDI were performed by randomly selecting 15 points and using point sampling. According to the values of NDVI, and NGRDI indices of above-ground biomass for each selected point, the vegetation indices values are compared to the values of above-ground mass (Figure 7).

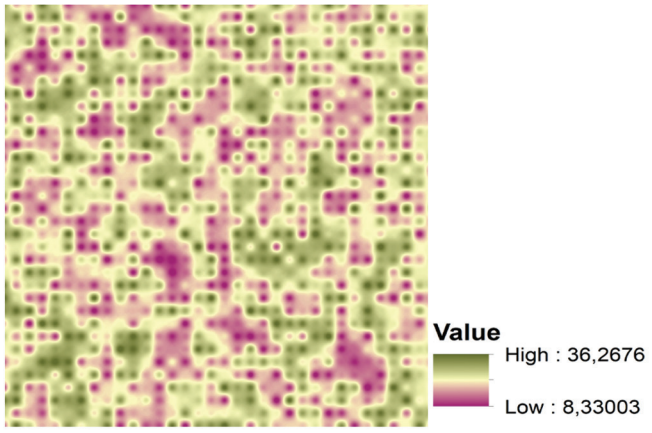

Figure 6. Above-ground biomass of the forest compartment under study.

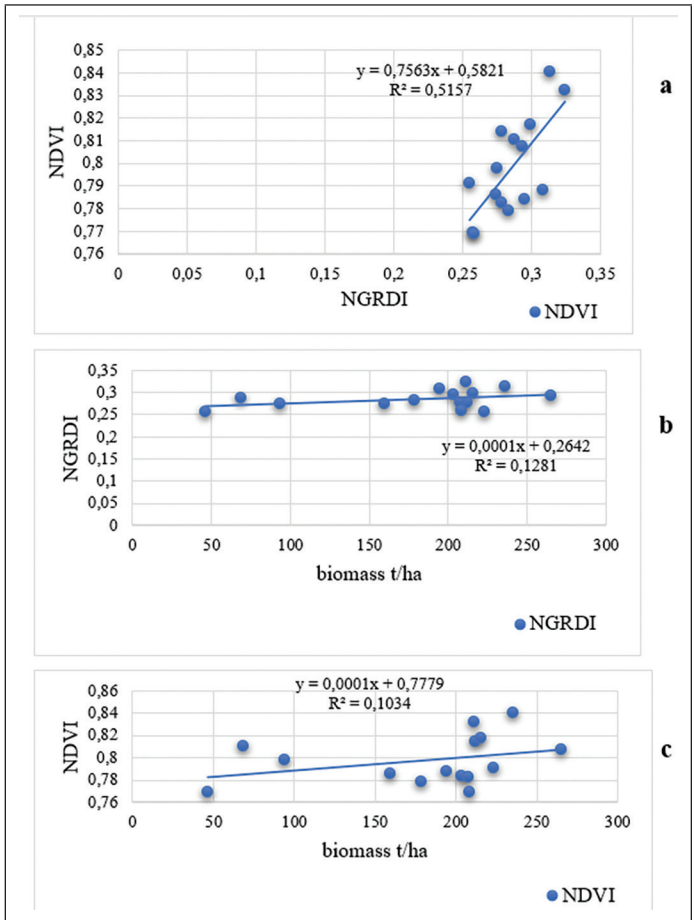

Figure 7. Graphs of the interdependence of vegetation indices (NDVI, NGRDI) (a) and their dependence on the volume of above-ground biomass (b, c). NDVI = Normalized Difference Vegetation Index; NGRDI = Normalized Green Red Difference Index.

The determination coefficient between NDVI and NGRDI is 0.52, which indicates the interchangeability of these vegetation indices. This fact is confirmed by the close values of R^2 of the relationship between the volume of above-ground biomass and the vegetation index NDVI ($R^2 = 0.10$), and between the volume of biomass and NGRDI index ($R^2 = 0.13$). The increase in NDVI and NGRDI values is associated with the presence of forest vegetation. The close relationship between indices and biomass indicates that infrared images allow better determination of biomass, allowing the mapping of the soil and vegetation cover class based on a multispectral classification of satellite images in the studied area. This is due to the near infrared (NIR) bands, which provide more information about the characteristics of trees and their biophysical parameters, such as the leaf area index, than visual stripes.

Land cover change is one of the factors of carbon sequestration (Deo *et al.* 2017). The main methods of field research are forest estimation, the use of stand development tables and a vortex covariance method based on direct measurement of the CO_2 flux in small areas (Zhang *et al.* 2012).

The average carbon stock and the NDVI index value for each site were obtained during the research. Fifty percent of carbon stocks were compared with NDVI and the resulting training samples (Table 3). It was ensured that the training samples covered all the layers observed in the image. Before making any classification, a pair-wise correlation was performed to find out the degree of relationship between the carbon stocks and NDVI. In 2021, the average carbon stock in the studied area was 11.89 t/ha, with an annual carbon absorption rate of 0.10 t/ha. During the growing season from May to June, CO_2 emissions reached 333.4 ppm at the daytime and 101.7 ppm at night, which is due to different temperature conditions and humidity during the daytime and at night.

Measurements made at the forest site in 2022 showed that the concentration of CO_2 decreases with increasing altitude. The maximum concentration of CO_2 is 651.38 mg/m3 at an altitude of 100 m, which is 7.0% higher than at 300 m. On a forest plot near the industrial zone of an oil refinery, the concentration of carbon dioxide is 30% higher compared to the height of 300 m at an altitude of 100 m. A data table has been compiled using the Sniffer4D Mapper software (Tables 4 and 5; Figure 8).

The box plot of the concentration of CO_2 shows the median (mean value), lower and upper quartiles, minimum and maximum sampling values, and outliers (Figure 9). Some similar diagrams can be placed side by side horizontally or vertically to visually compare one distribution with another. The distances between different parts of the diagram allow determining the degree of dispersion (variance) and asymmetry of the data to identify outliers.

The concentration of CO_2 is closely correlated with the values of temperature and humidity. The linear regression curve (red line) shows the dependence of the carbon dioxide concentration $R^2 = 0.388$ on temperature, and $R^2 = 0.667$ on humidity. r = 0.807 (Figures 10 and 11).

Discussion

Many researchers have reported methods for obtaining various forest variables based on lidar measurements (Magnussen *et al.* 2018). Lidar point clouds are often used particularly in a wide range of forestry applications as a data source for obtaining forest estimation indicators

Table 3. Values of above-ground biomass, vegetation indices, and greenhouse gas emissions in the carbon landfill forest area.

Inventory Point	Biomass, tonn	Vegetation Indices		Greenhouse Gas Emissions					
						CO_2, ppm		NO_2, mcg/m3	
		NGRDI	NDVI	CO_2, t/year	NO_2, g/cm²	daytime	night	daytime	night
1	223.26	0.25512	0.79129	22.84873	1.261553	333.4	102.6	25.5	27.3
2	212.02	0.27831	0.81407	12.1079	1.261553	331.1	101.7	26.0	26.3
3	46.28	0.2576	0.76938	8.918	1.261553	330.4	103.8	24.6	27.5
4	203.68	0.29479	0.78416	4.0474	1.261553	332.7	103.1	26.5	27.9
5	235.71	0.3131	0.84039	17.9242	1.265326	329.6	103.0	26.9	28.8
6	215.57	0.29884	0.81729	13.3329	1.265326	330.9	102.6	27.4	27.5
7	93.84	0.27529	0.79789	10.4615	1.265326	330.4	102.2	28.4	28.8
8	68.52	0.28775	0.81037	1.5876	1.261553	330.8	103.4	27.9	28.8
9	178.52	0.28311	0.77886	13.0634	1.261553	329.7	103.6	31.6	27.3
10	265.25	0.29341	0.80737	16.2876	1.261553	329.6	103.1	30.7	28.8
11	194.24	0.30862	0.78822	4.7432	1.261553	331.9	102.2	32.1	28.4
12	211.52	0.32448	0.83251	15.1312	1.261553	331.1	102.9	31.2	27.3
13	207.52	0.27813	0.78271	7.0413	1.261553	330.4	101.8	31.6	27.3
14	159.45	0.27444	0.78609	6.8747	1.261553	330.8	102.1	32.1	24.9
15	208.42	0.25798	0.76901	24.0345	1.261553	331.9	103.4	31.2	28.4

NDVI = Normalized Difference Vegetation Index; NGRDI = Normalized Green Red Difference Index.

Table 4. Measurement data obtained using a gas analyzer on a forest plot.

Timing Mark	Distance, m	Air Temperature, °C	Air Humidity, %	Air Pressure, Pa	Concentration of CO_2 mg/m3
10:20:05	100	11.11	86	98.611	651.38
11:32:15	150	13.52	83	98.596	649.76
12:36:25	200	13.52	80	95.660	644.76
13:15:35	250	15.43	76	94.606	630.51
14:40:45	300	16.24	651.72	92.630	606.65

Table 5. Carbon dioxide (CO_2) concentration.

The Object of the Study	Measurement Height, m	Maximum Concentration of CO_2 mg/m3	Minimum Concentration of CO_2 mg/m3	Average Value of CO_2, mg/m3	Average Value of CO_2, ppm
Forest	100	655.90	646.85	651.38	355.8
Industrial zone	100	909.89	852.93	879.98	480.7

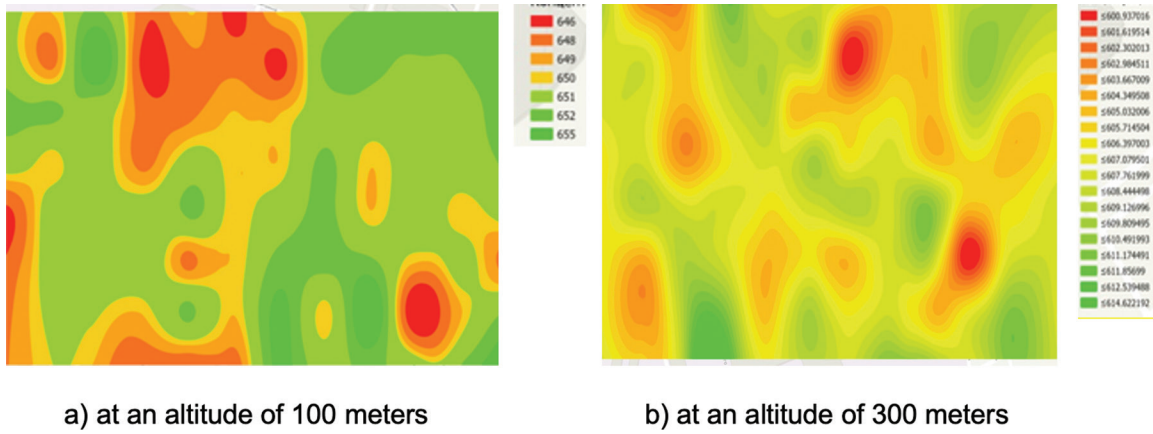

Figure 8. Concentration of carbon dioxide (CO_2) mg/m3 in a forest area.

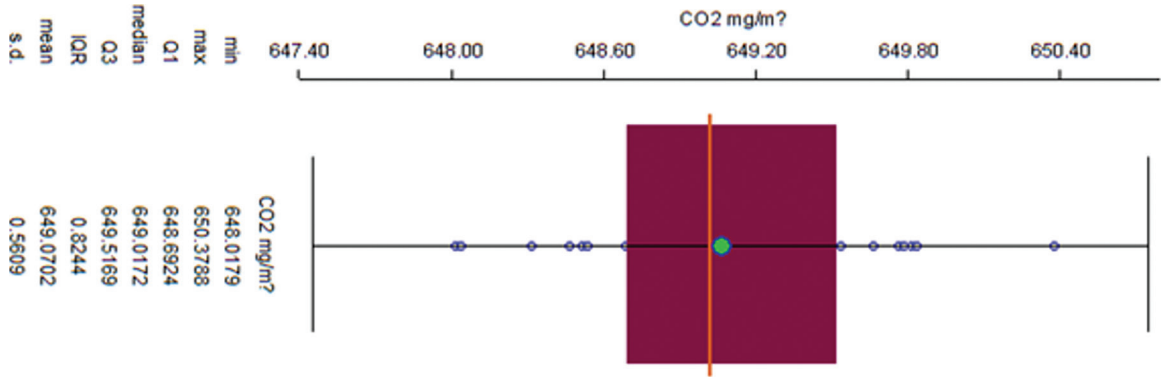

Figure 9. Diagram of the range of concentration of carbon dioxide (CO_2).

such as trunk density (Knapp *et al.* 2018), tree height, species composition, crown size, wood volume (Silva *et al.* 2018), and AGB (Strîmbu *et al.* 2017). For example, on-board laser scanning data can be used to obtain three-dimensional tree structures, thus contributing

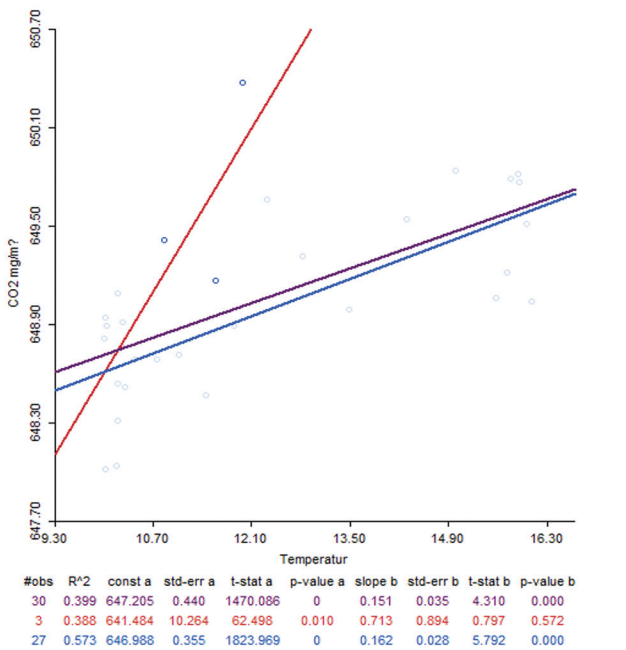

#obs	R^2	const a	std-err a	t-stat a	p-value a	slope b	std-err b	t-stat b	p-value b
30	0.399	647.205	0.440	1470.086	0	0.151	0.035	4.310	0.000
3	0.388	641.484	10.264	62.498	0.010	0.713	0.894	0.797	0.572
27	0.573	646.988	0.355	1823.969	0	0.162	0.028	5.792	0.000

Figure 10. Linear regression of the dependence of carbon dioxide concentration on air temperature.

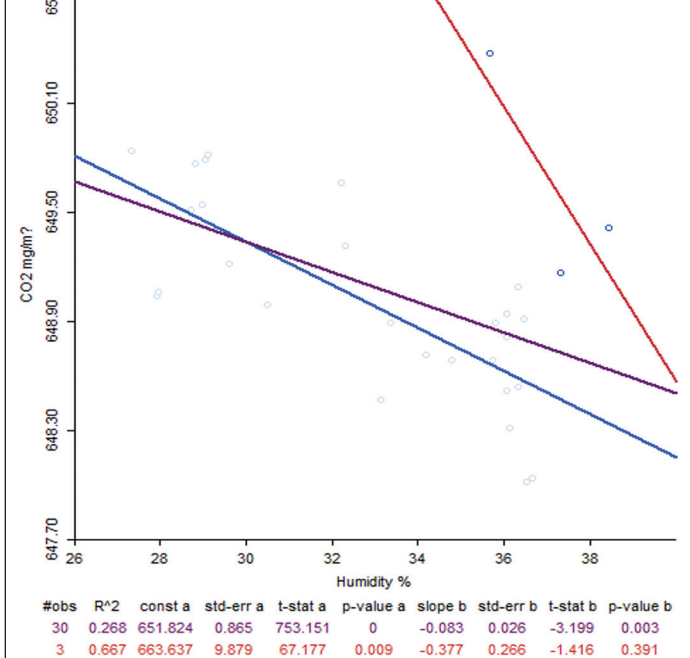

#obs	R^2	const a	std-err a	t-stat a	p-value a	slope b	std-err b	t-stat b	p-value b
30	0.268	651.824	0.865	753.151	0	-0.083	0.026	-3.199	0.003
3	0.667	663.637	9.879	67.177	0.009	-0.377	0.266	-1.416	0.391
27	0.587	652.880	0.654	998.443	0	-0.118	0.020	-5.956	0.000

Figure 11. Linear regression of the dependence of carbon dioxide concentration on air humidity.

to an effective large-scale three-dimensional forest inventory (Silva *et al.* 2018) and providing practical solutions to problems arising from large-scale estimates of biomass in forests. As mentioned in many sources, the accuracy of the biomass estimate corresponds to the accuracy of measuring the height of trees. AGB assessment can be carried out using two main methods (Yan *et al.* 2021). First, a method where individual trees are detected, isolated, and segmented from measured point clouds. Subsequently, the tree biomass is modeled by calculating the volume of branches and tree trunks through a three-dimensional geometric reconstruction of the tree structure.

Some researchers use crown segmentation of individual trees (Jarron *et al.* 2020) and classification of tree species (Xu *et al.* 2020). According to researchers, the simplest method of modeling a tree is an inventory within a compartment using predefined regression models such as DBH and height (Pourshamsi *et al.* 2021). In addition, several researchers have focused on developing automated modeling methods or algorithms to create a detailed representation of individual trees. Günlü *et al.* (2014) determined a close relationship between AGB, the values of the reflection coefficient of individual bands, and 10 vegetation indices (VIS) obtained from the Landsat satellite image for pine forests in northwestern Turkey. The VIS give a better estimate of AGB ($R^2 = 0.606$) compared with the reflection values of individual bands TM 1 and TM 2 ($R^2 = 0.465$). One method involves fitting regular geometric models, such as circles (Bienert *et al.* 2007) and cylinders (Thies *et al.* 2004), using voxel-based representations (Jupp *et al.* 2009) or grids (Antonarakis *et al.* 2009). A method based on model selection using conventional geometric models, in particular a parametric model, can be used directly to estimate the volume of the tree, which makes this method a simple solution. However, real treelike structures are formed randomly. The difference between conventional geometric models and real forms of tree structures affects the accuracy of the volume estimate (Li and Liu 2019). Second, methods based on plots in which, instead of detecting individual trees, measuring the height of the crown surface using lidar surveys can be compared with tree inventory plots measured in the field with a known biomass. Thus, a predictive model can be developed based on biomass reference estimates and applied to large-scale areas (Asner and Mascaro 2014). In the work of Matasci *et al.* (2018), various structural indicators based on lidar measurements were extracted for large-scale mapping of Canadian boreal forest biomass. Lidar point clouds obtained using high-speed UAVs cannot provide high-precision measurements of tree structures and obtaining lidar data of the same quality is a difficult task requiring precise control of the flight route since some flight parameters must be adapted to the relief of the measured area. However, the present study has confirmed the possibility of using structural and spectral attributes obtained from multispectral images, which allowed developing a predictive model for estimating AGB biomass and applying it to the area of interest, including the CO_2 flux calculation. In addition, lidar surveys are effective for local landscape forecasting.

The methods used to estimate carbon stocks also differ depending on the scale used. They include methods for local plots (Marziliano *et al.* 2017), a combination of measurement data and allometric equations for local and semi-regional scales, and remote sensing methods on a regional, national, or global scale (Avitabile *et al.* 2012; Ponce-Hernandez *et al.* 2004) described in detail the principle of tree allometry connected with changes in carbon in biomass. Situmorang *et al.* (2016) got similar results in Indonesia. They noted a high dependence between the NDVI index and carbon stocks (determination coefficient $R^2 = 0.728$, average carbon value 46.32 t/ha). When using large-scale biomass mapping, differences in expert data and the allometric equations, both empirical (Jenkins 2004) and modeled (Fehrmann and Kleinn 2006), can lead to large uncertainties (Stephenson *et al.* 2014). Productivity models use biomass expansion coefficients, which are another source of uncertainty in carbon accounting at the national level (Schöne and Schulte 1999). Studies comparing above-ground forest biomass using two or more estimation methods show some variability in the results (Pechanec *et al.* 2017). Soil carbon estimation has also shown variability (Liebens and VanMolle 2003). In this regard, calibration and verification of remote sensing data based on accurate ground (site) reference measurements of biomass is recommended (Valbuena *et al.* 2017).

Conclusions

Research on a forest site with a relief, the vegetation structure, and soil cover representative of the territory of the Republic of Bashkortostan, is aimed at enhancing scientific potential for development and testing of technologies for controlling the balance of climatically active gases of natural ecosystems. Measurements of greenhouse gas emissions and uptake are carried out at the carbon polygon to assess the spatial and temporal variability of the flows of climatically active gases and carbon balance. Methods in the field of environmental control are being tested.

Considering the rate of change of forest ecosystems and the time required for their ground-based monitoring, it is advisable to use remote sensing methods that provide important advantages (speed, repeatability, coverage width, non-destructive approach) (Féret and De Boissieu 2020; Pechanec *et al.* 2022). The research involved the estimation of the volume of AGB in the carbon landfill forest area of the broad-leaved forests of the Republic of Bashkortostan. The estimation was performed using the crown diameter index of trees obtained by lidar survey and by calculating NDVI and NGRDI vegetation indices. The research revealed the interchangeability of NDVI and NGRDI vegetation indices when assessing AGB and the reliability of biomass determining using radar classification of lidar images in the studied area, together with vegetation indices, since the NIR bands provide more information about the characteristics of trees and biophysical parameters, such as the leaf area index, than the Red Green Blue visual bands. The relationship between the NDVI and NGRDI indices at the research points is characterized by a determination coefficient equal to 0.52. Above-ground biomass reserves closely correlate with the values of NDVI and NGRDI vegetation indices. The research established close values of R^2 at the points of studies of the relationship between the above-ground biomass volume and the vegetation index NDVI ($R^2 = 0.10$), and between the biomass volume and the index NGRDI ($R^2 = 0.13$). An increase in the values of NGRDI from 0.25 to 0.31 and of NDVI from 0.76 to 0.83 is associated with an increase in the density of forest vegetation. The assessment of the emission of CO_2 and NO_2 during the growing season in the forest air cover level revealed differences in values in the daytime and at night. The value of CO_2 reached 333.4 ppm during the daytime and 101.7 ppm at night, which is associated with different temperature conditions and humidity in the daytime and at night. Measurements made in 2022 at the forest site showed that the concentration of CO_2 decreases with increasing altitude and closely correlates with the values of temperature and humidity.

The results determined promising methods of inventory of the carbon landfill forest area for the assessment and mapping of AGB based on data obtained from several sources, including ground-based forest estimation.

These methods involve:

(1) integration of a UAV-based digital camera and lidar sensors in order to optimize the efficiency and cost of data collection;
(2) taking advantage of high-resolution aerial photographs and sparse lidar point clouds using an information fusion approach and the ability to compensate for their shortcomings.

The research was carried out as part of the Program for the creation and operation of a carbon landfill on the territory of the Republic of Bashkortostan "Eurasian Carbon Landfill" for 2022–2023.

Acknowledgments

Rida Sultanova and Radik Mustafin conceived and designed the experiments. Rida Sultanova performed the experiments. Radik Mustafin analyzed the data. Rida Sultanova drafted the manuscript. Critical revision of manuscript for important intellectual content were done by Rida Sultanova and Radik Mustafin. This research did not receive any

specific grant from funding agencies in the public, commercial, or not-for-profit sectors. Data is available on request.

Funding

This research was performed within the state assignment framework of the Ministry of Science and Higher Education of the Russian Federation: "Program for the creation and functioning of a carbon polygons on the territory Bashkortostan Republic "Eurasian carbon polygon" for 2022_2023" (Publication number: FEUR-2022-000 1).

References

Abzhanova, S. A., A. A. Bulambayeva, B. S. Zhetpisbaeva, M. O. Kozhakhiyeva, A. I. Matibayeva, M. S. Serikkyzy and B. A. Rskeldiev. 2018. Research of the impact of a vegetable protein composition on the functional and technological properties of national meat products. *Asian Journal of Microbiology, Biotechnology and Environmental Sciences* 20(4):1071–1080. http://hdl.handle.net/123456789/1399.

Antonarakis, A. S., K. S. Richards, J. Brasington and M. Bithell. 2009. Leafless roughness of complex tree morphology using terrestrial lidar. *Water Resources Research* 45(10):1–10. https://doi.org/10.1029/2008WR007666.

Asner, G. P. and J. Mascaro. 2014. Mapping tropical forest carbon: Calibrating plot estimates to a simple LiDAR metric. *Remote Sensing of Environment* 140:614–624. https://doi.org/10.1016/j.rse.2013.09.023.

Avitabile, V., A. Baccini, M. A. Friedl and C. Schmullius. 2012. Capabilities and limitations of Landsat and land cover data for aboveground woody biomass estimation of Uganda. *Remote Sensing of Environment* 117:366–380. https://doi.org/10.1016/j.rse.2011.10.012.

Bienert, A., S. Scheller, E. Keane, F. Mohan and C. Nugent. 2007. Tree detection and diameter estimations by analysis of forest terrestrial laserscanner point clouds. *ISPRS Workshop on Laser Scanning*, held in Espoo, Finland, 12–14 September 2007.

Chan, E.P.Y., T. Fung and F.K.K. Wong. 2021. Estimating above-ground biomass of subtropical forest using airborne LiDAR in Hong Kong. *Scientific Reports* 11(1):1751. https://doi.org/10.1038/s41598-021-81267-8.

Deo, R. K., M. B. Russell, G. M. Domke, C. W. Woodall, M. J. Falkowski and W. B. Cohen. 2017. Using Landsat time-series and LiDAR to inform aboveground forest biomass baselines in northern Minnesota, USA. *Canadian Journal of Remote Sensing* 43(1):28–47. https://doi.org/10.1080/07038992.2017.1259556.

Fehrmann, L. and C. Kleinn. 2006. General considerations about the use of allometric equations for biomass estimation on the example of Norway spruce in central Europe. *Forest Ecology and Management* 236(2–3):412–421. https://doi.org/10.1016/j.foreco.2006.09.026.

Féret, J. B. and F. De Boissieu. 2020. biodivMapR: An r package for α-and β-diversity mapping using remotely sensed images. *Methods in Ecology and Evolution* 11(1):64–70. https://doi.org/10.1111/2041-210X.13310.

Gamoń, F., M. Tomaszewski, G. Cema and A. Ziembińska-Buczyńska. 2022. Adsorption of oxytetracycline and ciprofloxacin on carbon-based nanomaterials as affected by pH. *Archives of Environmental Protection* 48(2):34–41. https://doi.org/10.24425/aep.2022.140764.

Günlü, A., I. Ercanli, E. Z. Başkent and G. Çakır. 2014. Estimating aboveground biomass using Landsat TM imagery: A case study of Anatolian Crimean pine forests in Turkey. *Annals of Forest Research* 57(2):289–298. https://doi.org/10.15287/afr.2014.278.

Guo, X., N. C. Coops, P. Tompalski, S. E. Nielsen, C. W. Bater and J. J. Stadt. 2017. Regional mapping of vegetation structure for biodiversity monitoring using airborne lidar data. *Ecological Informatics* 38:50–61. https://doi.org/10.1016/j.ecoinf.2017.01.005.

Hein, J., A. Guarin, E. Frommé and P. Pauw. 2018. Deforestation and the Paris climate agreement: An assessment of REDD+ in the national climate action plans. *Forest Policy and Economics* 90:7–11. https://doi.org/10.1016/j.forpol.2018.01.005.

International Union of Forest Research Organizations (IUFRO). 2020. Post-2020 STRATEGY. Interconnecting Forests, Science and People. <https://www.iufro.org/fileadmin/material/science/divisions/toolbox/iufro-strategy-2020-post.pdf> Accessed

Jarron, L. R., N. C. Coops, W. H. MacKenzie, P. Tompalski and P. Dykstra. 2020. Detection of sub-canopy forest structure using airborne LiDAR. *Remote Sensing Environment* 244:111770. https://doi.org/10.1016/j.rse.2020.111770.

Jenkins, J. C. 2004. *Comprehensive Database of Diameter-Based Biomass Regressions for North American Tree Species (No. 319)*. Radnor, Pa.: U.S. Department of Agriculture, Forest Service, Northeastern Research Station.

Jupp, D. L., D. S. Culvenor, J. L. Lovell, G. J. Newnham, A. H. Strahler and C. E. Woodcock. 2009. Estimating forest LAI profiles and structural parameters using a ground-based laser called 'Echidna®. *Tree Physiology* 29(2):171–181. https://doi.org/10.1093/treephys/tpn022.

Knapp, N., R. Fischer and A. Huth. 2018. Linking lidar and forest modeling to assess biomass estimation across scales and disturbance states. *Remote Sensing of Environment* 205:199–209. https://doi.org/10.1016/j.rse.2017.11.018.

Li, L. and C. Liu. 2019. A new approach for estimating living vegetation volume based on terrestrial point cloud data. *PloS One* 14(8):e0221734. https://doi.org/10.1371/journal.pone.0221734.

Li, Y., M. Li, C. Li and Z. Liu. 2020. Forest aboveground biomass estimation using Landsat 8 and Sentinel-1A data with machine learning algorithms. *Scientific Reports* 10(1):9952. https://doi.org/10.1038/s41598-020-67024-3.

Liebens, J. and M. VanMolle. 2003. Influence of estimation procedure on soil organic carbon stock assessment in Flanders, Belgium. *Soil Use and Management* 19(4):364–371. https://doi.org/10.1111/j.1475-2743.2003.tb00327.x.

Machar, I., J. Simon, K. Rejsek, V. Pechanec, J. Brus and H. Kilianova. 2016. Assessment of forest management in protected areas based on multidisciplinary research. *Forests* 7(11):285. https://doi.org/10.3390/f7110285.

Magnussen, S., T. Nord-Larsen and T. Riis-Nielsen. 2018. Lidar supported estimators of wood volume and aboveground biomass from the Danish national forest inventory (2012–2016). *Remote Sensing of Environment* 211:146–153. https://doi.org/10.1016/j.rse.2018.04.015.

Malimbwi, R. E., T. Eid and S.A.O. Chamshama. 2016. *Allometric Tree Biomass and Volume Models in Tanzania*. Department of Forest Mensuration and Management, College of Forestry, Wildlife and Tourism, Sokoine University of Agriculture, Morogoro.

Marziliano, P. A., G. Menguzzato and V. Coletta. 2017. Evaluating carbon stock changes in forest and related uncertainty. *Sustainability* 9(10):1702. https://doi.org/10.3390/su9101702.

Matasci, G., T. Hermosilla, M. A. Wulder, J. C. White, N. C. Coops, G. W. Hobart and H. S. Zald. 2018. Large-area mapping of Canadian boreal forest cover, height, biomass and other structural attributes using Landsat composites and lidar plots. *Remote Sensing of Environment* 209:90–106. https://doi.org/10.1016/j.rse.2017.12.020.

Mosier, T. M., D. F. Hill and K. V. Sharp. 2014. 30-Arcsecond monthly climate surfaces with global land coverage. *International Journal of Climatology* 34(7):2175–2188.

Mukhametov, A. E., D. R. Dautkanova and G. N. Zhakupova. 2018. Oxidation of vegetable fats and methods of their analysis. *Journal of Engineering and Applied Sciences* 13(S8):6462–6466.

Nguyen, T. H., S. D. Jones, M. Soto-Berelov, A. Haywood and S. Hislop. 2020. Monitoring aboveground forest biomass dynamics over three decades using Landsat time-series and single-date inventory data. *International Journal of Applied Earth Observation and Geoinformation* 84:101952. https://doi.org/10.1016/j.jag.2019.101952.

Pechanec, V., F. Stržínek, J. Purkyt, L. Štěrbová and P. Cudlín. 2017. Carbon stock in forest aboveground biomass-comparison based on Landsat data. *Lesnicky Casopis* 63(2–3):126–132. https://doi.org/10.1515/forj-2017-0014.

Pechanec, V., L. Štěrbová, J. Purkyt, M. Prokopová, R. Včeláková, O. Cudlín, P. Vyvlečka, E. Cienciala and P. Cudlín. 2022. Selected aspects of carbon stock assessment in aboveground biomass. *Land* 11(1):66. https://doi.org/10.3390/land11010066.

Pinzón, J. E., M. E. Brown and C. J. Tucker. 2005. EMD correction of orbital drift artifacts in satellite data stream. In *Hilbert-Huang Transform and Its Applications*, Vol. 5. Singapore: World Scientific, pp. 167–186. https://doi.org/10.1142/9789814508247_0011.

Ponce-Hernandez, R., P. Koohafkan and J. Antoine. 2004. *Assessing Carbon Stocks and Modelling Win-win Scenarios of Carbon Sequestration Through Land-Use Changes*, Vol. 1. Rome: Food and Agriculture Organization of the United Nations.

Pourshamsi, M., J. Xia, N. Yokoya, M. Garcia, M. Lavalle, E. Pottier and H. Balzter. 2021. Tropical forest canopy height estimation from combined polarimetric SAR and LiDAR using machine-learning. *ISPRS Journal of Photogrammetry and Remote Sensing* 172:79–94. https://doi.org/10.1016/j.isprsjprs.2020.11.008.

Pugh, T. A., M. Lindeskog, B. Smith, B. Poulter, A. Arneth, V. Haverd and L. Calle. 2019. Role of forest regrowth in global carbon sink dynamics. *Proceedings of the National Academy of Sciences* 116(10):4382–4387. https://doi.org/10.1073/pnas.1810512116.

Ruiz, L. Á., J. A. Recio, P. Crespo-Peremarch and M. Sapena. 2018. An object-based approach for mapping forest structural types based on low-density LiDAR and multispectral imagery. *Geocarto International* 33(5):443–457. https://doi.org/10.1080/10106049.2016.1265595.

Sakharova, T., A. Mukhametov and D. Bokov. 2022. The role of divalent iron cations in the growth, adhesive properties and extracellular adaptation mechanisms of Propionibacterium sp. *Saudi Journal of Biological Sciences* 29(5):3642–3646. https://doi.org/10.1016/j.sjbs.2022.02.048.

Schöne, D. and A. Schulte. 1999. Forestry after Kyoto: Quantifying and utilizing carbon sinks in practice. *Forstarchiv* 70(5):167–176.

Shoot, C., H. E. Andersen, L. M. Moskal, C. Babcock, B. D. Cook and D. C. Morton. 2021. Classifying forest type in the national forest inventory context with airborne hyperspectral and lidar data. *Remote Sensing* 13(10):1863. https://doi.org/10.3390/rs13101863.

Silva, C. A., S. Saatchi, M. Garcia, N. Labriere, C. Klauberg, A. Ferraz, V. Meyer, K. J. Jeffery, K. Abernethy, L. White, K. Zhaoet, S. L. Lewis and A. T. Hudak. 2018. Comparison of small-and large-footprint lidar characterization of tropical forest aboveground structure and biomass: A case study from Central Gabon. *IEEE Journal of Selected Topics in Applied Earth Observations and Remote Sensing* 11(10):3512–3526. https://doi.org/10.1109/JSTARS.2018.2816962.

Situmorang, J. P., S. Sugianto and D. Darusman. 2016. Estimation of carbon stock stands using EVI and NDVI vegetation index in production forest of lembah Seulawah sub-district, Aceh Indonesia. *Aceh International Journal of Science and Technology* 5(3):126–139. https://doi.org/10.13170/aijst.5.3.5836.

Stephenson, N. L., A. J. Das, R. Condit, S. E. Russo, P. J. Baker, N. G. Beckman, D. A. Coomes, E. R. Lines, W. K. Morris, N. Rüger, E. Álvarez, C. Blundo, S. Bunyavejchewin, G. Chuyong, S. J. Davies, Á. Duque, C. N. Ewango, O. Flores, J. F. Franklin, H. R. Grau, Z. Hao, M. E. Harmon, S. P. Hubbell, D. Kenfack, Y. Lin, J.-R. Makana, A. Malizia, L. R. Malizia, R. J. Pabst, N. Pongpattananurak, S.-H. Su, I-F. Sun, S. Tan, D. Thomas, P. J. van Mantgem, X. Wang, S. K. Wiser and M. A Zavala. 2014. Rate of tree carbon accumulation increases continuously with tree size. *Nature* 507:90–93. https://doi.org/10.1038/nature12914.

Strîmbu, V. F., L. T. Ene, T. Gobakken, T. G. Gregoire, R. Astrup and E. Næsset. 2017. Post-stratified change estimation for large-area forest biomass using repeated ALS strip sampling. *Canadian Journal of Forest Research* 47(6):839–847. https://doi.org/10.1139/cjfr-2017-0031.

Thies, M., N. Pfeifer, D. Winterhalder and B. G. Gorte. 2004. Three-dimensional reconstruction of stems for assessment of taper, sweep and lean based on laser scanning of standing trees. *Scandinavian Journal of Forest Research* 19(6):571–581. https://doi.org/10.1080/02827580410019562.

Tijerín-Triviño, J., D. Moreno-Fernández, M. A. Zavala, J. Astigarraga and M. García. 2022. Identifying forest structural types along an aridity gradient in peninsular Spain: Integrating low-density LiDAR, forest inventory, and aridity index. *Remote Sensing of Environment* 14(1):235. https://doi.org/10.3390/rs14010235.

Togisbayeva, A., D. Gura, S. Makar and I. Akulinina. 2022. Effect of outdoor recreation on forest phytocenosis. *Biodiversity and Conservation* 31(7):1893–1908. https://doi.org/10.1007/s10531-022-02425-6.

Tucker, C. J., J. E. Pinzon, M. E. Brown, D. A. Slayback, E. W. Pak, R. Mahoney, E. F. Vermote and N. El Saleous. 2005. An extended AVHRR 8-km NDVI dataset compatible with MODIS and SPOT vegetation NDVI data. *International Journal of Remote Sensing* 26(20):4485–4498. https://doi.org/10.1080/01431160500168686.

Vafaei, S., J. Soosani, K. Adeli, H. Fadaei, H. Naghavi, T. D. Pham and D. Tien Bui. 2018. Improving accuracy estimation of forest aboveground biomass based on incorporation of ALOS-2 PALSAR-2 and Sentinel-2A imagery and machine learning: A case study of the Hyrcanian forest area (Iran). *Remote Sensing* 10(2):172. https://doi.org/10.3390/rs10020172.

Valbuena, R., M. Maltamo, L. Mehtätalo and P. Packalen. 2017. Key structural features of boreal forests may be detected directly using L-moments from airborne lidar data. *Remote Sensing of Environment* 194:437–446. https://doi.org/10.1016/j.rse.2016.10.024.

Wiggins, H. L., C. R. Nelson, A. J. Larson and H. D. Safford. 2019. Using LiDAR to develop high-resolution reference models of forest structure and spatial pattern. *Forest Ecology and Management* 434:318–330. https://doi.org/10.1016/j.foreco.2018.12.012.

Xu, Z., X. Shen, L. Cao, N. C. Coops, T. R. Goodbody, T. Zhong, W. Zhao, Q. Sun, S. Ba, Z. Zhang and X. Wu. 2020. Tree species classification using UAS-based digital aerial photogrammetry point clouds and multispectral imageries in subtropical natural forests. *International Journal of Applied Earth Observation and Geoinformation* 92:102173. https://doi.org/10.1016/j.jag.2020.102173.

Yan, F., W. Li, G. Wang, J. Geng, Z. Lu, Z. Zhai and Y. Zhang. 2021. Sensory characteristics analysis for typical odor emission sources. *Archives of Environmental Protection* 47(3):92–97. https://doi.org/10.24425/aep.2021.138467.

Zhang, X., Y. Zhao, M. S. Ashton and X. Lee. 2012. Measuring carbon in forests. In *Managing Forest Carbon in a Changing Climate.* Dordrecht, the Netherlands: Springer, pp. 139–164. https://doi.org/10.1007/978-94-007-2232-3_7.

Zhou, L., C. J. Tucker, R. K. Kaufmann, D. Slayback, N. V. Shabanov and S. B. Myneni. 2001. Variations in northern vegetation activity inferred from satellite data of vegetation index during 1981 to 1999. *Journal of Geophysical Research: Atmospheres* 106(D17):20069–20083. https://doi.org/10.1029/2000JD000115.

Special Advertising Opportunities

FRONT COVER SPONSORSHIP

A *PE&RS* cover sponsorship is a unique opportunity to capture the undivided attention of your target market through three premium points of contact.

1— *PE&RS* FRONT COVER

(Only twelve available, first-come, first-served)
PE&RS is world-renowned for the outstanding imagery displayed monthly on its front cover—and readers have told us they eagerly anticipate every issue. This is a premium opportunity for any company, government agency, university or non-profit organization to provide a strong image that demonstrates their expertise in the geospatial information industry.

2— FREE ACCOMPANYING "HIGHLIGHT" ARTICLE

A detailed article to enhance your cover image is welcome but not a condition of placing an image. Many readers have asked for more information about the covers and your article is a highly visible way to tell your story in more depth for an audience keenly interested in your products and services. No article is guaranteed publication, as it must pass ASPRS editorial review. For more information, contact Rae Kelley at rkelley@asprs.org.

3— FREE TABLE OF CONTENTS COVER DESCRIPTION

Use this highly visible position to showcase your organization by featuring highlights of the technology used in capturing the front cover imagery. Limit 200-word description.

Terms: Fifty percent nonrefundable deposit with space reservation and payment of balance on or before materials closing deadline.

Cover Specifications: Bleed size: 8 5/8" × 11 1/4", Trim: 8 3/8" × 10 7/8"

PRICING

	Sustaining Member Exhibiting at a 2023 ASPRS Conference	Sustaining Member	Exhibitor	Non Member
Cover 1	$1,850	$2,000	$2,350	$2,500

Belly Bands, Inserts, Outserts & More!

Make your material the first impression readers have when they get their copy of *PE&RS*. Contact Bill Spilman at bill@innovativemediasolutions.com

VENDOR SEMINARS

ASPRS Sustaining Members now have the opportunity to hold a 1-hour informational session as a Virtual Vendor Seminar that will be free to all ASPRS Members wishing to attend. There will be one opportunity per month to reach out to all ASPRS Members with a demonstration of a new product, service, or other information. ASPRS will promote the Seminar through a blast email to all members, a notice on the ASPRS web site home page, and ads in the print and digital editions of *PE&RS*.

The Virtual Seminar will be hosted by ASPRS through its Zoom capability and has the capacity to accommodate 500 attendees.

Vendor Seminars	
Fee	$2,500 (no discounts)

DIGITAL ADVERTISING OPPORTUNITIES

EMPLOYMENT PROMOTION

When you need to fill a position right away, use this direct, right-to-the-desktop approach to announce your employment opportunity. The employment opportunity will be sent once to all ASPRS members in our regular Wednesday email newsletter to members, and will be posted on the ASPRS Web site for one month. This type of advertising gets results when you provide a web link with your text.

Employment Opportunity	Net Rate
30-Day Web + 1 email	$500/opportunity
Web-only (no email)	$300/opportunity

Do you have multiple vacancies that need to be filled? Contact us for pricing details for multiple listings.

NEWSLETTER DISPLAY ADVERTISING

Your vertical ad will show up in the right hand column of our weekly newsletter, which is sent to more than 3,000 people, including our membership and interested parties. **Open Rate: 32.9%**

Newsletter vertical banner ad	Net Rate
180 pixels x 240 pixels max	$500/opportunity

DEDICATED CONTENT EMAIL BLAST

Send a dedicated email blast to the ASPRS email list. Advertiser supplies HTML (including images). Lead time: 14 days.

Materials	Net Rate
Advertiser supplies HTML, including images.	$3000/ opportunity

PE&RS Digital Edition

Digital Edition Announcement E-Mail: 5,800+

PE&RS is available online in both a public version that is available to anyone but does not include the peer-reviewed articles, and a full version that is available to ASPRS members only upon login.

The enhanced version of *PE&RS* contains hot links for all ASPRS Sustaining Member Companies, as well as hot links on advertisements, ASPRS Who's Who, and internet references.

Become a sponsor today!

The e-mail blast sponsorship opportunity includes a **180 x 240 pixel ad** in the email announcement that goes out to our membership announcing the availability of the electronic issue.

Digital Edition Opportunities	Net Rate
E-mail Blast Sponsorship*	$1,000

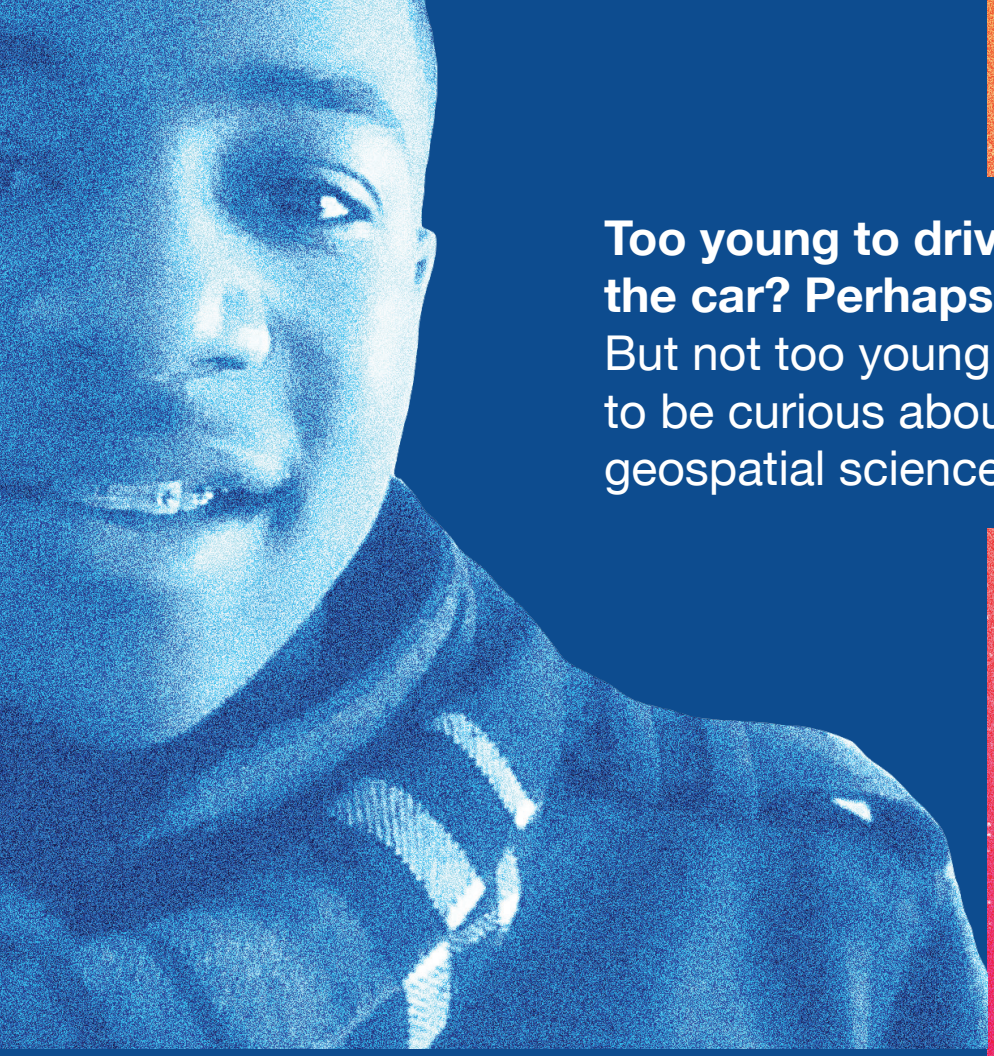

Too young to drive the car? Perhaps!
But not too young to be curious about geospatial sciences.

asprs FOUNDATION

The ASPRS Foundation was established to advance the understanding and use of spatial data for the betterment of humankind.

The Foundation provides grants, scholarships, loans and other forms of aid to individuals or organizations pursuing knowledge of imaging and geospatial information science and technology, and their applications across the scientific, governmental, and commercial sectors.

Support the foundation, so when they are ready, we are too.

asprsfoundation.org/donate